

L. TAUSCHER

DISS. ETH No. 9350

and report of the Institute for Intermediate Energy Physics (ETHZ)

$p\bar{p}$ ANNIHILATION INTO K^+K^- AND $\pi^+\pi^-$

A dissertation submitted to the
SWISS FEDERAL INSTITUTE OF TECHNOLOGY ZURICH

for the degree of

Doctor of Natural Sciences

presented by

Christoph Witzig
dipl. phys. ETHZ
born December 31, 1959
citizen of Zurich and Laufen-Uhwiesen, Switzerland

accepted on the recommendation of

Prof. Dr. H.-J. Gerber examiner

Prof. Dr. L. Tauscher co-examiner

1991

CERN LIBRARIES, GENEVA



DISS. ETH No. 9350

CM-P00081065

and report of the Institute for Intermediate Energy Physics (ETHZ)

$p\bar{p}$ ANNIHILATION INTO K^+K^- AND $\pi^+\pi^-$

A dissertation submitted to the
SWISS FEDERAL INSTITUTE OF TECHNOLOGY ZURICH

for the degree of

Doctor of Natural Sciences

CERN LIBRARIES, GENEVA

presented by

Christoph Witzig
dipl. phys. ETHZ
born December 31, 1959
citizen of Zurich and Laufen-Uhwiesen, Switzerland

accepted on the recommendation of

Prof. Dr. H.-J. Gerber examiner

Prof. Dr. L. Tauscher co-examiner

1991

Contents

Abstract	3
Zusammenfassung	4
1 Introduction	5
2 The CPLEAR Experiment	7
2.1 The Physics Motivation of CPLEAR	7
2.2 The Experimental Program of CPLEAR	9
2.3 The CPLEAR Detector	13
2.3.1 The CPLEAR Coordinate Convention	13
2.3.2 The CPLEAR Detector	13
2.4 The CPLEAR Trigger	21
2.4.1 Hard Wired Processor 1: HWP 1	23
2.4.2 Hard Wired Processor 2: HWP 2	26
2.4.3 Hard Wired Processor HWP 2.5	26
2.4.4 Hard Wired Processor 3 and 4: HWP 3 and 4	27
2.4.5 Trigger Decisions	27
3 The CPLEAR Data Acquisition System	30
3.1 General Online Considerations	30
3.2 Root Read Out and Event Builder	32
3.3 Data Distribution System	38
3.3.1 The Principles of the VMV	38
3.3.2 The Data Transfers from EB to TAPE / MSP over DDS	39
3.4 TAPE and MSP VALET	41
3.5 The ϵ'/ϵ Data Stream	42
3.5.1 Online Constraints	42
3.5.2 The EPS Valet	43
3.6 The Communication between the VALET and the VAX Cluster	44
4 $p\bar{p}$ Annihilation into K^+K^- and $\pi^+\pi^-$	47
4.1 Theoretical Introduction	47
4.1.1 Formation and Cascade of the Protonium	47
4.1.2 $p\bar{p}$ Annihilation	52
4.2 Analysis of the Relative Branching Ratio $R = \frac{BR(p\bar{p} \rightarrow K^+K^-)}{BR(p\bar{p} \rightarrow \pi^+\pi^-)}$	58

4.2.1	Some Initial Remarks on the CPLEAR Offline Package	58
4.2.2	Data Reduction	58
4.2.3	Back to Back Selection	62
4.2.4	Determination of the Uncorrected Branching Ratio R_{raw} . . .	66
4.3	Monte Carlo Studies	71
4.3.1	The Relative Acceptance between Back to Back Kaons and Pions	73
4.3.2	The Monte Carlo Background Simulation	74
4.3.3	Fit to a Monte Carlo Sample	76
4.4	Discussion	79
5	Conclusion	83
A	Appendix	84
A.1	Introduction	84
A.2	Phenomenological Description	86
A.2.1	Interference Phenomena	89
A.2.2	Decay into $\pi\pi$	91
A.2.3	CP Violation in Other Decay Modes of the Neutral Kaon System	94
A.3	The Current Experimental Status	95
B	Appendix	97
B.1	The VALET PLUS	97
B.2	FIC8230	98
B.3	The VME Vertical Bus VMV	99
B.3.1	General Principles of the VMV bus	100
B.3.2	The CES Modules VBE 8212 and VBR 3213	100
B.3.3	VMV Addressing Modes:	100
B.3.4	VMV Setup in CPLEAR	101
B.3.5	Timeout Handling on the Vertical Bus	101
C	Appendix	103
	Curriculum Vitae	111
	Acknowledgments	112

Abstract

The CERN experiment PS195 (CPLEAR) is designed to study CP violation in the decay of the neutral K meson. The novel feature of this experiment is to use initially pure K^0 and \bar{K}^0 states, which are produced in the $p\bar{p}$ annihilation into $K^+\pi^-\bar{K}^0$ and $K^-\pi^+K^0$. By measuring the rate asymmetry between the initially pure K^0 and \bar{K}^0 states into a given final state as a function of the kaon eigentime one can deduce the CP violating parameters.

The performance of the detector has been studied by identifying various $p\bar{p}$ annihilation channels. In the present thesis the relative branching ratio of $p\bar{p}$ annihilation into K^+K^- and $\pi^+\pi^-$ in gaseous hydrogen at 15 bar has been measured for the first time to be

$$\frac{BR(p\bar{p} \rightarrow K^+K^-)}{BR(p\bar{p} \rightarrow \pi^+\pi^-)} = 0.205 \pm 0.017$$

Combining this relative branching ratio with the absolute branching ratios of $p\bar{p}$ annihilation into K^+K^- and $\pi^+\pi^-$ from initial $p\bar{p}$ s and p states allows the determination of the fraction of p wave annihilation f_p .

f_p depends on the target properties. At low target pressure p wave annihilation is dominant. On the other hand at high target pressure Stark mixing between degenerate angular momentum eigenstates of a given energy level of the $p\bar{p}$ atom leads mainly to annihilation from an atomic s state.

The obtained value for f_p at a target pressure of 15 bar of

$$f_p = 0.380 \pm 0.086$$

is consistent with measurements of f_p at 1 bar and liquid hydrogen, as well as with cascade calculations.

Zusammenfassung

Das CERN Experiment PS195 (CPLEAR) untersucht CP-Verletzung im Zerfall von neutralen Kaonen. Erstmals wird ein Strahl von reinen K^0 - und \overline{K}^0 -Zuständen beobachtet, die in der $p\bar{p}$ -Annihilation in $K^+\pi^-\overline{K}^0$ und $K^-\pi^+K^0$ erzeugt werden. Die CP-verletzenden Parameter werden aus den Asymmetrien der Zerfallsraten der ursprünglich reinen K^0 - und \overline{K}^0 -Zuständen gewonnen.

Zum Verständnis des Detektors wurden verschiedene $p\bar{p}$ -Annihilationskanäle untersucht. Im Rahmen der vorliegenden Arbeit wurde erstmals das relative Verzweigungsverhältnis der $p\bar{p}$ -Annihilation in K^+K^- und $\pi^+\pi^-$ in gasförmigem Wasserstoff bei einem Druck von 15 bar als

$$\frac{BR(p\bar{p} \rightarrow K^+K^-)}{BR(p\bar{p} \rightarrow \pi^+\pi^-)} = 0.205 \pm 0.017$$

bestimmt.

Unter Verwendung der absoluten Verzweigungsverhältnisse von $p\bar{p}$ -Annihilation aus ursprünglich reinen s- und p-Wellen kann der p-Wellenanteil der Annihilation f_p bestimmt werden.

f_p hängt von den Targeteigenschaften ab. Bei niedrigem Druck dominiert die p-Wellen-Annihilation. Bei hohem Targetdruck dagegen führen Stark-Übergänge zwischen den entarteten Drehimpulseigenzuständen eines bestimmten Energieniveaus vorwiegend zu Annihilationen aus einem atomaren s-Zustand.

Der erhaltene Wert für f_p bei 15 bar Druck von

$$f_p = 0.380 \pm 0.086$$

ist in Übereinstimmung mit Messungen bei 1 bar Druck und in flüssigem Wasserstoff und mit Resultaten von Kaskadenrechnungen.

1 Introduction

CP violation is one of the outstanding topics in particle physics. It is an isolated phenomenon, whose origin is still unknown. So far it has only been observed in the decay of the neutral kaon.

CPLEAR intends to measure CP violation using for the first time initially pure K^0 and \overline{K}^0 states, produced in $p\bar{p}$ annihilation at rest:

$$p\bar{p} \rightarrow K^+\pi^-\overline{K}^0 \quad \text{and} \quad p\bar{p} \rightarrow K^-\pi^+K^0.$$

The K^0 's and \overline{K}^0 's are tagged by the observation of the accompanying charged kaon (strangeness tagging).

The parameters describing CP violation can be gained out of the asymmetry

$$A_f(\tau) = \frac{R_f(\tau, \overline{K}^0) - R_f(\tau, K^0)}{R_f(\tau, \overline{K}^0) + R_f(\tau, K^0)}$$

where $R_f(\tau, K^0)$ ($R_f(\tau, \overline{K}^0)$) is the rate of an initially pure K^0 (\overline{K}^0) state into a final state $|f\rangle$ as a function of the eigentime τ in the rest frame of the neutral kaon.

The main advantage of using $p\bar{p}$ annihilation as a neutral kaon source is the different nature of its systematic errors compared to previous experiments on CP violation. In addition most of the systematic errors cancel to first order when taking the above mentioned asymmetries. Furthermore this method enables to observe CP violation in channels, where it has not been seen so far.

The main experimental challenges of this experiment are the realization of the trigger system (due to the small branching ratio of $p\bar{p}$ into $K^+\pi^-\overline{K}^0$ and $K^-\pi^+K^0$ of $2 \cdot 10^{-3}$) and the online system (due to the high data flux on tape). The online system makes extensive use of a microprocessor system, based on the VME standard, called VALET PLUS.

As an important byproduct CPLEAR is also able to study $p\bar{p}$ annihilation, mainly into kaonic final states. In the framework of this thesis the relative branching ratio

$$R = \frac{BR(p\bar{p} \rightarrow K^+K^-)}{BR(p\bar{p} \rightarrow \pi^+\pi^-)}$$

for gaseous hydrogen at a pressure of 15 bar has been measured for the first time. It allows the determination of the fraction of p wave annihilation under the above

mentioned target conditions.

CPLEAR took data for the first time in the second half of 1989.

This thesis is organized as follows:

In the next chapter we give a short introduction to the CPLEAR experiment. After discussing its physics motivation the detector is described rather briefly. The trigger system is explained in more detail in order to clarify its relation with the online system. A short overview of CP violation is given in appendix A.

The third chapter is dedicated to a detailed description of the CPLEAR online system, which is based on the VALET PLUS, a VME based microprocessor system. The VALET PLUS as well as some more technical details of the online system are explained in appendix B.

In chapter 4, the main part of this thesis, the $p\bar{p}$ annihilation into K^+K^- and $\pi^+\pi^-$ is discussed. In a theoretical introduction the cascade of the $p\bar{p}$ atom leading to the annihilation is explained, as well as some theoretical aspects of $p\bar{p}$ annihilation into the two body final states K^+K^- and $\pi^+\pi^-$. Then the analysis leading to the determination of the above mentioned branching ratio of $p\bar{p}$ annihilation into K^+K^- and $\pi^+\pi^-$ is presented. It is compared with the results of a Monte Carlo simulation. The last section is dedicated to a discussion of the obtained relative branching ratio. It is compared with previous measurements under different target conditions and related to the cascade process. Combining our result with the absolute branching ratios of $p\bar{p} \rightarrow K^+K^-$ and $p\bar{p} \rightarrow \pi^+\pi^-$ from the s and p levels of the $p\bar{p}$ atom leads to the determination of the fraction of p wave annihilation in hydrogen at 15 bar.

2 The CPLEAR Experiment

CPLEAR is designed to determine the CP violating parameters from the asymmetry

$$A_f(\tau) = \frac{R_f(\tau, \overline{K}^0) - R_f(\tau, K^0)}{R_f(\tau, \overline{K}^0) + R_f(\tau, K^0)} \quad (2.1)$$

where $R_f(\tau, K^0)$ ($R_f(\tau, \overline{K}^0)$) is the rate of an initially pure K^0 (\overline{K}^0) state ¹ into a final state $|f\rangle$ as a function of the eigentime τ in the rest frame of the neutral kaon.

The first section of this paragraph is dedicated to the physics motivation for this kind of measurement, its advantages and its experimental challenges. This then leads to the requirements that the detector has to fulfill.

In the second section we give a short description of the detector.

In the last paragraph the trigger is explained in more detail, in order to clarify the relationship with the online system, which will be discussed in the next chapter.

An overview of CP violation is given in appendix A.

2.1 The Physics Motivation of CPLEAR

Prior experiments measuring CP violation have generally used a K_L^0 beam. A K_S^0 component was either added by regeneration or by observing the kaon close to the production region. The parameters describing CP violation were extracted either from rate ratios of K_S^0 and K_L^0 , from the interference of the K_S^0 and the K_L^0 amplitude or from the interference of a incoherent mixture of K^0 and \overline{K}^0 states. Note, that all previous experiments measuring CP violation were performed at high energies.

CPLEAR [1,2,3] intends to pursue a new approach by measuring asymmetries, as explained below. $p\bar{p}$ annihilation at rest is used as a source of tagged low energy kaons. Thus CPLEAR measures CP violation at a new energy scale with a new method, leading to systematic errors of different nature compared to previous experiments. In addition most of the systematic errors cancel, when taking the asymmetries.

The following annihilation channels are of interest:

$$p\bar{p} \rightarrow K^+ \pi^- \overline{K}^0 \quad \text{Branching ratio} \simeq 2 \cdot 10^{-3} \quad (2.2)$$

$$p\bar{p} \rightarrow K^- \pi^+ K^0 \quad \text{Branching ratio} \simeq 2 \cdot 10^{-3}. \quad (2.3)$$

¹ $|\psi(\tau=0)\rangle = |K^0\rangle$ or $|\psi(\tau=0)\rangle = |\overline{K}^0\rangle$

Strangeness conservation guarantees, that the neutral kaon is in an initially pure $|K^0\rangle$ or $|\bar{K}^0\rangle$ state, i.e.

$$|\psi(\tau=0)\rangle = |K^0\rangle \quad \text{or} \quad |\psi(\tau=0)\rangle = |\bar{K}^0\rangle. \quad (2.4)$$

By determining the decay vertex of the neutral kaon ² into a final state $|f\rangle$, one gets the asymmetry

$$A_f(\tau) = \frac{R_f(\tau, \bar{K}^0) - R_f(\tau, K^0)}{R_f(\tau, \bar{K}^0) + R_f(\tau, K^0)} \quad (2.5)$$

$$= \frac{2\Re\hat{\epsilon} - 2(\frac{1}{2} \mp \Re\hat{\epsilon}) |\eta_f| e^{-\frac{\gamma_l - \gamma_s}{2}\tau} \cos(\Delta m\tau - \phi_f)}{1 + |\eta_f|^2 e^{-(\gamma_l - \gamma_s)\tau}} \quad (2.6)$$

where:

$R_f(\tau, K^0)$ is the rate of an initially pure $|K^0\rangle$ state into a final state $|f\rangle$ (respectively $R(\tau, \bar{K}^0)$ for \bar{K}^0),

τ eigentime in the rest frame of the neutral kaon,

$|\eta_f| e^{i\phi_f}$ is the ratio of the amplitudes of the CP forbidden to the CP allowed transition into the final state $|f\rangle$,

$\Re\hat{\epsilon}$ real part of the parameter $\hat{\epsilon}$, describing the mixing between K^0 , \bar{K}^0 and K_S^0 , K_L^0 ,

γ_s, γ_l the width of K_S^0 and K_L^0 ,

Δm the mass difference between K_L^0 and K_S^0 .

The desired annihilation final states $K^+\pi^-\bar{K}^0$ and $K^-\pi^+K^0$ are detected by triggering on a $K^\pm\pi^\mp$ pair coming from the target (strangeness tagging).

As the annihilation occurs at rest, the initial energy of the system is well defined (being $2M_p$, i.e. twice the proton mass).

With a \bar{p} flux of $2 \cdot 10^6 \bar{p}/\text{sec}$ provided by LEAR ³ at CERN, one expects to tag $\simeq 10^8$ neutral kaons per day.

What is the significance of measuring the interference effect out of an initially pure $|K^0\rangle$, $|\bar{K}^0\rangle$ state?

In detecting $|K_L^0\rangle \rightarrow |\pi\pi\rangle$ one looks for a transition violating a quantum number conservation rule. This method is not applicable for final states like $|\pi^+\pi^-\pi^0\rangle$

²An overview of CP violation is given in appendix A.

³Low Energy Antiproton Ring

or $|\gamma\gamma\rangle$ as both $|K_L^0\rangle$ as well as $|K_S^0\rangle$ are allowed to decay into by the CP symmetry.

On the other hand Sehgal and Wolfenstein pointed out [4], that “for any possible nonleptonic decay mode of the K^0 meson the observation of an interference effect between K_L^0 and K_S^0 decays in the partial decay rate of this mode is clear evidence of CP violation”.

The partial decay rate, in the meaning of the authors, includes an integration over all momenta and spin degrees of freedom.

Thus using asymmetries to measure CP violation is a more general method, than looking for a quantum number violating transition. It opens up the possibility to look for CP violation in channels, where it hasn't been seen so far.

Other advantages of measuring asymmetries, rather than rate ratios, are:

- The systematic errors of this kind of measurement will be completely different from the previous CP violation experiments. This allows an important cross-check on already measured parameters.
In addition most systematic errors cancel in first order, when taking the asymmetries.
- K^0 and \bar{K}^0 can be normalised independently.
- Formula 2.6 reveals another feature of using asymmetries: $|\eta_f|$ is measured to first order, whereas ratios of CP violating decays yield $|\eta_f|^2$. This is particular important for decays with low branching ratios, like $|K_S^0\rangle \rightarrow |\pi\pi\rangle$.

2.2 The Experimental Program of CPLEAR

CPLEAR intends to measure:

- 2π decay:
 $\Re\hat{\epsilon}$, $|\eta_{+-}|$, ϕ_{+-} , $|\eta_{00}|$, ϕ_{00} can be extracted out of the time dependent asymmetry $A_{\pi\pi}(\tau)$ in the region $5\tau_s < \tau < 20\tau_s$. Figure 1 shows the asymmetry $A_{\pi^+\pi^-}(\tau)$ as a function of eigentime τ as an illustration.
The measurement of ϵ'/ϵ is unlikely to be possible from $|\eta_{+-}|$ and $|\eta_{00}|$, because of the expected precision of the eigentime measurement.

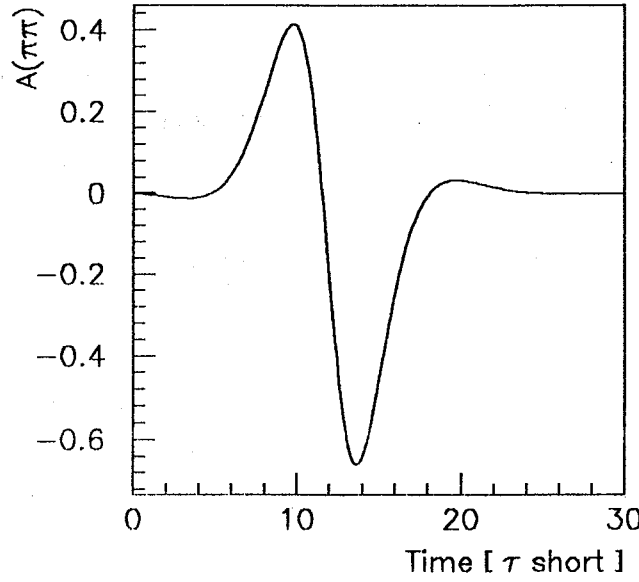


Figure 1: Time dependent asymmetry $A_{\pi\pi}(\tau) = \frac{R_{\pi\pi}(\tau, \overline{K^0}) - R_{\pi\pi}(\tau, K^0)}{R_{\pi\pi}(\tau, \overline{K^0}) + R_{\pi\pi}(\tau, K^0)}$ for the final state $|f\rangle = |\pi^+\pi^-\rangle$ for $0 < \tau < 30\tau_s$.

- ϵ'/ϵ :

The integral asymmetry for a final state $|f\rangle$ is defined as

$$I_f(\tau) = \frac{\int_0^\tau R_f(\tau', \overline{K^0}) d\tau' - \int_0^\tau R_f(\tau', K^0) d\tau'}{\int_0^\tau R_f(\tau', \overline{K^0}) d\tau' + \int_0^\tau R_f(\tau', K^0) d\tau'} \quad (2.7)$$

where $R_f(\tau', K^0)$ is as before the rate of an initially pure $|K^0\rangle$ state into a final state $|f\rangle$ (respectively $R_f(\tau, \overline{K^0})$ for $|\overline{K^0}\rangle$). It can be shown [1,3], that ϵ'/ϵ can be measured using the relation

$$\frac{\Re\epsilon'}{\Re\epsilon} \simeq \frac{1}{6} \left(1 - \frac{I_{00}}{I_{+-}}\right). \quad (2.8)$$

Note that this is a measurement of $\Re\epsilon'/\Re\epsilon$, whereas the other experiments so far measured $\Re(\epsilon'/\epsilon)$ (eq. A.61).

- Nonleptonic channels other than $\pi\pi$:

Looking for interference terms in decay channels of neutral kaons, where CP violation has not yet been seen, such as

- $|K_S^0\rangle \rightarrow |\pi^0\pi^0\pi^0\rangle$ (forbidden by CP),
- $|K_S^0\rangle \rightarrow |\pi^+\pi^-\pi^0\rangle$ (the allowed state is suppressed because of angular momentum barriers).

- Semileptonic decay:

We define

$R_{\pm}(\tau)$: the rate of an initially pure $|K^0\rangle$ state into $|\pi^{\mp}l^{\pm}\nu\rangle$

$\overline{R}_{\pm}(\tau)$: the rate of an initially pure $|\overline{K}^0\rangle$ state into $|\pi^{\mp}l^{\pm}\nu\rangle$

Two tests are possible in the semileptonic decay:

- $\Delta S = \Delta Q$ rule:

The total semileptonic decay rate

$$R_{tot}(\tau) = R_+(\tau) + R_-(\tau) + \overline{R}_+(\tau) + \overline{R}_-(\tau) \quad (2.9)$$

depends on $\Re x$, and the rate difference

$$A(\tau) = \frac{(\overline{R}_+(\tau) + \overline{R}_-(\tau)) - (R_+(\tau) + R_-(\tau))}{\overline{R}_+(\tau) + \overline{R}_-(\tau) + R_+(\tau) + R_-(\tau)} \quad (2.10)$$

on $\Im x$,

where x describes the violation of the $\Delta S = \Delta Q$ rule (eq A.68). Note that in those two measurements no e/μ separation is needed.

- Expected T violating effects can be observed in the asymmetry

$$A_T(\tau) = \frac{R(\overline{K}^0 \rightarrow e^+\pi^-\nu, \tau) - R(K^0 \rightarrow e^-\pi^+\nu, \tau)}{R(\overline{K}^0 \rightarrow e^+\pi^-\nu, \tau) + R(K^0 \rightarrow e^-\pi^+\nu, \tau)} \quad (2.11)$$

assuming the $\Delta S = \Delta Q$ rule. This measurement requires e/π separation.

- CPT violation:

The neutral kaon system is also well suited to look for possible CPT violations.

Possible effects might be seen in:

- Wu-Yang triangle, in particular in the phase differences (eq. A.63-A.65) [5].

- The time dependent asymmetry $A_{\pi\pi}(\tau)$ extrapolated to $\tau = 0$ (eq. A.31, A.33).

Requirements to the Detector

First we give an overview of the experimental challenges for performing such an experiment.

- By producing neutral kaons out of $p\bar{p}$ annihilation, one has to cope with the annihilation background. This is in particular a problem for those asymmetries, which require measurements at low lifetimes ($\tau < 5\tau_s$), namely the integral, semileptonic and 3π asymmetries.

- Whereas the eigentime dependent efficiency of the neutral kaon tagging should cancel in first order in the time dependent asymmetries, it has to be taken into account for the measurement of the integral asymmetries.
- The measurement of the eigentime of the neutral Kaon has to be precise enough in order to allow the extraction of the time dependent asymmetries. This is especially challenging for the neutral decay mode, as it includes the determination of energy and position of four photons. In particular the decay $|K_L^0\rangle \rightarrow |\pi^0\pi^0\pi^0\rangle$, where two photons are not detected, will contribute to the background.

We can now formulate the requirements for the detector:

- It needs a large solid angle to maximize the detection efficiency of particles.
- It has to be sufficiently large in order to contain the interference region for the $\pi\pi$ decay mode. As the average momentum of the neutral kaons is 550 MeV/c, the tracks should be reconstructed up to a distance of 50 cm in the transversal plane (transversal means perpendicular to the magnetic field).

Drift and proportional chambers are used for tracking.

The thickness of those chambers in units of radiation length has to be minimized, in order to avoid regeneration of the neutral kaon. This in turn would introduce a bias between the initially pure $|K^0\rangle$ and $|\bar{K}^0\rangle$ states and change the expected shape of the asymmetries.

- The channels $K^+\pi^-\bar{K}^0$ and $K^-\pi^+K^0$ have to be detected reliably, in order to reduce the annihilation background.

In addition this decision has to be made as early as possible in order to reduce the event rate.

A particle identification detector (PID) consisting of a Cerenkov counter, sandwiched between two scintillators, is used to separate kaons from pions.

- An electromagnetic calorimeter is needed for the detection of photons from π^0 decays, as well as for the identification of e and μ from leptonic decay modes.

2.3 The CPLEAR Detector

2.3.1 The CPLEAR Coordinate Convention

We mention the CPLEAR coordinate convention, before starting the detector description (figure 2).

- The coordinate system is right handed with the target at the origin.
- Z-AXIS:
Points in the beam direction, which is also the axis of the detector. The magnetic field is along the z-axis. Upstream means $-z$ direction, downstream $+z$ direction.
- X-AXIS:
Is horizontal and points to the left looking along the z-axis.
- Y-AXIS:
Points upwards.
- Transversal Plane:
The xy plane is called transversal plane (with respect to the magnetic field).

2.3.2 The CPLEAR Detector

We describe now very briefly the different parts of the detector, which are shown in figure 2-4. The dimensions and number of elements of each subdetector are listed in table 2. In table 3 the design values for the efficiency, resolution and the sectorization is given. The sectorization of each detector corresponds to the partition of the read out electronics. The trigger gets in a first pass the hit maps of the detector based on this sectorization.

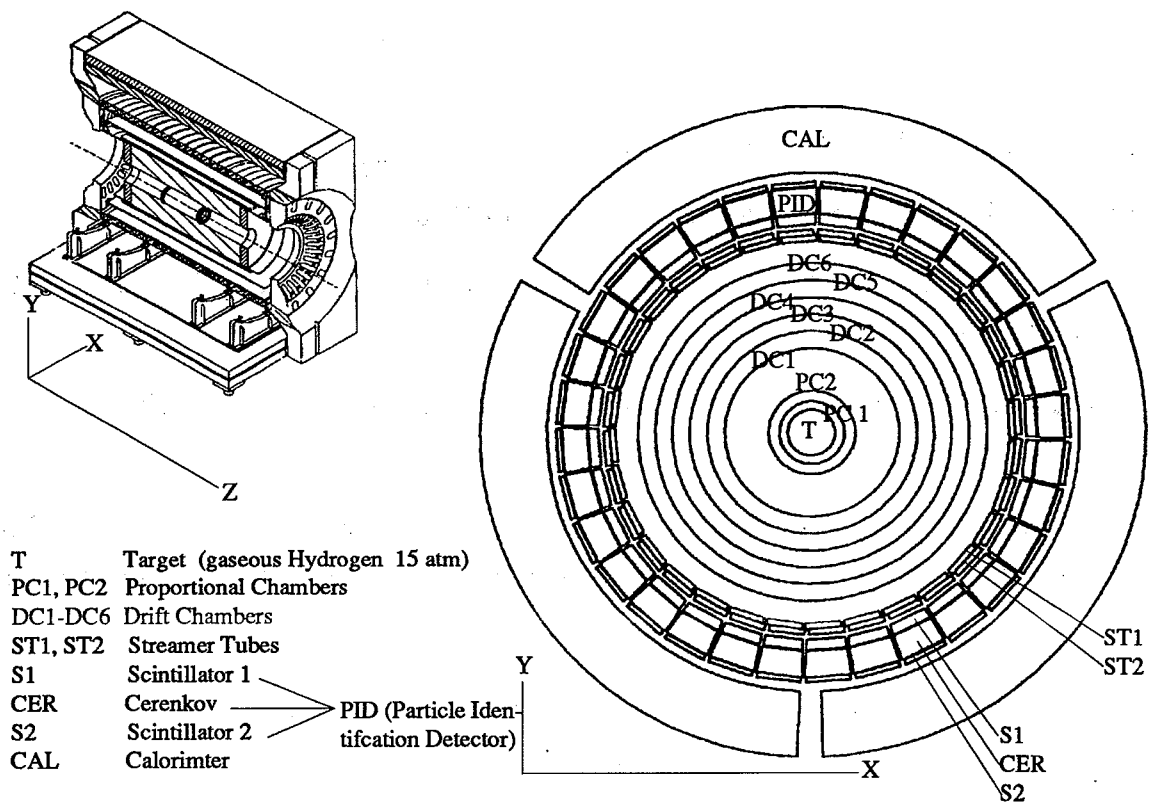


Figure 2: Transversal view of the CPLEAR detector.

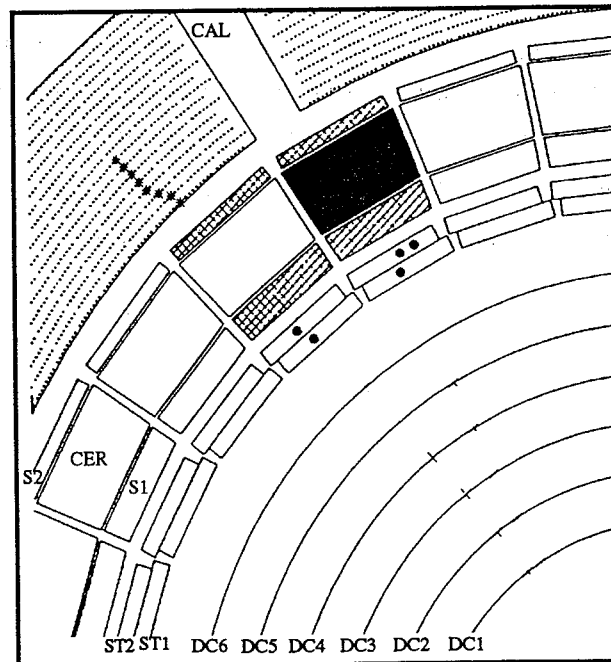


Figure 3: Section of the detector with DCs, ST1, ST2, PID and calorimeter segments.

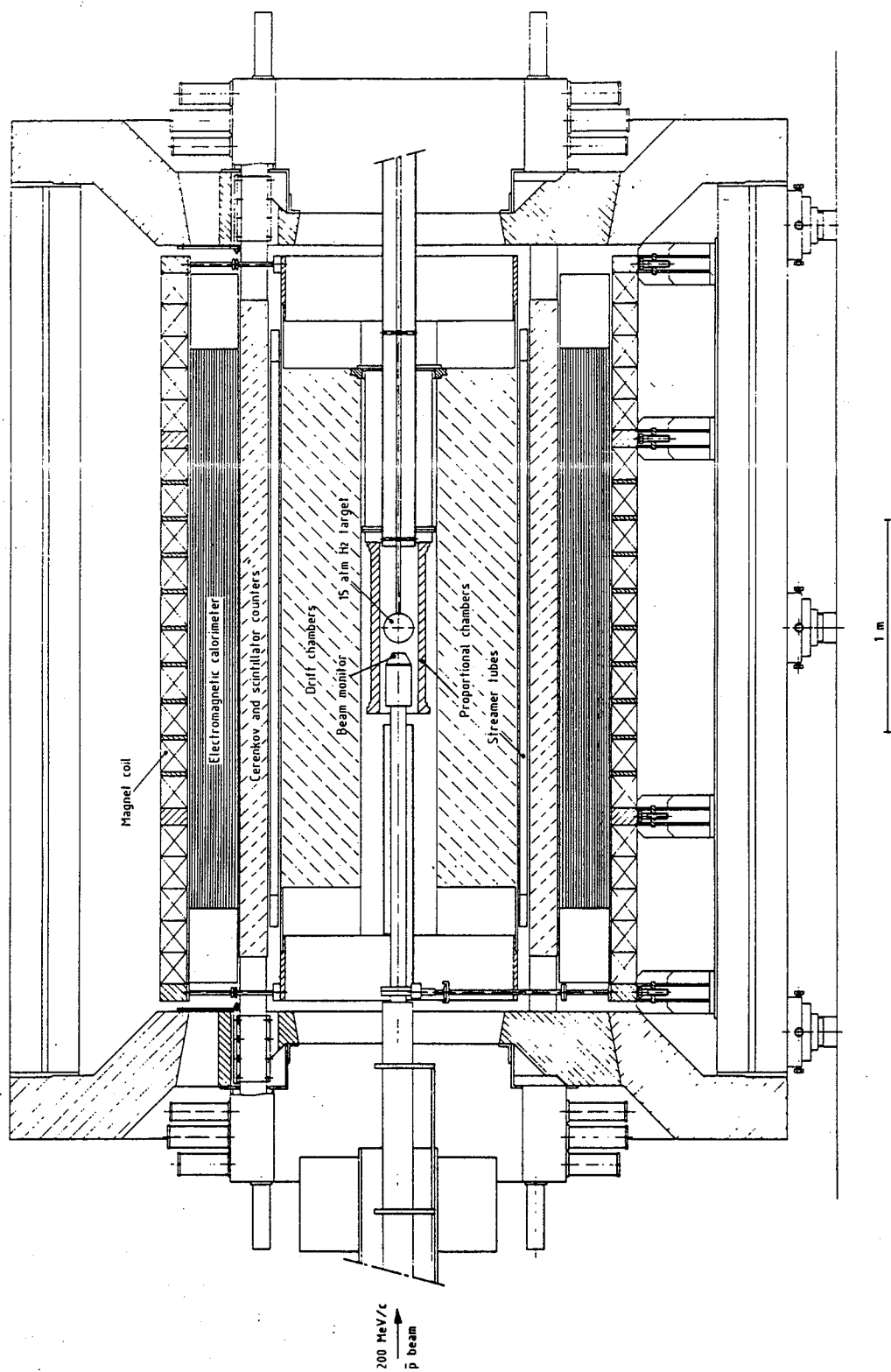


Figure 4: Longitudinal view of the CPLEAR detector.

- **MAGNET:**

It is a solenoid magnet. Its dimensions can be found in table 1.

- **BEAM MONITOR:**

The beam is monitored by 2 MWPC (multi wire proportional chambers). At the entrance of the target is a scintillator (beam counter), which signals an incoming \bar{p} .

- **TARGET:**

The target is a sphere made of kevlar with a wall thickness of 0.5 mm. The entrance window has a diameter of 11 mm and a thickness of 0.12 mm.

The target is filled with gaseous hydrogen at a pressure of 15 atm. The stopping distribution in the target is shown in figure 5. The FWHM ⁴ 200 MeV/c \bar{p} 's has been measured to be 25 mm.

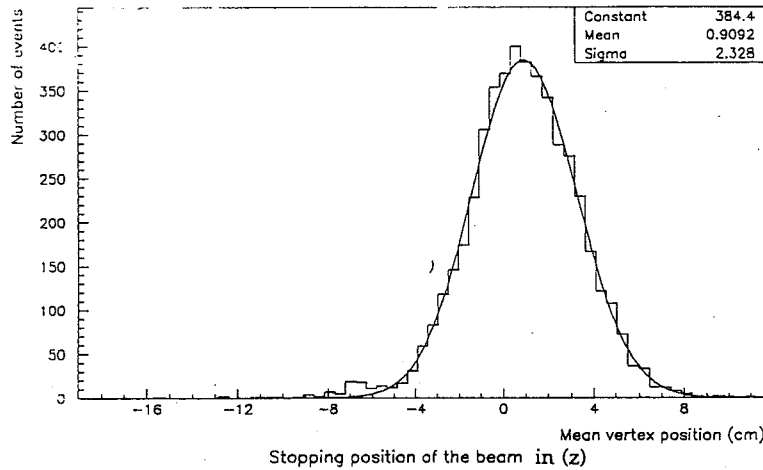


Figure 5: *Beam stopping distribution in the target.*

- **PROPORTIONAL CHAMBERS : PC1 and PC2**

The PCs provide the first points of a track at a high efficiency. They also enable the trigger to identify secondary particles (see below). Each PC consists of a wire plane with U and V strips at an angle of $16.1^\circ / -15.4^\circ$ for PC1 and $16.6^\circ / -18.3^\circ$ for PC2. The wire pitch is 1 mm, the strip pitch 2.4 mm. A gas mixture of 20 % isobutan, 69.5 % argon and 0.5 % freon (CF_3Br) is used.

A detailed description can be found in [6].

- **DRIFT CHAMBERS : DC1 - DC6**

The six drift chambers are the main tracking devices.

⁴Full Width at Half the Maximum height

They are equipped with U and V cathode strips at an angle between 11° / -12° (for DC1 U/V) and 25.7° / -25.7° (for DC6 U/V).

The wires are grouped in doublets (figure 6). The distance between two wires of a doublet is 0.5 mm and is guaranteed by small glue ball spacers at regular intervals of 20 cm. This doublet structure overcomes left - right ambiguities. The distance between two doublets is 1 cm with a potential wire situated inbetween. The strip pitch is 5 mm. The drift time is measured by 4 bit TDCs. The expected resolution in the transversal plane is $250 \mu\text{m}$, if the track does not cross the doublet. The resolution of the strips is designed to be 1 mm. The gas is a mixture of 50 % ethane and 50 % argon.

Each chamber has a thickness corresponding to $7 \cdot 10^{-4} X_0$ (radiation length).

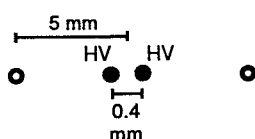


Figure 6: Doublet structure of the drift chambers.

- STREAMER TUBES : ST1 and ST2

There are two layers of 192 streamer tubes, each measuring $1.75 \times 1.75 \times 250$ cm (figure 3).

They provide a fast (700 ns) z measurement: The TDCs are started by the signal from the downstream end of the tube and stopped by the signal of the upstream end. The z position of the track can then be extracted from the TDC value.

There is a half tube stagger between the two layers in order to minimize dead space. The gas mixture consists of 46 % isobutane, 50 % argon and 4 % methylal and 0.008 % freon. A detailed description can be found in [7].

- PARTICLE IDENTIFICATION DETECTOR : PID

The PID (figure 3) consists of 32 elements. Each element is made up of a Cerenkov counter, sandwiched between two scintillators: S1 (closer to the target) and S2.

The Cerenkov consists of a box of extruded plexiglas with a trapezoidal cross-section (length 310 cm, thickness 8 cm, width 12.5 cm [closer to the target] and 14.1 cm). The Cerenkov box is filled with Fluorinert (FC72, C_6F_{14}) with Diphenyloxazol (PPO) as wavelength shifter. S1 and S2 are plastic scintilla-

tors.

The upstream and downstream ends of the PID are read out by flash ADC, S1 and Cerenkov also by TDC. There are eight photomultipliers per PID segment: Two for Cerenkov and one each for S1 and S2 on upstream and downstream end.

The threshold for light production in the Cerenkov is such, that pions are expected to give light in contrast to the heavier kaons. Therefore kaons are characterized by a $S\bar{C}S$ signal in the PID, pions by SCS . The S2 signal is used to detect the exit of the particle from the Cerenkov, as many conversions are expected to occur.

A detailed description can be found in [8,9].

- **ELECTROMAGNETIC CALORIMETER : CAL**

The electromagnetic calorimeter is needed for the vertex reconstruction of the neutral decay of the kaon into π^0 and photons. The accuracy of the vertex determination depends on the energy and shower foot resolution of the photons in the calorimeter. Monte Carlo studies have shown, that the latter is more important for the reconstruction of the neutral vertex. Therefore a gas sampling calorimeter of high granularity was chosen.

The calorimeter has 18 layers of 1.5 mm thick lead sheets ($\simeq 5.8$ radiation length). The lead sheets of each layer are split up for mechanical reasons into three pieces, each covering 120° . Each sheet is covered by an aluminium layer of 0.3 mm for stability. The first lead sheet is replaced by an aluminium cylinder of the same radiation thickness to enhance the stability. Between the lead sheets are layers of gas tubes, sandwiched by U and V strips at an angle of $\pm 30^\circ$ [10]. There is an average of 120 gas tubes per layer. A tube is subdivided into 8 cells (cross section 4.5×4 mm) with one wire each. The tubes work in limited streamer mode in a gas mixture of CO_2 (2/3) and n-pentan (1/3).

The calorimeter readout is only digital, as there are over 63'000 channels.

A detailed description can be found in [11].

Table 1: *Characteristics of the CPLEAR magnet.*

Inner axial length between the poles	362.0 cm
Inner diameter of the coil	200.0 cm
Weight	approx. 120 tons
Max. central field	0.438 Tesla

Table 2: *CPLEAR detector characteristics : (Mid-plane) radius. For PCs and DCs the radius of the wires. (Active) z length. Thickness: Difference between inner and outer radius. For target wall thickness. Number of elements: Number of wires, resp. segments. For PCs, DCs and CAL the number of wires (for DC doublets) U and V strips.*

Detector	Radius [cm]	z length [cm]	Thickness [cm]	number of elements
Target	7.0	-	0.50	-
PC1	9.52	70.00	1.00	576 246 262
PC2	12.70	70.00	1.00	768 310 325
DC1	25.46	233.60	1.00	160 275 285
DC2	30.56	233.60	1.00	192 324 336
DC3	35.65	233.60	1.00	224 378 385
DC4	40.74	233.60	1.00	256 424 432
DC5	45.84	233.60	1.00	288 465 477
DC6	50.93	233.60	1.00	320 510 520
ST1	58.22	252.00	1.75	32*6
ST2	59.97	252.00	1.75	32*6
S1	63.84	310.00	3.00	32
CER	69.43	310.00	8.00	32
S2	74.21	310.00	1.40	32
CAL	87.52	264.00	19.11	17'112 22'896 23'040

Table 3: CPLEAR detector characteristics : Sectorization of the read out: (For DC: 64*(2-3) means alternatively two or three doublets per sector.) Efficiency and Resolution: Design values are given, as not all the final read out electronics is at present operational. Resolution: For CAL: Resolution for shower foot determination and energy resolution.

Detector	sectorization	efficiency	resolution [cm]
Target	-	-	-
PC1	64*9	99 %	0.030 (wires)
PC2	64*12	99 %	0.040 (z)
DC1	64*(2-3)	96 %	For all DCs: 0.025 (wires) 0.10 (z) " " "
DC2	64*3	"	
DC3	64*(3-4)	"	
DC4	64*4	"	
DC5	64*(4-5)	"	
DC6	64*5	"	
ST1	32*2	98 %	0.50(r, φ) / 1.0(z)
ST2	32*2	98 %	0.50(r, φ) / 1.0(z)
S1	32*2	99.8 %	0.2 ns
CER	32*4		
S2	32*2		
CAL	4'853*8		0.3 (r, φ) 0.5 (z) $\sigma_E = \frac{15\%}{\sqrt{E}}$

2.4 The CPLEAR Trigger

The expected rate of incoming \bar{p} is $2 \cdot 10^6 \bar{p}/\text{sec}$, as already mentioned in section 2.1. This results in a rate of about $8 \cdot 10^3$ golden ⁵ events per second, which the trigger has to select.

The trigger [12] consists of several levels. In each level a characteristic of the event is examined. If it passes the test, it is kept, and the next test level is launched. Otherwise the event is rejected. Figure 7 gives an overview of the trigger system.

The trigger system is based on the interplay of four elements:

- The FRONT END ELECTRONICS (FE), which are the hardware modules for the readout of each detector (ADCs, TDCs ...).
- TRIGGER PROCESSORS: As mentioned above, there are several levels of trigger decisions. They can be grouped into several hard wired processor (HWP 1, 2, 2.5, 3 and 4). They will be described in the following sections.
- The TRIGGER CONTROL (TC) is the operating system of the trigger. It receives the results of the different trigger decision modules and takes the appropriate action (e.g. reset, strobe to start readout ...).
- The SPY is the interface between the trigger and the data acquisition system. It can acquire information contained in any module of the trigger. Its four output FIFOs (First In First Out) are connected to:

1. HWP RRO: (Hard Wired Processor Root Read Out): Read out of the trigger for the main data stream (see below).
2. Input to HWP 3 and HWP 4.
3. Input to the ϵ'/ϵ data stream (see section 3.5).
4. Not used.

Figure 8 shows the timing of the trigger.

⁵By golden event we mean the annihilation final state $K^+\pi^-\bar{K}^0$ or $K^-\pi^+K^0$

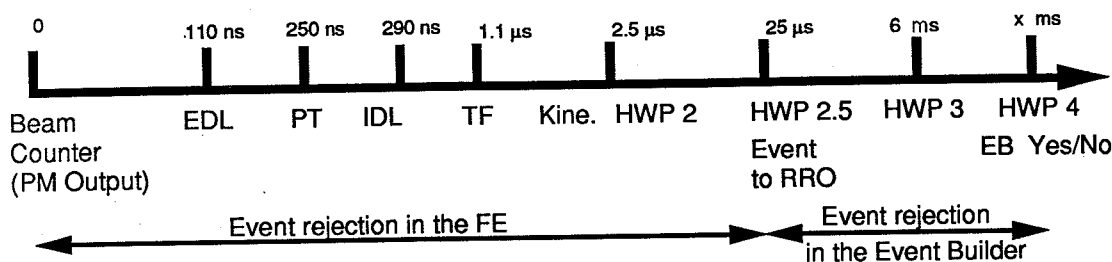


Figure 8: *Timing of the trigger. The main strobe is given after 110 ns, the transfer from the FE's to the data acquisition sytem after 25 μsec. The last possibility to reject an event is in the HWP4 stage after several milliseconds.*

Before describing the different steps in the trigger logic, we recall the general character of the golden event:

There should be one charged pion and one (oppositely) charged kaon coming from the target (called primary tracks), signalling $p\bar{p} \rightarrow K^+\pi^-\bar{K}^0$ or $p\bar{p} \rightarrow K^-\pi^+K^0$. Note, that demanding two hits in PCs corresponds to a cut on the lifetime of the neutral kaon in its charged decay mode.

2.4.1 Hard Wired Processor 1: HWP 1

Early Decision Logic: EDL

The incoming \bar{p} is signalled by the beam counter, which starts the triggering process.

The main task of the early decision is to identify within the shortest possible time the general character of an event. Therefore only information of the PID is used, which is available after 40 nanoseconds.

The EDL gets as input the logical (i.e. after proper discrimination) signals of all photomultipliers of the PID, namely $2 \cdot 32$ for S1, $4 \cdot 32$ from the Cerenkov, $2 \cdot 32$ from S2. These 256 signals are reduced to $3 \cdot 32 = 96$ by taking the OR of each subdetector.

The number of sectors having the signature $S\bar{C}S$ (meaning hit in S1 and S2, but not in the Cerenkov) is then checked. The presence of such a pattern is considered to be the first evidence of kaons.

The number of kaons candidates ($N_{S\bar{C}S}$ = number of $S\bar{C}S$) is determined. The event can be considered as good, if either exactly one or at least one kaon candidate has been found.

The charged multiplicity N_{S1} is estimated by counting the hits in S1 ⁶.

If the event survives those early decisions, the trigger control issues a strobe to the FE to start the conversion of the data.

The event is rejected, if the beam counter detects another incoming \bar{p} during those early decisions.

p_t cut

The next step is a cut on the transversal momentum (p_T) of the kaon candidate (figure 9). It is done in order to eliminate events with slow pions, which also give an $S\bar{C}S$ signature in the PID. For this decision the wire information of DC1 and DC6 is needed, which is passed directly from the FE to the p_T -cut processor.

Each PID corresponds to a sector of 15 wires in DC6. A p_T cut of 800, 400, 270 or 200 MeV/c can be done by demanding a hit in a sector of ± 1 , ± 2 , ± 3 or ± 4 wires around the wire in DC1, which corresponds to the wire in DC6, which was hit.

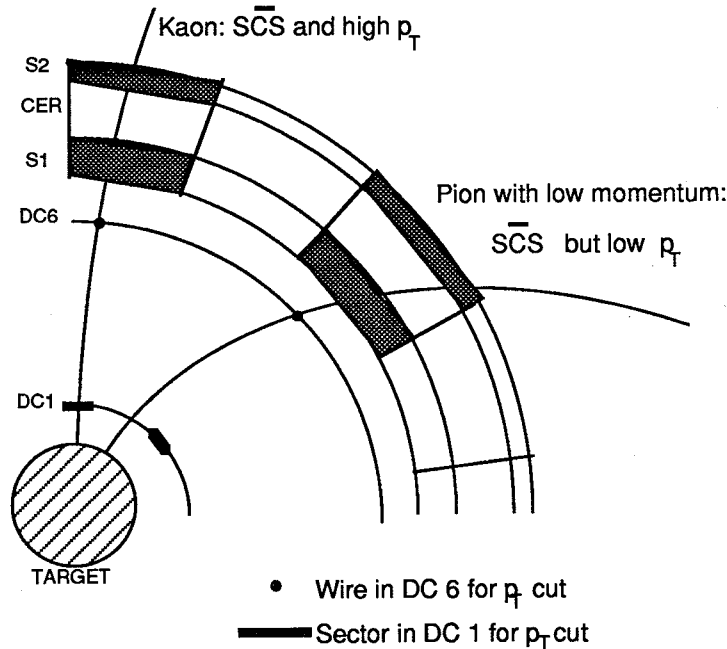


Figure 9: The idea of the p_t cut (not to scale)

⁶This introduces a momentum cut at 70 MeV/c, which is the minimum momentum for particles reaching S1.

Intermediate Decision Logic: IDL

The IDL is a test on:

- whether there are enough hits in the tracking chambers to be associated with tracks,
- the number of tracks.

These decisions are based on the hit maps of the tracking devices (PC and DC). (The hit map corresponds to a sectorization ⁷ of the circle into 64 segments.) The IDL gets from the FE the hit maps of PC1, PC2, DC1, DC2, DC5 and DC6. It then performs the OR of PC1 and PC2, DC1 and DC2, DC5 and DC6 in connection with the hit maps of S1 and \overline{SCS} . This yields the number of primary tracks N_{PT} , the number of charged tracks N_{CT} and the number of kaon tracks N_{KT} :

$$N_{PT} = (PC1 \text{ OR } PC2) \text{ AND } (DC1 \text{ OR } DC2) \text{ AND } (DC5 \text{ OR } DC6)$$

$$N_{CT} = (DC5 \text{ OR } DC6) \text{ AND } S1$$

$$N_{KT} = (PC1 \text{ OR } PC2) \text{ AND } p_T.$$

E.g. a sign of the golden channel is $N_{PT} = 2$, $N_{CT} = 2$ or 4 and $N_{KT} \geq 1$.

Track Follower

The track follower (TF) tries to follow each track from the outside (S1) towards the center (PC1), based on the sector hit map of each tracking device. If there is a hit in sector i , the hit map of the next inner chamber is searched for hits in the sectors $i-3, \dots, i+3$.

If a hit is found, the readout of the wire address and drift time in that sector is requested. So after the track follower stage the angles in the transversal plane ϕ_i of each hit on each track is available.

The TDC value of the ST is also read out for use in the kinematics (p_z), ϕ calibration and HWP 2 and 3.

Parametrization of the Track

The tracks can be parametrized in the transversal plane using a fast linear fit, yielding the curvature ρ , the distance of closest approach to the origin ϵ , and the starting angle φ in xy .

Kinematics

The oppositely charged tracks can be combined to calculate the missing mass for the primary tracks. However, it is expected, that a possible cut on the missing mass

⁷see table 3.

around the kaon mass would not lead to a significant data reduction.

If there are enough hits for the secondary tracks an invariant mass could be calculated.

Note, that there are two possibilities to combine four tracks into two pairs with opposite charge.

2.4.2 Hard Wired Processor 2: HWP 2

HWP 2 performs another test on the K/π identification of the primary tracks as done by the EDL. It is launched by the TC, after the results of the track parametrizations have been obtained.

HWP 2 gets from the PID FE the ADC value of S1 and Cer, the TDC value of S1, as well as the curvature and the z information from HWP1. It performs three tests:

- $(dE/dx)_{S1}$:
The expected energy loss is calculated from the track parametrization: $(dE/dx)_{calc}$. An experimental $(dE/dx)_{exp}$ is obtained from the ADC count of $S1_{upstream}$ and $S1_{downstream}$. The event will be rejected in case of a disagreement of the two values for kaons and pions.
- $(N_{phot})_{Cer}$: The number of photoelectrons in the Cerenkov is obtained by an analogous calculation for the kaon candidate track with the ADC value of the Cerenkov, corrected along z.
- Time of Flight (TOF): The TOF is given by the beam counter as a start signal and the S1 as stop signal. The TOF difference between primary tracks can be used as a further test to verify the K/π identification. Again the track parametrization is used to calculate the expected time of flight difference between the kaon candidate and the corresponding pion TOF_{calc} , which is compared with the TOF_{exp} obtained from the S1 TDC.

The result is passed to the TC, after those tests have been done.

2.4.3 Hard Wired Processor HWP 2.5

The main task of HWP 2.5 is to veto all events, where a K_L^0 decays outside the detector.

If two charged tracks have been identified, the TC issues a strobe to HWP 2.5 and requests the sector information from the calorimeter FE.

They are scanned by simple pattern recognition algorithms to find the number of

clusters for the wires ($NCLU_{wir}$) and the strips ($NCLU_U$ and $NCLU_V$) and the cluster feet.

The total number of clusters $NCLU_{cal}$ is calculated from $NCLU_{wir}$, $NCLU_U$ and $NCLU_V$ and, depending on its value, the event will be kept or rejected.

Furthermore each shower foot is calculated.

If the event survives to this stage, a general strobe is issued to start the transfer from the FE into the data acquisition chain (See chapter 3 for a details on the online system).

2.4.4 Hard Wired Processor 3 and 4: HWP 3 and 4

Two more processors are foreseen to work on the calorimeter data.

They get their input data from one of the output FIFOs of SPY or from HWP 2.5. Both will be implemented in software.

- HWP 3: calculates the exact shower foot coordinates and gets the number of gammas N_γ in the calorimeter, by subtracting the number of charged tracks N_{CT} from the number of clusters N_{clu} . Hardware wise it is made up of a multiprocessor VME crate.
- HWP 4: calculates the neutral vertex of the K^0 for events with $N_\gamma = 4$. The event will be rejected, if $t_{vertex} < 5\tau_s$.

The results of HWP 3 and HWP 4 are available after several milliseconds.

A module in the data acquisition chain (the event builder) keeps an event in its buffer, until it gets the results from HWP 3 and HWP 4. Then it either transfers it to tape or rejects it. (See chapter 3 for details on the online system.)

2.4.5 Trigger Decisions

The trigger control (TC) either accepts or rejects the event, depending on the outcome of the various tests mentioned above. The TC is not a static module. Its decision criteria can be changed from run to run, depending on the class of events required.

The master trigger, which all the events have to fulfill, is:

$$MT = (N_{PT} \geq 2) \text{ and } (N_{KT} \geq 1) \text{ and } (HWP2 \text{ ok}) \text{ and } (NCLU \geq N_0)$$

where N_0 is the required number of clusters found by HWP 2.5. It can be adjusted according to the trigger performance.

CPLEAR has two distinct data streams, which are independent of each other and have different trigger conditions, namely

- ϵ'/ϵ data stream,
- main data stream.

The ϵ'/ϵ **data stream** selects the data for the measurement of the integral asymmetries, from which ϵ'/ϵ will be calculated (eq. 2.7,2.8). Only data from HWP 1, 2 and 2.5 will be used. They are transferred through the SPY to a microprocessor system (called EPS VALET), which is connected to its own tape unit (see section 3.5).

The trigger condition for the ϵ'/ϵ data stream is

$$Trigger(\epsilon'/\epsilon) = MT.$$

The **main data stream** comprises the data from the various detectors, including the HWP data. The events in the main data stream are a complete subsample of the ϵ'/ϵ data stream events. Full advantage is taken of the versatility of the trigger, so many event classes can be acquired at the same time.

The events can then be grouped into:

- **CHARGED DECAY:** $K^0 \rightarrow \pi^+\pi^-$
 $MT * (MM \simeq m_{K^0}) * (N_{PT} = 2) * (N_{CT} = 4)$
- **NEUTRAL DECAY:** $K^0 \rightarrow \pi^0\pi^0$
 $MT * (MM \simeq m_{K^0}) * (N_{CT} = 2) * (\tau_{HWP4} \geq 5\tau_S)$
- **CHARGED 3 π DECAY:** $K^0 \rightarrow \pi^+\pi^-\pi^0$
 $MT * (MM \simeq m_{K^0}) * (N_{CT} = 4) * (N_{PT} = 4) * (IM \neq m_{K^0})$ for $\tau < 5\tau_S$
 $MT * (MM \simeq m_{K^0}) * (N_{CT} = 4) * (N_{PT} = 2)$ for $\tau > 5\tau_S$
- **NEUTRAL 3 π DECAY:** $K^0 \rightarrow \pi^0\pi^0\pi^0$
 $MT * (MM \simeq m_{K^0}) * (N_{CT} = 2) * (N_{PT} = 2)$
- **SEMILEPTONIC DECAY:** $K^0 \rightarrow \pi\mu\nu_\mu$
 $MT * (MM \simeq m_{K^0}) * (N_{CT} = 4) * (N_{PT} = 4) * (IM \neq m_{K^0})$ for $\tau < 5\tau_S$
 $MT * (MM \simeq m_{K^0}) * (N_{CT} = 4) * (N_{PT} = 2)$ for $\tau > 5\tau_S$

- ϵ'/ϵ SAMPLING MODE:

$$MT * (N_{CT} = 4) * (IM \simeq m_{K^0}) * SCALE$$

This mode is only used to acquire a subsample of the events of the ϵ'/ϵ data stream. SCALE is a possible scale factor.

where :

MM missing mass of the two primary tracks,

IM invariant mass of the two secondary tracks,

τ_{HWP4} lifetime as calculated by HWP 4.

3 The CPLEAR Data Acquisition System

This chapter has three main parts:

The first is dedicated to some general considerations for designing data acquisition systems. The data flow and physical location of the CPLEAR online system is also explained.

In the second part, the different parts of the data acquisition chain are described in more detail. The CPLEAR data acquisition system is based on the VALET PLUS, a VME based microprocessor system, which is described in appendix B. The different use of the VALETs is discussed.

The whole data acquisition is controlled from a VAX cluster. The communication procedure between the VALET and the VAX will be explained briefly in the last section of this chapter.

3.1 General Online Considerations

The online system must be able to handle the total data rate of the experiment, which depends on the average event size and the event rate.

CPLEAR has two independent data streams, as described in section 2.4.

For the main data stream an event size of approximately 2.4 kbytes is expected, which is split into the following data blocks for each detector:

- PC 200 by
- DC 500 by
- ST 200 by
- PID 200 by
- CAL 1000 by
- HWP 300 by

At the design stage the event rate can only be estimated, as the final rejection performance of the trigger and the background branching ratio of the $p\bar{p}$ -annihilation are not known. However, it was estimated, that CPLEAR would have an approximate rate of 800 events/sec to tape.

The event rate of the ϵ'/ϵ data stream is expected to be around 1000 - 2000 events/sec.

An event size of 200 - 400 bytes is anticipated.

In addition, other less scientific, but more 'worldly' constraints have to be considered in designing data acquisition systems of large experiments.

Between the detector and the tape may be a considerable physical distance. So data have to be moved over relatively large distances without being corrupted, especially in noise rich experimental halls.

A data acquisition system has to be sufficiently modular, so that different detectors can be switched off with minimum interruption.

LEAR is not a pulsed machine, but runs in DC mode, meaning a continuous data rate over periods of one hour or more. Therefore it is not possible to buffer the data on disk or memory during data taking phase.

Furthermore the price, and the fact that the components of the detector will be designed and tested in home institutes have to be considered. Choosing a sufficiently modular and simple system has the advantage, that detector groups become already familiar with the first stage readout of their specific detector, while building and testing it. This facilitates the final installation of the experiment, and also makes the addition of new detectors easier.

Based on these reasons it was decided to use the VME based microprocessor system VALET PLUS ⁸ extensively. It has been developed at CERN by the Data Division Online Computing group (DD/OC), so a large expertise and support is available on site. Before describing the hardware and software components of all these VALET PLUS's, we mention the three main stages of the data acquisition :

- Read out of each detector electronics (Front end) with one VALET PLUS (called RRO = Root Read Out) per detector.
- Transferring the individual detector data from the RRO into another VALET PLUS, which merges them into a full event in a specified format. This VALET is called Event Builder (EB).
- Transferring the data to tape and in parallel online monitoring on the full event. For this 3 VALET PLUS's are used. DDS (Data Distribution System) to distribute the data to the TAPE VALET and MSP VALET (MSP = Model Spider Producer).

⁸The VALET PLUS is described in appendix B, together with its CPU the FIC 8320.

So the data acquisition system can be characterized by distributed intelligence all over the system. Each RRO can perform online monitoring tasks on the detector, to which it is attached, while passing the data to the EB. In addition each RRO provides a mean to control the FE electronics, to which it is attached.

The run control of the VALETs is done centrally from a VAX cluster over ETHERNET. The VAX cluster comprises 3 MICROVAXES and 6 VAXSTATIONS. Histograms (e.g. hit maps) and other information (error messages, warnings) can be passed from the RRO to the VAX for monitoring purposes during data taking.

A slow control system, also running on the VAX cluster, monitors continuously the detector. High voltage, gas flow, beam shape etc are constantly checked. If a deviation from normal run conditions is found, an alarm message is sent. We will not describe it any further, as it will be treated in more detail in a coming publication [13].

Figure 10 shows the layout of the CPLEAR experiment in the LEAR hall.

The detector is located at the experimental beam line S1. Next to it are the front end and trigger electronics. RRO and EB are located in the barack EP16. EP23 is the CPLEAR control room with the following components of the data acquisition system: VAX cluster, tape units and the following VALETs: DDS, TAPE and MSP. The approximate distance from the area (S1) to the RROs (EP16) is 12 metres, from EP16 to the control room (EP23) about 25 metres.

Figure 11 shows the data flow of the data acquisition system, as it will be described in the following sections.

3.2 Root Read Out and Event Builder

When HWP 2.5 has finished its calculation and the event is still considered to be good by the trigger control, the transfer from the FE to the RRO is started, as described in the section 2.4 (figure 8). Home built differential bus extenders are used to transfer the data from the FE in the experimental area to the RRO in the barack EP16.

The RRO consists of a VALET and a 16 bit I/O module (STR 302)⁹. The Filtabyte

⁹Trademark of Antares AG, Schulstr.3, CH - 5415 Nussbaumen.

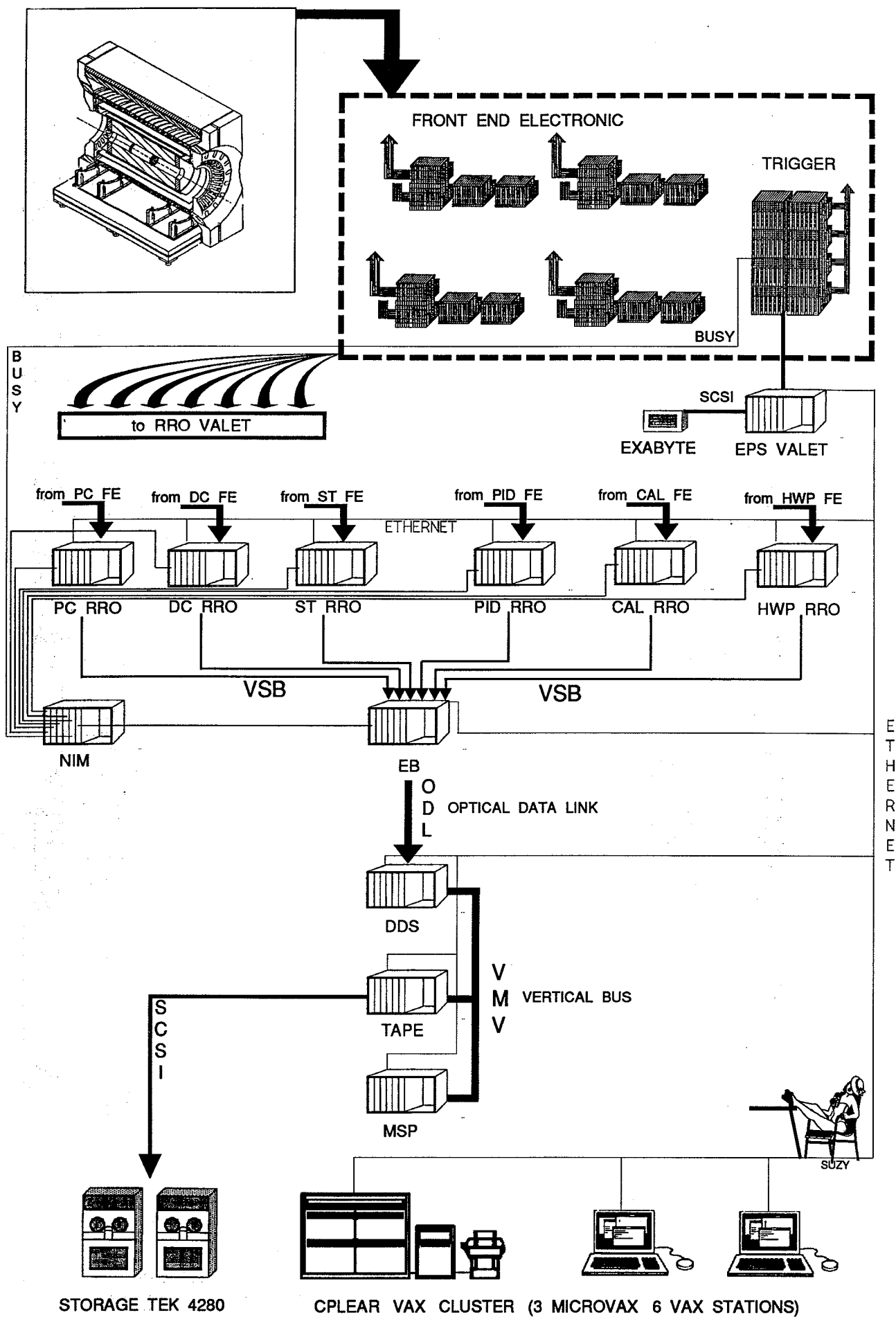


Figure 11: Data flow chart of CPLEAR data acquisition chain.

25.2C (LRT) ¹⁰ is used as ETHERNET interface for all the VALETs.

A special test pulse coming in parallel with the first word of an event generates an interrupt on the STR 302 (see figure 12). In the corresponding interrupt service routine (ISR) the data are transferred from the STR 302 I/O port into the event buffer, which is located in the onboard memory of the FIC. The end of transfer is given by another signal from the FE. The CPU now initialises the WE 32104 DMAC¹¹, which transfers the event over VSB ¹² to the EB.

Time critical ISRs are written in assembler and loaded into the SRAM of the FIC. Therefore their execution is fast. It is possible, to extract single events from the RRO buffer manager. This enables online analysis programs to monitor their specific detector performance in parallel to the actual data acquisition. All this less time critical code is written in PILS and executed in the global onboard memory of the FIC.

The EB consists of a VALET with 7 2SB ¹³ RAM cards, a LRT card, an ODL (Optical Data Link - see below) and a STR 302.

The ODL is used to send the data from the barack EP16 to the control room (barack EP23) - a distance of about 25 meters.

The 2SB is a 2 Mby RAM card. It is dual ported to VME and VSB with very fast access and cycle times ¹⁴.

Each detector's RRO has its own 2SB card in the EB crate, with which it is physically connected over VSB. The RRO WE 32103 DMAC transfers the event into its corresponding 2SB card, as mentioned above. The location of the event in the memory of the 2SB (i.e. its physical VME address) is determined by the cycling event number (CEN). This number is generated by the EB and written into every 2SB card at a well defined address at the start of an event for the following event ¹⁵. Each RRO reads this number, before the WE 32104 DMAC starts the RRO - EB transfer. Therefore the EB CPU knows the address of each detector block and can check, whether all the RROs have sent their event.

¹⁰Trademark of Logic Replacement Technology (LRT), Arkwright Road, GB - Reading RG2 OLU

¹¹This device is described in appendix B together with the FIC

¹²Vme Sub Bus

¹³Trademark of RADSTONE Technology, former PLESSEY, Water Lane, Towcester, GB - Northants NN12 7JN.

¹⁴Maximum access/cycle time or single read 248 ns / 277 ns

¹⁵This scheme might change in the future. A special card is in design stage, that would be present in all RRO and EB to generate the cycling event number simultaneously.

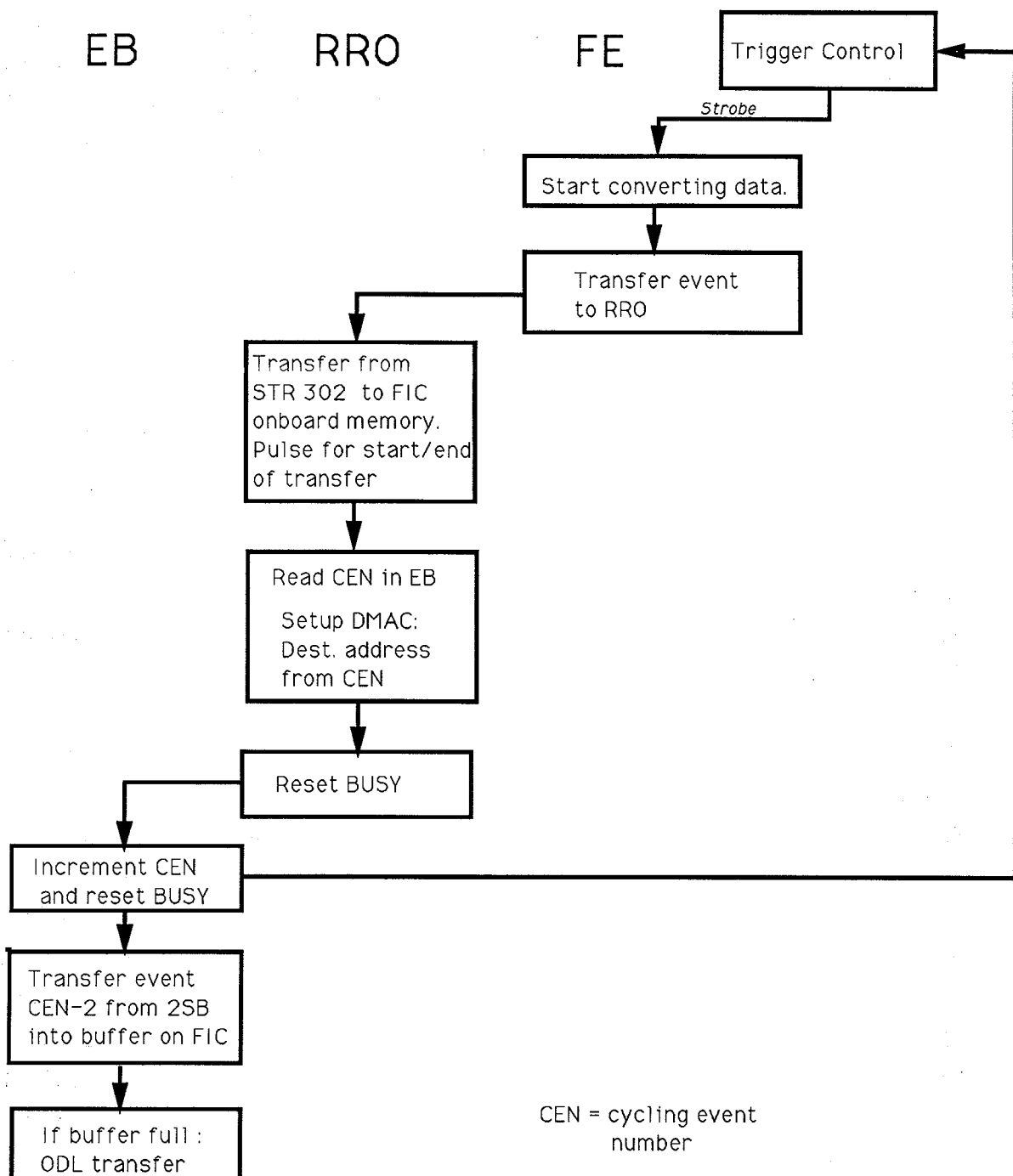


Figure 12: Transfer from the FE to the RRO and EB. The STR 302 module, a 16 bit I/O module, is used as interface between FE and RRO (VME bus). The RRO first transfers the data from the STR to the FIC onboard memory, and then to the EB, where the different data blocks are merged into one event and formatted.

As the data of a particular event arrives in the 2SB memory, the EB prepares a table with the starting addresses of the different detector data blocks. When the whole event is in the EB, this table is used to move the event into the global onboard memory of the FIC by a chained DMA transfer of the WE 32104. The event header is added and the ZEBRA data structure completed ¹⁶.

As soon as a whole ZEBRA data block of 23040 bytes has been built in that way, it is transferred over the optical link to the DDS VALET (Data Distribution System) in the control room.

As the EB mostly uses DMAC transfer for data handling, it is not necessary to write it in assembler. It is entirely written in PILS.

The communication between the trigger and the RROs is done using the output signals of the general purpose fast front panel connector of the FIC.

The trigger sets the BUSY high, if the event has to be read out. Each RRO outputs a RESET pulse on the front panel connector, after the event has been sent to the EB. Those RESET pulses produce an interrupt on the STR 302 in the EB, which is the start of event for the EB. The EB, in turn, first increments the CEN for the next event, reenables the trigger by a pulse on the STR 302 and then merges the detector data of event CEN - 2 from the 2SB cards into the ZEBRA block in his onboard global memory.

These signals are directed to a NIM crate, which is located next to the VALETs in barack EP16. Once all the RROs and the EB have given their RESET signal, the BUSY is released, and the trigger is ready for the next event.

This BUSY scheme will change in the future, when HWP 3 is operational.

HWP 3 (and 4) will be launched by the trigger control simultaneously with the data transfer from the FE via RRO to the EB (see chapter 2.3. for a description of the trigger). As it will take several milliseconds, before HWP 3 and 4 have finished their calculation, the trigger will be released beforehand. Therefore the event will be kept in the EB buffer, until the HWP 3 and 4 decision is available. If the event is marked as bad by one of those two processors, it will be rejected by the EB, otherwise transferred to tape.

¹⁶CPLEAR uses for offline use ZEBRA [14].

3.3 Data Distribution System

As the event buffers (i.e. ZEBRA blocks of events) arrive in the control room over the optical link, they have to be distributed to two consumers:

Firstly they have to be written to tape, secondly a subset of them has to be transferred to one of the microvaxes for full online event monitoring.

Tape writing has the higher priority of the two consumers. The solution adopted is to distribute the data blocks over the VMV (VME vertical bus)¹⁷ into two VALETs. One is only dedicated to writing to tape (TAPE VALET), whereas the other (MSP VALET)¹⁸ retrieves single events out of the ZEBRA buffer and sends them over Ethernet to the VAX. This transfer is rather slow (due to ETHERNET).

In terms of hardware the DDS, TAPE and MSP VALETs comprise:

DDS	FIC with 2 Mby memory, VBE 8213, VBR 8212, ODL and LRT
TAPE	FIC with 4 Mby memory, VBR 8212, LRT, SCSI interface, 2SB
MSP	FIC with 4 Mby memory, VBR 8212, LRT, 2 SB

Before discussing the actual data transfer, we give first a short description, how the VMV bus is used in this context. A detailed description of the VMV can be found in [15] or in the appendix B.3.

3.3.1 The Principles of the VMV

The CES VMV modules VBE 8213 and VBR 8212¹⁹ were choosen. They are described in appendix B.3.

Figure 13 shows the principles of the VMV operation, as CPLEAR uses it.

The VBE module occupies in the DDS a 1 Mby window in the VME address space. From the DDS point of view VME cycles in this address space look like an ordinary VME cycle. However, the cycle is propagated over the VMV into a VME cycle in

¹⁷More details about the VMV bus can be found in appendix B.3

¹⁸This name is 'historical': SPIDER is a simple data acquisition program written for the VALET in connection with CAMAC. MSP is a VAX program for the control of SPIDER and transfer of events from the VALET to the VAX. The program running in the MSP VALET is, however, a completely rewritten version of the original one. Only the name has remained unchanged.

¹⁹Trademark of Creative Electronic Systems (CES), rue du pont-butin 70, CH - 1213 PETIT-LANCY 1 / GENEVE.

the destination crate, which is selected by the value of a special VBE register. It is also possible, to write/read simultaneously to all the crates attached to the vertical bus.

Therefore the solution adopted to distribute the data from the DDS to the MSP and TAPE VALET is to locate all the common variables of those three VALET's, in particular the event buffer, in this VBE window. This means, that the DDS crate has full control over the input of the buffers, but geographically the buffers do not lie in its crate, but in the 2SB cards of the TAPE, MSP respectively.

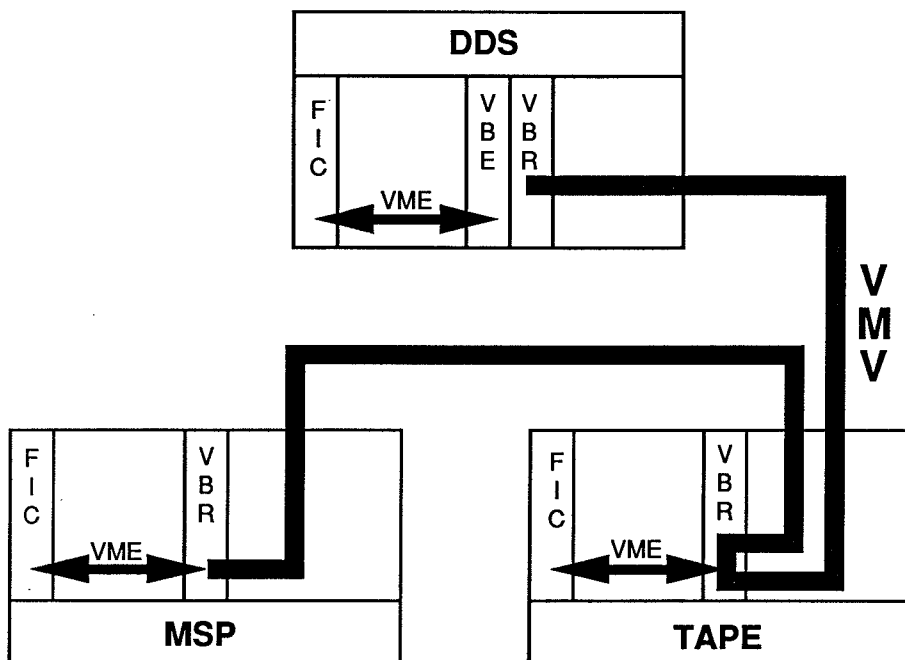


Figure 13: *Principle of the VMV operation. VME cycles done at the window of the VBE are propagated over the VMV bus into VME cycles in the destination crate. The latter is selected by the value of a special register in the VBE.*

3.3.2 The Data Transfers from EB to TAPE / MSP over DDS

The modules ODL 8142 are used as optical link between the EB and DDS. One module sits in each crate, and they are connected by two optical cables. Each module can be either the emitter or the receiver. Data as well as 15 different commands can be transmitted. If both arrive at the same time, the command has the higher priority.

The data is transferred from the FIFO (First In, First Out) of the emitting module into the FIFO of the receiving one. If the receiving FIFO is half full, the transmission is stopped. As soon as the FIFO is less than half full, it is resumed. The transmission is done automatically and independent of the user.

The ODL is connected to the FIC front panel general purpose connector. So its FIFO can be accessed either by the FIC CPU or the WE 32104 DMAC.

The interrupt commands of the ODL are translated into FIC front panel interrupts. The transmission of data is controlled by a CRC check, a more sophisticated check method than the parity bit one.

The transfer of data from the EB over the DDS to TAPE/MSP is done in the following way:

If the EB has finished building a complete ZEBRA data block, it sends a header with the transfer count over the ODL to the DDS. After the latter has initialised its DMAC, it requests the data block. The DMAC now picks the data byte after byte, as it arrives in the ODL FIFO, and moves it into an internal buffer. If an error exception occurs, the DDS asks the EB to retry.

After the data block has been moved into the FIC memory, it is DMA-ed into the VBE window. The register, which determines the destination crate on the VMV bus (TAPE and/or/neither MSP) is set up according to the shared status variables of DDS, TAPE and MSP. Timeouts on the vertical bus can occur, and are handled by the bus error exception subroutine, which is also described in the appendix B.3.

As mentioned above the transfer from MSP to the VAX is rather slow. So the MSP event buffer is most of the time full, and the DDS does not transfer any data to it.

If the event buffer in the TAPE is full (i.e. the transfer over the ODL and VMV is faster than tape writing), the DDS stops requesting data blocks from the EB. The data transfer is resumed, as soon as the TAPE has released one of its event buffers.

Optionally the DDS can check the ZEBRA structure of the data. If errors are found, the block can be thrown away. This check, which slows down the overall transfer rate, is normally only done in the setting up phase of a run.

A transfer rate of 2 Mby/sec has been achieved over the ODL and the VMV.

The DDS software is entirely written in PILS, with the exception of the bus error ISR, which is written in assembler (see appendix B.3 for a description of the bus error ISR).

3.4 TAPE and MSP VALET

After the DDS has transferred the data into the TAPE and MSP, it updates the shared status variables in both crates. Neither TAPE nor MSP have any influence on the input of data into their event buffers.

CPLEAR uses the STORAGE TEK 4280 as tape station with the option of two cassette writing units, both having the 211X autoloader. This unit is fully compatible with IBM 3480 cartridges. The autoloader uses magazines with a maximum of 10 3480 cartridges. Once one unit has reached the end of tape, writing is immediately continued on the other, while the first is rewound and unloaded.

The module CES SCSI 8230/4 is used as interface between the tape unit and the TAPE VALET. It is plugged into the front panel of the FIC, so again the transfer is done by the WE 32104 DMAC.

The MSP VALET continuously checks the ZEBRA structure of the event buffer. If errors are found, a message is sent to the VAX. In addition full events can be dumped on the screen, if a terminal is attached to the MSP - a useful tool for debugging.

A process on the VAX, called KENYA, demands in regular time intervals events from the MSP over ETHERNET. On average several events per second are transferred.

MSP can also optionally send only events with a given simple signature (say number of hits in S1), if events of a particular type are required to be accumulated on the VAX (e.g. for online calibration purpose).

KENYA injects those events into the Model Buffer Manager (MBM), an event buffer manager. Several consumers may then have access to this data. One example is the CPLEAR online event display. It is a reduced version of the offline event display, so the "offline software runs online".

Both TAPE as well as MSP software are entirely written in PILS.

3.5 The ϵ'/ϵ Data Stream

We first describe in this section the statistics required for the measurement of ϵ'/ϵ , leading to the online constraints for this kind of measurement.

In the second part we describe the EPS VALET, which handles the ϵ'/ϵ data stream.

3.5.1 Online Constraints

CPLEAR will measure ϵ'/ϵ using

$$\frac{\Re\epsilon'}{\Re\epsilon} \simeq \frac{1}{6} \left(1 - \frac{I_{00}}{I_{+-}}\right) \quad (3.1)$$

where I_f is the integral asymmetry, defined in eq. 2.7.

The upper integration limit for I_f is given by the detector dimension and is about $20\tau_s$. This does not introduce any bias, as the integral asymmetry is constant after $12\tau_s$ (only K_L^0 are left). In contrast to the measurement of the time dependent asymmetry also events with the neutral Kaon decaying at small lifetimes (i.e. $\tau < 5\tau_s$) are kept.

Note that the reconstruction of the vertex of the neutral Kaon is not required in this measurement. However, the detection efficiency as a function of lifetime for the $\pi^+\pi^-$ and $\pi^0\pi^0$ final states has to be taken into account.

The required statistics are several 10^9 $K \rightarrow \pi\pi$ events. Due to the large amount of data involved, using conventional technology for the data storage and offline analysis is not possible.

Therefore CPLEAR decided:

- To decouple the ϵ'/ϵ data stream completely from the main data stream of the experiment and to keep only the results of the trigger processors (section 2.4). This reduces the event size to 200 - 400 bytes/event.
- As this trigger data is precalibrated, the CPU time needed for offline analysis is reduced significantly.
- To write all events having a Kaon candidate (i.e. \overline{SCS} , p_T cut, HWP 2, HWP 2.5) and at least two charged tracks to tape (master trigger, page 28). This trigger condition leads to an expected event rate of 1000 - 2000 events/sec.

- To use 8 mm video cassettes as storage medium, each having a capacity of 2 Gby. This reduces the number of tapes by a factor of 10. In total about 1000 cassettes are required.
- To use one of the four output channels of the SPY (section 2.4) to transfer the ϵ'/ϵ data into a VALET PLUS (called the EPS VALET), which writes them on cassette (see figure 11).

3.5.2 The EPS Valet

In terms of hardware the EPS VALET consists of ²⁰:

- FIC 8230 with CES SCSI 8230/4
- STR 302 with 12 MHZ HD68450 DMAC
- LRT ethernet interface
- 2SB 2 Mby memory card.

The tape unit is the EXABYTE 8200 CTS ²¹. It is connected to the FIC front panel by the CES SCSI 8240/4 interface. The storage medium is 8 mm video cassettes. The capacity of 2 Gby per cassette is achieved using advanced helical scanning ²². The rate to cassette is 256 kby/sec at large blocksizes.

We describe now the data transfer from the SPY to the EXABYTE.

The output port of the STR 302 is connected to the SPY output FIFO. A special pulse from the SPY signals the start of transfer by generating an interrupt. In the corresponding ISR the FIC CPU initialises the STR 302 DMAC, which transfers the data into the event buffer. After the data has been read out, another pulse generates an interrupt, linked to the end of transfer ISR.

The buffer management is done using the four FIC communication FIFOs (see appendix B.2) by passing the pointers to the data input buffers between the FIFOs.

The STR 302 DMAC transfers the data over VME into the 2SB card. The 2SB in turn is connected to the FIC over VSB as well as VME (figure 14). This has the advantage, that the data transfer from the 2SB to tape, performed by the FIC WE 32104 DMAC, can be done over VSB, thus minimising VME arbitration.

²⁰See preceding sections for the description of those modules

²¹Trademark of EXABYTE Corp., 1745 38th Street, BOULDER, Colorado 80301, USA.

²²This technology writes very narrow tracks at a very accurate angle towards the edge of the tape medium, so the actual track length is much larger than the tape width. For more information see EXABYTE User Manual, available from the manufacturer.

The time critical code for the STR 302 ISR and FIFO ISR is written in assembler, tape writing and online monitoring in PILS.

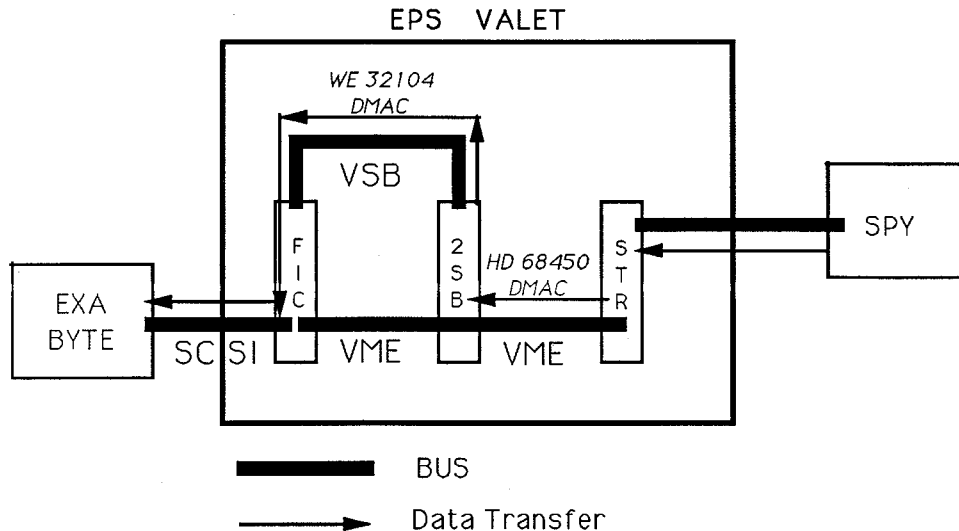


Figure 14: *Data transfer in the EPS VALET. The data is transferred into the 2SB memory by the STR 302 DMAC and to tape by the FIC WE 32014 DMAC.*

3.6 The Communication between the VALET and the VAX Cluster

CLEAR wrote its own package for the control of the VALET from the VAX.

It is based on KATE [16], a set of menus, which initiate the execution of commands by the VALET.

In so-called local mode the user enters the commands directly into a terminal emulator on the VAX. However, most of the time the VALET is not attached to a terminal, and the KATE commands are passed to the VALET over ETHERNET by a process called GAMBIA (figure 15). There is one GAMBIA per VALET, through which all the VALET-VAX communication is done. GAMBIA, in turn, gets the commands to be passed to the VALET from a set of shared resources (commons, event flags etc), called the PAC.

In principle any process has access to the PAC and may initiate a VALET command. However, there is one process per VALET, called SENIGAL, through which

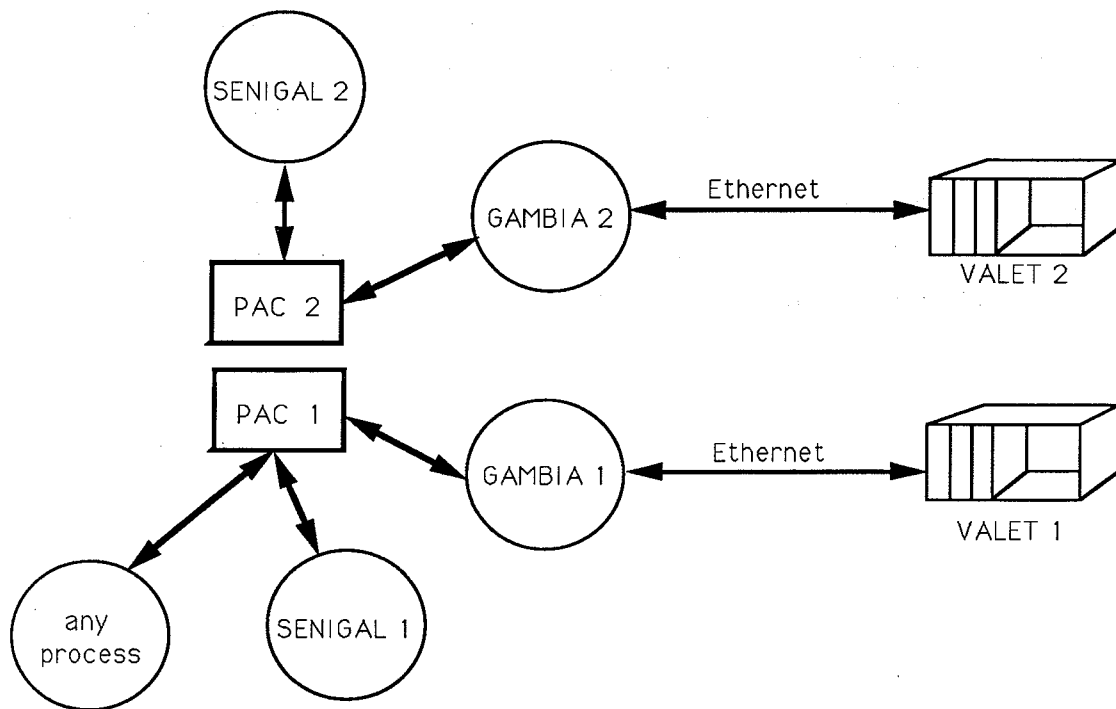


Figure 15: *Communication between VALET and VAX. There is one GAMBIA per VALET, which passes the commands to the VALET. GAMBIA gets its commands from a set of resources, called the PAC. Any process can access the PAC.*

many of the commands are passed. In addition SENIGAL can launch other processes, which then pass commands to the PAC.

As an example we discuss the run control. The user communicates with a top level process (DAKAR), which causes SENIGAL to launch a process, which contains all the commands to be passed to a given VALET, e.g. all the commands the VALET has to execute at the start of a run.

KENYA, already mentioned in the last section, is another example. The user asks SENIGAL to launch KENYA, which will then cause GAMBIA to ask the MSP VALET for new events. When the event has arrived on the VAX, KENYA will inject it into MBM, the Model Buffer Manager (see appendix B.1).

Finally we mention the histogram handling. The online monitoring programs of the RROs fill histograms with their detector data during a run. If the user, working in CPPAW (CPLEAR version of PAW - Physics Analysis Workstation [17]), wants to look at a histogram of a given VALET, CPPAW asks the SENIGAL of the corresponding VALET to cause GAMBIA to demand the histogram from the VALET.

Other VAX processes used in context with the VALET include a state manager, asking the VALETs in regular time intervals for status updates, automatic tape logging (as tape writing is done from the TAPE VALET), etc..

4 $p\bar{p}$ Annihilation into K^+K^- and $\pi^+\pi^-$

First we give an overview of the $p\bar{p}$ cascade and the current theoretical description of $p\bar{p}$ annihilation with emphasis on annihilation into $\pi^+\pi^-$ and K^+K^- .

Then the analysis of the annihilation channels

$$\begin{aligned} p\bar{p} &\rightarrow K^+K^- & (p_K = 797 \text{ MeV}/c) \\ p\bar{p} &\rightarrow \pi^+\pi^- & (p_\pi = 927 \text{ MeV}/c) \end{aligned}$$

is presented. (The momentum of the particles is given in brackets above.) This leads to a measurement of the relative branching ratio

$$R = \frac{BR(p\bar{p} \rightarrow K^+K^-)}{BR(p\bar{p} \rightarrow \pi^+\pi^-)} \quad (4.1)$$

in $p\bar{p}$ annihilation in gaseous hydrogen at 15 bar. Comparison with Monte Carlo simulation is done.

Combining our result of R with the absolute branching ratios for K^+K^- and $\pi^+\pi^-$ from atomic s and p level [18], allows the determination of the fraction of p wave annihilation at 15 bar.

4.1 Theoretical Introduction

This chapter consists of two parts:

First we describe the formation and cascade of the $p\bar{p}$ atom (protonium). In particular it is explained from which initial atomic states the annihilation occurs and its dependence on the target pressure.

In the second part we first mention the selection rules for the $p\bar{p}$ annihilation into $\pi^+\pi^-$ and K^+K^- and then describe briefly the $p\bar{p}$ -annihilations in terms of the quark model. Special emphasis is put on annihilation into $\pi^+\pi^-$ and K^+K^- .

4.1.1 Formation and Cascade of the Protonium

When a (non-relativistic) \bar{p} enters a hydrogen target, it starts losing energy by ionization loss.

Wightman [20] calculated the moderation time for negative particles in liquid and gaseous hydrogen from 10 MeV/c down to $\beta = v/c = 5 \cdot 10^{-2}$, obtaining $1.92 \cdot 10^{-7}$ sec for \bar{p} . (For lower β the stopping power formula becomes invalid, as the \bar{p} momentum is approximately equal to that of the electron in the hydrogen.)

Once the \bar{p} has been slowed down to the velocity of the electron in H_2 ($\simeq \frac{e^2}{\hbar}$), it is captured by a proton at a distance of the Bohr radius a_B . This corresponds to an energy level of

$$n \simeq \sqrt{m_{red}} = \sqrt{\frac{M_p}{2m_e}} \simeq 30$$

where m_{red} is the reduced mass of the $p\bar{p}$ system.

The following processes occur after capture, partly in parallel:

- Chemical deexcitation
- Coulomb deexcitation
- Auger transition
- Radiative deexcitation
- Stark mixing
- Annihilation

CHEMICAL DEEXCITATION: The $p\bar{p}$ system loses energy by chemical dissociation of neighbouring H_2 molecules:



The rate is given by [21]

$$\Gamma_{if}(chem) \simeq \frac{1}{2} N v \pi a_{n_i}^2 \quad \text{if } \Delta E > \Delta E_D \quad (4.3)$$

where:

N is the density of the hydrogen,

a_{n_i} is the radius of the n_i -th Bohr radius,

v the velocity of the $p\bar{p}$ atom,

ΔE energy loss of the $p\bar{p}$ atom,

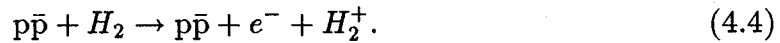
ΔE_D dissociation energy of the H_2 molecule = 4.7 eV.

It is seen, that $\Gamma_{if}(chem)$ plays only an important role for high energy levels n (a_{n_i} large).

The $p\bar{p}$ atom acquires a kinetic energy of $\simeq 1\text{eV}$ in this process [22].

COULOMB DEEXCITATION: The radius of the $p\bar{p}$ atom is inversely proportional to the reduced mass, therefore about 900 times smaller than the radius of the H atom. Thus the tiny $p\bar{p}$ atom will move through the electronic shells of neighbouring H_2 molecules. If the electrostatic interaction is comparable with the energy gap between different atomic levels, transitions of the $p\bar{p}$ to energetically lower states can occur. Thus Coulomb deexcitation is expected to be relevant only at high energy levels. Coulomb deexcitation becomes less important, the heavier the exotic atom is [23]. Therefore it is often neglected in cascade calculations, like e.g. [24].

AUGER DEEXCITATION: The $p\bar{p}$ system transfers in this process part of its energy to the electron of a neighbouring H_2 molecule, which is accelerated away:



Given the energy difference of a $p\bar{p}$ atomic level and the ionization energy of H_2 , Auger deexcitation leads mainly to small changes of the energy level of the $p\bar{p}$ atom. The rate is approximatively described by [21]:

$$\Gamma_{if}(Auger) \simeq \frac{16}{3} \frac{N}{M_{red}^2} R_{if}^2 (2\Delta E + 1.39)^{-0.5} \quad \text{if } \Delta E > 15.2 eV \quad (4.5)$$

where:

M_{red} is the reduced mass of the p atom,

R_{if} matrix element of the transition.

RADIATIVE DEEXCITATION: (Emission of light) Its rate is given by [21]

$$\Gamma_{if}(rad) = \frac{4}{3} \alpha h^{-1} M_{red}^{-2} R_{if}^2 (\Delta E)^3 \quad (4.6)$$

It follows, that radiative deexcitation favours large changes of the energy level n . Radiative deexcitation follows the selection rule $\Delta l = \pm 1$, where Δl is the change of the angular momentum²³.

Target properties determine the relative weight of Auger and radiative deexcitation. For liquid H_2 radiation processes were calculated to become important for pionic atoms only at $n > 3$ [25], for gaseous H_2 at 1 bar at $n < 6$ [21]. Given the dependence of $\Gamma_{if}(rad)$ and $\Gamma_{if}(aug)$ on the reduced mass and pressure, one can expect, that for a gaseous H_2 at 15 bar radiative transitions occur at similar low values of n .

²³Note, that the radiationless transitions don't respect any selection rule.

STARK MIXING: As the $p\bar{p}$ penetrates the electronic shells of the neighbouring H_2 molecules, it experiences the electrical fields of these molecules. This induces Stark transitions between the degenerate angular momentum eigenstates of the given energy level. A state $|n, l, m\rangle$ makes transitions into $|n, l \pm 1, m\rangle$ or $|n, l, m \pm 1\rangle$ ²⁴. It can be shown [26], that a typical collision time is much bigger than the time needed for a Stark transition. Therefore the mixing is maximal. The collision rate is dependent on the target density, being maximal in liquid H_2 .

Special attention has to be given to Stark transitions into the atomic s and p states, as these are shifted by the strong interaction. Therefore in addition to the change of angular momentum, there is a shift in energy, what hinders Stark transitions into these levels. As the strong interaction energy shift for s and p level is given by

$$\delta E_{ns} \simeq \delta E_{1s} n^{-3} \quad (4.7)$$

$$\delta E_{np} \simeq \delta E_{2p} \frac{32 n^2 - 1}{3 n^5} \quad (4.8)$$

this becomes only important at the very lowest energy levels [25].

ANNIHILATION: Annihilation occurs, as soon as the wave functions of the \bar{p} and p overlap sufficiently. The annihilations from atomic d states can be neglected [27]. Therefore only annihilations from atomic s and p states are important. The rates are given by

$$\Gamma_{ns} \simeq \frac{\Gamma_{1s}}{n^3} \quad (4.9)$$

$$\Gamma_{np} \simeq \frac{32 n^2 - 1}{3 n^5} \Gamma_{2p} \quad (4.10)$$

CASCADE TIME: The cascade time of a $p\bar{p}$ atom has been measured at NTP (pressure $p = 1$ bar, $T = 0$ C) to be 5.1 ± 0.7 ns [24]. Cascade calculations indicate the cascade time at 15 bar to be of the order of 0.1 ns [24].

It can now be understood, how the target properties affect the above mentioned processes: At high target density the tiny $p\bar{p}$ atom spends a significant amount of time within other hydrogen molecules. Therefore many Stark transitions take place. So annihilation can occur, as soon as the \bar{p} is in an s state, even at a high excitation

²⁴The change in m is due to the rotation of the \vec{E} -field (that means quantization axis) as seen from the $p\bar{p}$ atom during the collision. However, this effect is rather small [25].

level n (Day-Snow-Sucher-effect [26,28]).

On the other hand in low pressure target ($p \ll 1$ bar) annihilations from p levels will become dominant. This can be understood as follows (figure 16):

Radiative transitions are the dominant process, if $p \ll 1$ bar. As they favour large changes of the energy level n (eq. 4.6), the $p\bar{p}$ atom will most likely end up in the highest angular momentum state of a given energy level n . Once it has dropped to such a level $|n, l = n - 1\rangle$, its transitions are $|n, l = n - 1\rangle \rightarrow |n' = n - 1, l' = l - 1 = n' - 1\rangle$ (selection rule $\Delta l = l' - l = \pm 1$). Annihilation will take place, once it has reached the $2p$ level, as annihilations are unlikely from atomic d levels (see above) and the radiative transition from the $2p$ level to the $1s$ level is suppressed [29].

However, Stark mixing continues playing an important role even at low pressures. E.g. it has been measured [18], that at NTP about 50 % of the $p\bar{p}$ annihilations still take place from atomic s states.

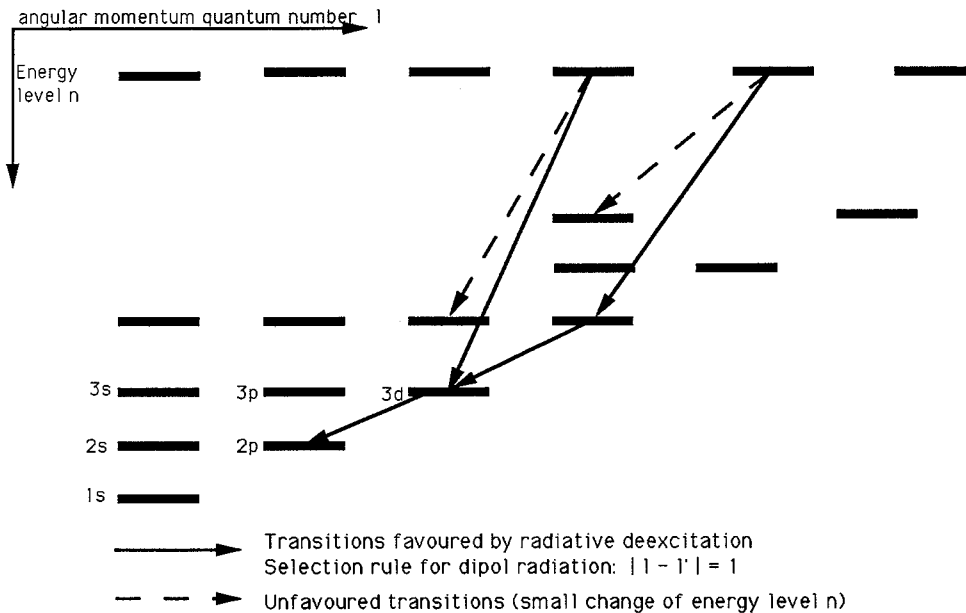


Figure 16: Radiative transitions lead mainly to annihilation from the atomic $2p$ level at low pressure ($p \simeq 0$ bar).

We will not discuss the dependence of the annihilation initial state on target properties any further and defer a more detailed discussion to the last section of this chapter.

4.1.2 $p\bar{p}$ Annihilation

$p\bar{p}$ annihilation has always attracted a special interest, because it is a simple system to study the nucleon antinucleon physics at low energies, and in particular the annihilation mechanism. The first systematic investigations were carried in the 1960s using bubble chambers. Thus the bulk of experimental data consists of annihilation in liquid hydrogen, that means overwhelmingly annihilation from atomic s level [30]. With the high flux of low energy antiprotons at LEAR, study of $p\bar{p}$ in gaseous hydrogen has become feasible.

Before concentrating on the annihilation into two meson final state, it should be pointed out, how they relate to the other channels. Multipionic final states (4, 5 or 6 pions) are produced in about 50 % of the $p\bar{p}$ annihilations, but the possible intermediate resonances in these final states are only vaguely known. On the other hand production of strange mesons is around 1%.

Special interest is given to the annihilation into two mesons, as it is the simplest final state, and therefore an ideal testbed for theoretical models. A special subclass of two meson final states is annihilation into a particle and its antiparticle, e.g. $\pi^+\pi^-$, $\pi^0\pi^0$ etc. Their branching ratio is very low, around 10^{-3} .

4.1.2.1. Selection Rules for Annihilations into K^+K^- and $\pi^+\pi^-$

Discrete symmetries lead to selection rules for $p\bar{p}$ -annihilation. For a $\bar{N}N$ system the P, C and G (parity, charge conjugation and G parity) eigenvalues are [30]:

$$P = (-1)^{L+1} \quad C = (-1)^{L+S} \quad G = (-1)^{L+S+I} \quad (4.11)$$

where:

- L is the angular momentum of the $\bar{N}N$ system,
- S is the spin,
- I is the isospin.

For a $\pi^+\pi^-$ or K^+K^- the eigenvalues are:

$$P(\pi^+\pi^-) = P(K^+K^-) = (-1)^l \quad (4.12)$$

$$C(\pi^+\pi^-) = C(K^+K^-) = (-1)^l \quad (4.13)$$

$$G(\pi^+\pi^-) = G(\pi)G(\pi) = 1 \quad (4.14)$$

where l is the angular momentum for the $\pi^+\pi^-$ and K^+K^- .

Note, that charged particles (like π or K) are not eigenstates of the charge conjugation operator C . The G eigenvalue is also not defined for the K , as it is a strange particle.

Table 4 summarizes the possible initial states for the $p\bar{p}$ -annihilation. It shows, that the following initial states for the reaction $p\bar{p} \rightarrow \pi^+\pi^-$ or $p\bar{p} \rightarrow K^+K^-$ are possible:

$$\begin{array}{ll} \pi^+\pi^- & {}^{33}S_1, {}^{13}P_0, {}^{13}P_2 \\ K^+K^- & {}^{33}S_1, {}^{13}P_0, {}^{13}P_2 \text{ AND} \\ & {}^{13}S_1, {}^{33}P_0, {}^{33}P_2 \end{array}$$

with the following notation $(2I+1)(2s+1)L_J$. Due to the absence of G parity constraints K^+K^- production is possible from more initial states than $\pi^+\pi^-$.

Table 4: Possible initial states for $p\bar{p}$ -annihilation into $\pi^+\pi^-$ and K^+K^- . The violated symmetry is noted, where the initial state is forbidden.

$p\bar{p}$	P	C	G	$\pi^+\pi^-$	K^+K^-
${}^{11}S_0$	-	+	+	P	P
${}^{31}S_0$	-	+	-	G,P	P
${}^{13}S_1$	-	-	-	G	✓
${}^{33}S_1$	-	-	+	✓	✓
${}^{11}P_1$	+	-	-	G,P	P
${}^{31}P_1$	+	-	+	P	P
${}^{13}P_0$	+	+	+	✓	✓
${}^{33}P_0$	+	+	-	G	✓
${}^{13}P_1$	+	+	+	P,C	P,C
${}^{33}P_1$	+	+	-	G,P,C	P,C
${}^{13}P_2$	+	+	+	✓	✓
${}^{33}P_2$	+	+	-	G	✓

4.1.2.2. Theoretical Models for $p\bar{p}$ Annihilation into Two Mesons

Within the Standard Model the strong interaction is described by QCD. But its perturbative approach, which does so well at high energies, cannot be used to explain low energy phenomena, where the quarks are confined and many quarks and gluons are involved in the processes.

$p\bar{p}$ annihilation into two mesons is of special interest to test theoretical models, as it provides the most simple annihilation mechanism and a large amount of experimental data is available.

The channels under consideration in the present analysis,

$$p\bar{p} \rightarrow \pi^+\pi^- \quad \text{and} \quad p\bar{p} \rightarrow K^+K^-$$

are of particular interest, as an $\bar{s}s$ quark pair has to be produced in the latter reaction. Therefore the comparison of those two channels reveals information about strangeness production.

Two experimental features of those two annihilation channels, which should be explained by theoretical models, are:

- Dependence of the ratio

$$R(i) = \frac{BR(p\bar{p} \rightarrow K^+K^-)}{BR(p\bar{p} \rightarrow \pi^+\pi^-)}$$

on the initial state $|i\rangle$. The absolute branching ratios from initial atomic s and p state have been measured [18,19]. It was found, that the K^+K^- final state is suppressed by a factor of four in the p wave initial state compared to the s wave initial state. On the other hand the $\pi^+\pi^-$ final state is enhanced in the p wave annihilation compared with the s wave annihilation by about 50 %.

- The angular momentum distribution was measured as a function of initial \bar{p} momentum in the range of 360 - 760 MeV/c [31]. A peak in the forward direction was seen for $\pi^+\pi^-$, whereas momentum of around 500 MeV/c.

Within the framework of the quark model two graphs contribute to the reaction $p\bar{p} \rightarrow 2 \text{ mesons}$. They are shown in figure 17.

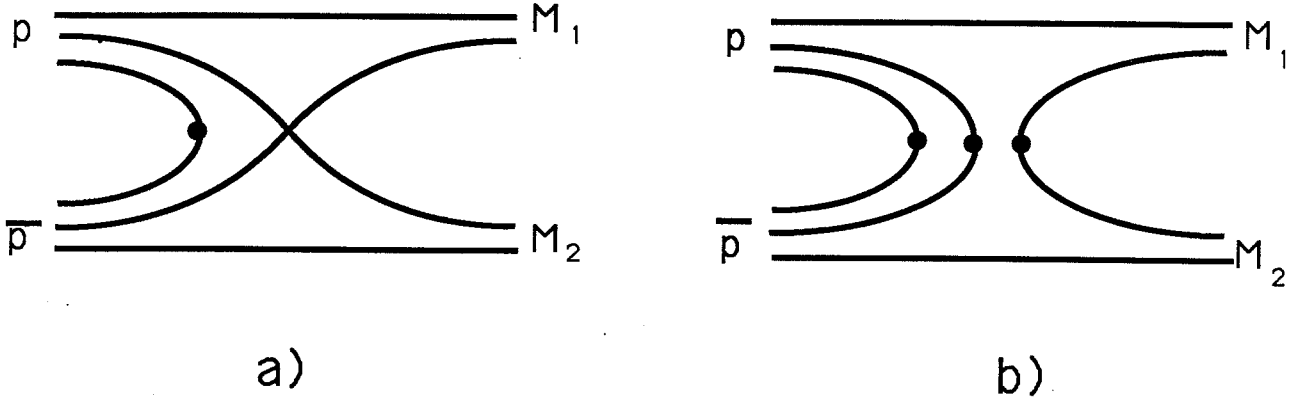


Figure 17: *Rearrangement (a) and annihilation or planar graph (b) contributing to $p\bar{p} \rightarrow 2$ mesons. The dots indicate quark-quark annihilation/creation vertices. Only (b) contributes to $p\bar{p} \rightarrow K^+ K^-$.*

17a is called rearrangement or R-graph, 17b annihilation or A-graph (or planar graph as the quark lines do not cross). At high energies A graphs are expected to dominate over R graphs [32].

The two main questions involved in the theoretical description of the $p\bar{p}$ annihilation into two mesons are:

- what is the relative weight of the rearrangement to the annihilation graph
- what is the quark antiquark configuration at their vertex.

Two models are used for to describe the $q\bar{q}$ vertex: The 3P_0 and the 3S_1 model. Figure 18 shows the corresponding vertex graphs.

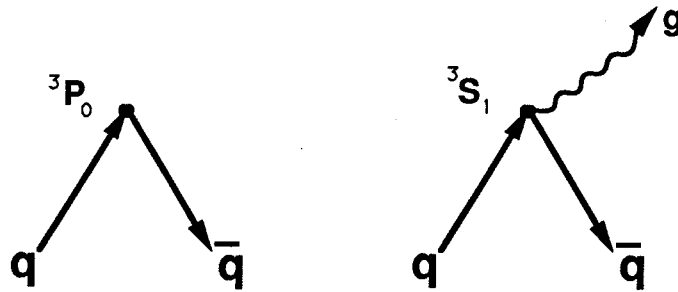


Figure 18: $q\bar{q}$ vertex graph: Left: 3P_0 vertex, where the quarks annihilate into the vacuum, right: 3S_1 , where the quarks annihilate into a gluon.

In the 3P_0 model the $q\bar{q}$ pair annihilate directly into the vacuum, in the 3S_1 model into a gluon, which can couple either to a $\bar{q}q$ production vertex or be absorbed by a

spectating quark. So in the 3P_0 model the other quarks are pure spectators, in the 3S_1 they interact with the gluon.

Meson and meson baryon coupling constants have been successfully described with the 3P_0 model. However, if it is applied to $p\bar{p} \rightarrow 2$ mesons reaction, its amplitude for the transition $p\bar{p}(L=0) \rightarrow M+M$ (S-wave) is zero in lowest order. (The 3P_0 model gives only in third order a nonvanishing contribution [33].) On the other hand the 3S_1 model for the $q\bar{q}$ vertex gives a nonvanishing contribution to first order.

Finally a word about initial and final state interactions, i.e. the proton-antiproton interaction before the annihilation and the interactions of the two outgoing mesons. They distort the wavefunction and have to be taken into account in the calculations. The initial state interactions of the $p\bar{p}$ can be described by a pionic exchange potential. (In this picture a pionic cloud surrounding the three quarks (antiquarks) gives a initial long range (2-4 fm) interaction of the $p\bar{p}$.)

Various attempts have been made to describe, theoretically, the $p\bar{p}$ annihilation into two or three mesons, but no common framework exists. The calculations yield different results, depending on the initial assumptions of the quark vertex (3P_0 or 3S_1), the quark line graphs (R or A graph) and other assumptions.

Kohno and Weise [34] calculated $p\bar{p} \rightarrow \pi^+\pi^-$ and $p\bar{p} \rightarrow K^+K^-$ in a nonrelativistic quark vertex with a 3S_1 model. They found that the R and A graph are of equal importance at rest, while the R graph loses in importance at higher momenta. They calculated the differential cross sections of $p\bar{p} \rightarrow \pi^+\pi^-$ and $p\bar{p} \rightarrow K^+K^-$ [35]. For $\pi^+\pi^-$ they found contributions from the A and R graph. The forward peak is reproduced for K^+K^- and $\pi^+\pi^-$, but not the K^+K^- backward one. A K^+K^- suppression was obtained for annihilation from initial atomic p level, in agreement with experimental data.

Maruyama and Ueda calculated the amplitudes for $p\bar{p}$ annihilation into 2 mesons for the R-graph [36] and the two possible A-graphs [37] with a 3S_1 vertex. Their calculation reproduces well the shape of the cross section for $p\bar{p} \rightarrow \pi^+\pi^-$ and $p\bar{p} \rightarrow K^+K^-$. The K^+K^- peak is present, but not as pronounced as in the data. They also included the possibility of a contribution from an A-graph with a 3P_0 vertex in their study. They find that such a contribution would be small. For annihilation in flight $L=2$ process (L being the initial angular momenta of the $p\bar{p}$ atom) dominates in this

model and the R-graph is not important. For annihilation at rest, the R-graph can give an important contribution depending on the annihilation channel. Their value of $\frac{BR(p\bar{p} \rightarrow K^+ K^-)}{BR(p\bar{p} \rightarrow \pi^+ \pi^-)}$ is in rough agreement with the data (about $\frac{1}{3}$).

Ellis, Gabathuler and Karliner proposed an interesting explanation for the $K^+ K^-$ backward peak [38]. Results from deep inelastic polarized μp scattering [39] and from the so-called $\pi - N$ sigma term [40,41] indicate the possible existence of a sea of $\bar{s}s$ quarks within the proton. This leads the authors of [38] to the conclusion, that the OZI rule²⁵ might not apply to baryons and the $K^+ K^-$ backward peak could arise from a reaction as pictured in figure 19.

To summarize it can be stated, that the form of the vertex, possible dominations of certain graphs as well as new extensions are still open questions.

As CRYSTAL BARREL [42] and OBELIX [43] at LEAR are starting to take data, new experimental data will be available soon.

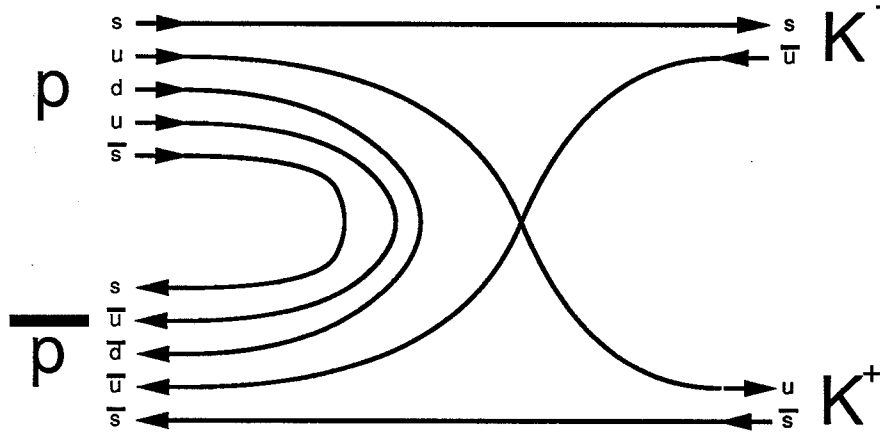


Figure 19: $K^+ K^-$ backward peak explanation as made by Ellis et al [38].

²⁵The OZI rule states, that amplitudes of processes with unconnected quark lines are suppressed.

4.2 Analysis of the Relative Branching Ratio $R = \frac{BR(p\bar{p} \rightarrow K^+ K^-)}{BR(p\bar{p} \rightarrow \pi^+ \pi^-)}$

4.2.1 Some Initial Remarks on the CPLEAR Offline Package

The CPLEAR coordinate convention, to which we will refer in this chapter, has been described in section 2.3.1

The CPLEAR offline package is based on the ZEBRA bank system.

The digitised data for each detector is first written into the RAW bank. Decoding and translation processors read this RAW bank and fill the COR banks, where the data is available in natural units.

The "pattern recognition" package identifies the single tracks out of the individual detector hits.

The fit processor uses the information of the TRA bank to calculate the parameters of the helix in space and thus the momentum of the charged particle. Multiple scattering is taken into account in the fit. If the χ^2 of the fit is too bad, the point giving the largest contribution to it, is removed, and the fit redone. If the χ^2 is still too large after two iterations, a special algorithm, which handles the kinks, is called. One FIT bank per track is filled, if the fit was successful.

The Monte Carlo package (CPGEANT) is based on GEANT 3 [44]. The results of the tracking of the particles in the detector are stored in the TRU bank. The detector simulation translates this information into the COR bank. From then on the Monte Carlo data is processed by the same pattern recognition and fit routines as the real data.

4.2.2 Data Reduction

This analysis was done with data taken in December 1989. An overview of the detector performance is given in appendix C, a more detailed description can be found in [7].

Two triggers were used:

- Trigger 7: At least one $S\bar{C}S$ hit in the PID
- Trigger 1: At least one hit in S1 ²⁶ (minimum bias trigger)

²⁶The detector abbreviations, to which we refer in this chapter, have been defined in chapter 1.

198 tapes of trigger 7 and 30 tapes of trigger 1 were taken in December 1989.

Figure 20 shows the data reduction from the raw data tapes to the back to back sample, as it will be discussed in this and the next section.

DST were produced for the events satisfying the following conditions:

- 2 or 4 tracks found by the pattern recognition package.
- z-information on either DC6 or streamer tubes.
- Sum of the charges of the tracks is zero (where charge refers to the charge as found by the pattern recognition package).

19 DSTs of trigger type 1 were further processed using a 'back to back' filter with the following conditions:

- 2 tracks found by the pattern recognition and the fit was done successful for both tracks.
- Cut on the opening angle in the transversal plane:
The momentum of both tracks was extrapolated to the point of closest approach to the z-axis. φ_{xy} was defined as the angle between the extrapolated momenta in the xy plane. It was required, that

$$\varphi_{xy} > 170^\circ. \quad (4.15)$$

- Back to back cut along the z-axis, as the particles come from the target:

$$|z_1 + z_2| < 20cm \quad (4.16)$$

where z_i is the z-information of track i of either the streamer tubes or DC6.

2 tapes of back to back candidates were obtained in this way.

Events on those tapes are from now on called back to back candidates.

Figure 21 shows as an illustration one back to back event and one background event of the obtained sample.

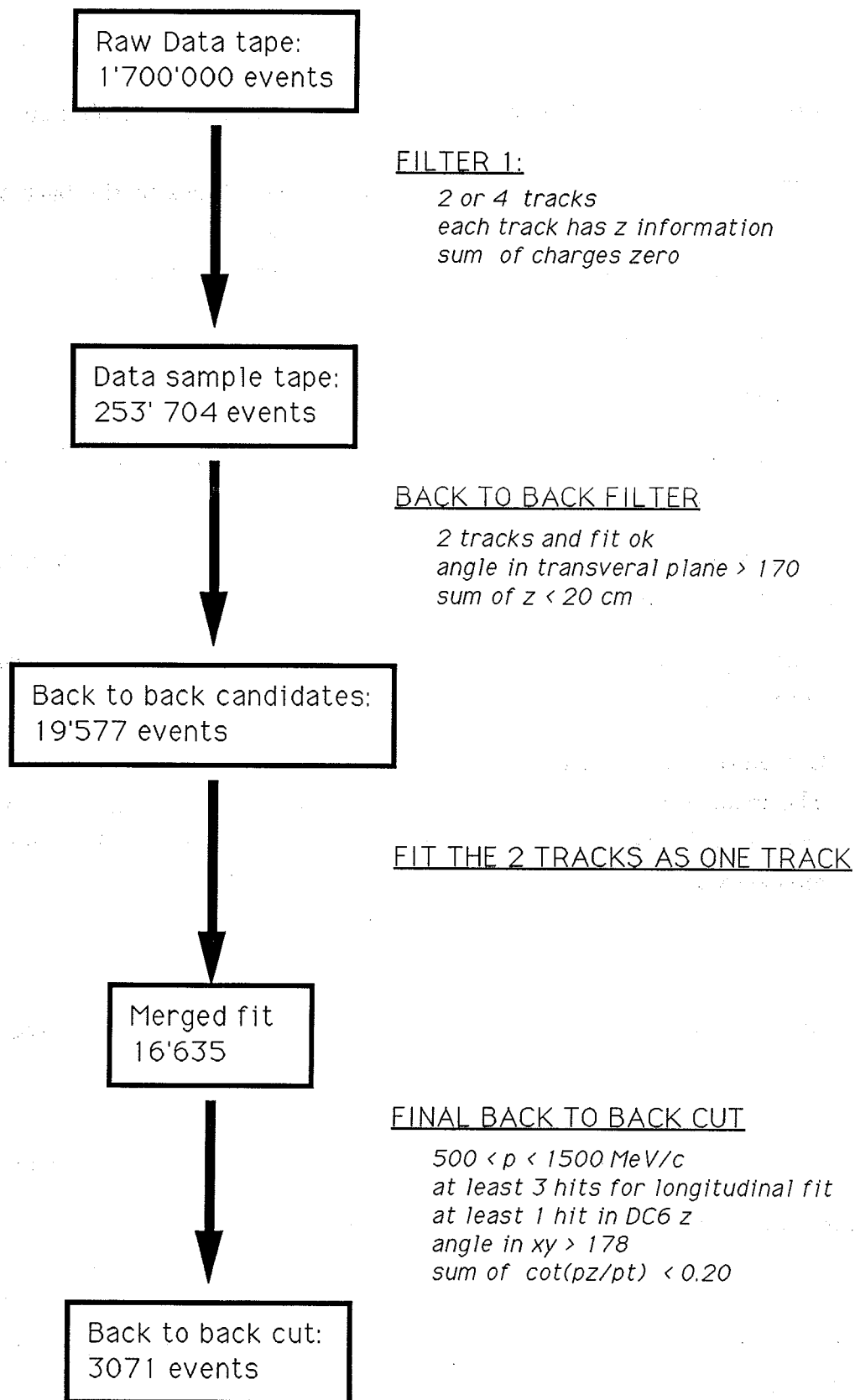


Figure 20: Data reduction from the raw data tape to the data summary tape (DST) and then to the back to back filter. About 3000 events were left after the main back to back cut.

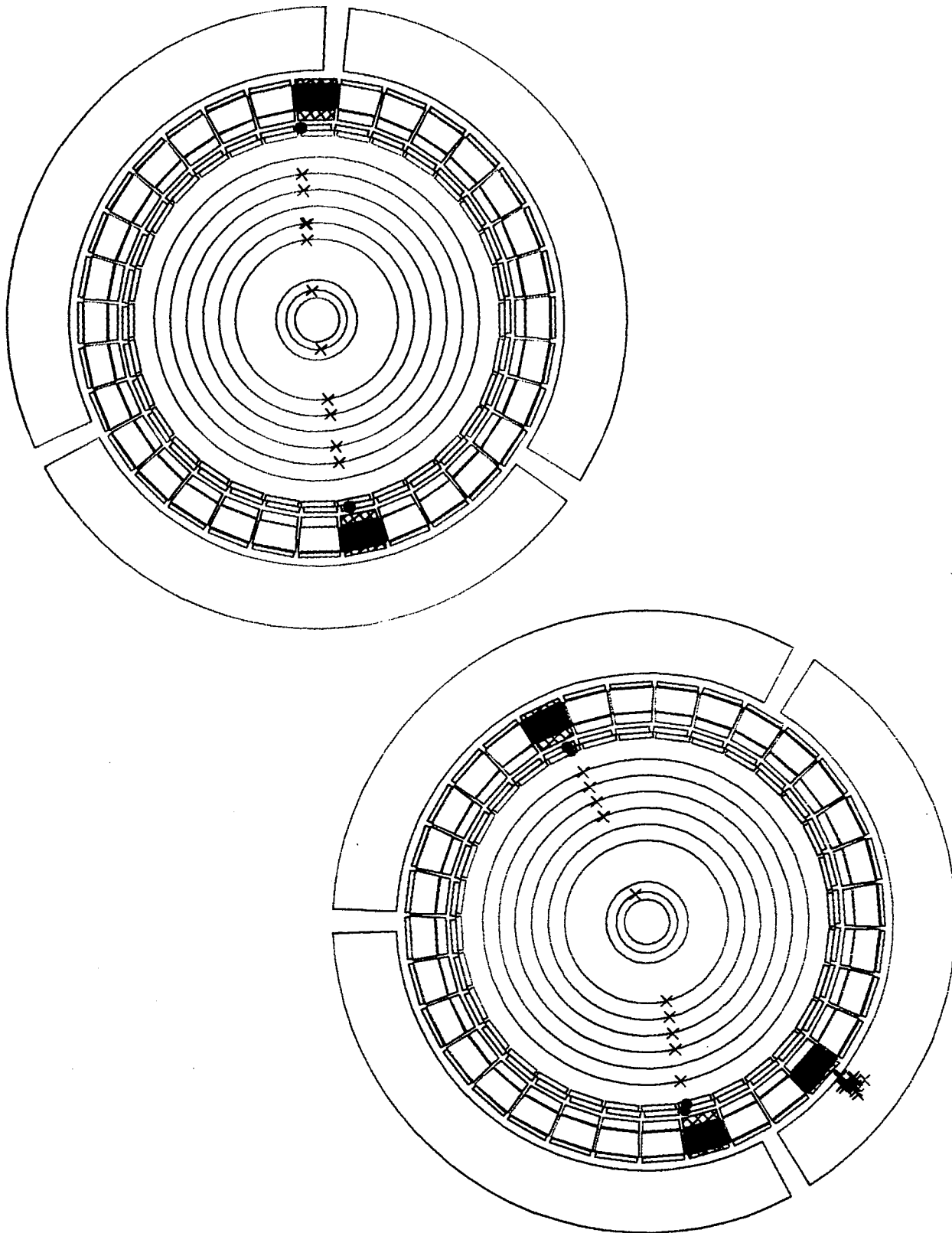


Figure 21: Offline event display of two events: The first is a typical back to back event, the other a background event. The existence of more particles in the latter is confirmed by the calorimeter at bottom right.

4.2.3 Back to Back Selection

Figure 22 shows the distribution of the momenta of the two tracks of the back to back candidates. A clear enhancement in the region between 700 - 1100 MeV/c is seen, where the back to back events are expected (797 MeV/c for K^+K^- and 927 MeV/c for $\pi^+\pi^-$). However, the resolution is too poor to distinguish between kaons, pions and background.

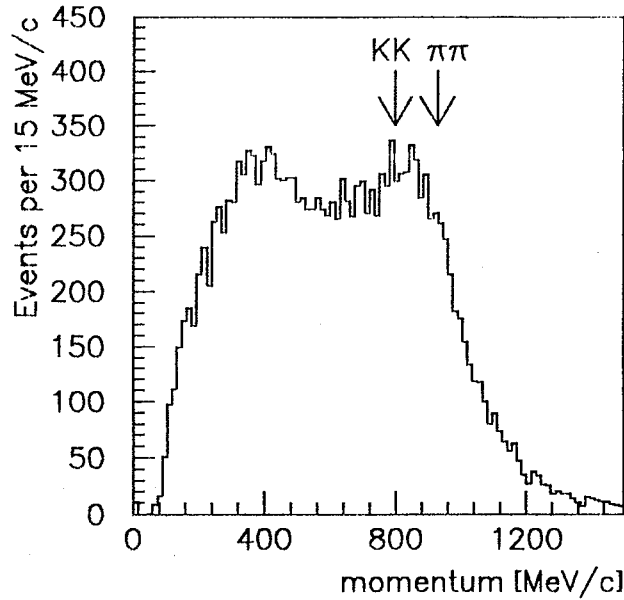


Figure 22: Momentum distribution of single tracks for back to back candidates. The two peaks at 797 MeV/c and 927 MeV/c are drowned in background events. The procedure described in the text shows the extraction of these two signals leading to figure 23 and finally to figure 25.

The desired K^+K^- and $\pi^+\pi^-$ events can further be selected by noting, that the tracks of true back to back events lie on a circle in the transversal plane. Thus they can be fitted as one track. This improves the resolution of the fit by more than a factor of four, what can be explained as follows:

The resolution of a fit to a circle in a magnetic field is given by [63]

$$(\delta k)^2 = (\delta k_{res})^2 + (\delta k_{ms})^2 \quad (4.17)$$

where:

δk is the curvature error,

δk_{res} is the curvature error due to finite measurement,

δk_{ms} is the curvature error due to multiple scattering, which is given by the detector.

δk_{res} can be approximated in a uniform medium for $N > 10$ by

$$\delta k_{res} = \frac{\epsilon}{L^2} \sqrt{\frac{720}{N+5}} \quad (4.18)$$

where:

N is the number of uniformly spaced points along the track,

L is the projected length of the track,

ϵ is the measurement error for each point perpendicular to the plane.

Thus by fitting the two tracks as one track the length and the number of points are doubled and the resolution is improved by more than a factor of four. We call this fit the merged fit.

Two individual tracks can be merged into a single one in the pattern recognition routines, by adding the two TRA banks and inverting the first track. Then the new merged track starts at DC6, proceeds to PC1 and then back to DC6 again. If the two tracks are not exactly back to back, the merged fit either fails or gives a usually much lower momentum than 797 MeV/c for K^+K^- , respectively 927 MeV/c for $\pi^+\pi^-$. Figure 23 shows the momentum distribution for the merged fit. The kaon and pion peaks are clearly visible.

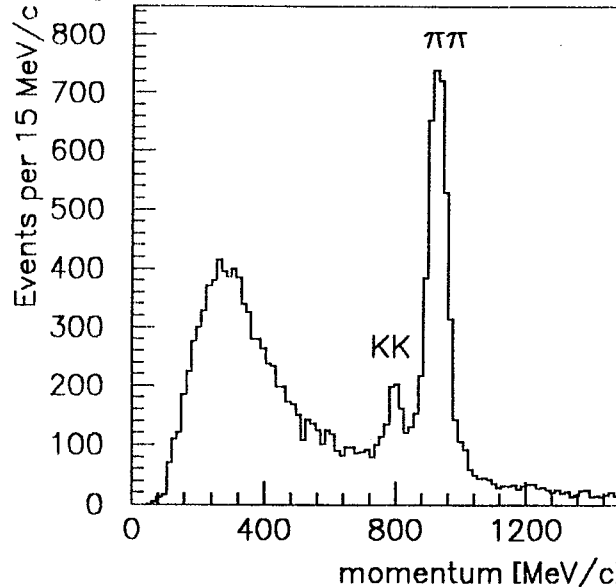


Figure 23: Momentum distribution, if the two tracks are fitted as one track ("merged fit"). This improves the resolution by a factor of more than four. The K^+K^- and $\pi^+\pi^-$ peak appear at the expected position of $p_{K^+K^-} = 797$ MeV/c and $p_{\pi^+\pi^-} = 927$ MeV/c. The broad enhancement at low momenta are background events.

The back to back events were then further selected by the following requirements:

- 2 requirements were made in order to have a cleaner data sample, namely:
 1. $NLFM > 3$:
where $NLFM$ is the number of points used by the straight line fit in the longitudinal direction.
 2. at least one hit in DC6 cathode strip:
The resolution of the z measurement was better for the DC6 cathode strip than for the streamer tubes. On the other hand the efficiency of DC6 was relatively low. So only one hit in DC6 cathode strip was required, in order to have one good z measurement for the merged fit.
- It was required, that the fit for the two individual tracks was successfully done:

$$500 < p_i < 1500 \text{ MeV}/c \quad (4.19)$$

where p_i is the momentum of the two single tracks ($i=1,2$)

- Cuts in the xy plane and in the longitudinal direction, in order to reject the background, i.e.

$$\varphi_{xy} > \varphi_0 \quad \text{and} \quad |ct_1 + ct_2| < ct_0 \quad (4.20)$$

where :

- φ_{xy} is the angle between the two individual momenta in the transversal plane, extrapolated to the point of closest approach to the z -axis,
- ct_i is the cotangents of the angle between p_z and $p_T = \sqrt{p_x^2 + p_y^2}$.
- φ_0 ct_0 are cut parameters, which were varied to obtain tighter or looser back to back conditions.

The distribution of φ_{xy} and $|ct_1 + ct_2|$ can be seen in figure 24. Figure 25 shows the momentum distribution of the merged track for $\varphi_0 = 178.0$ and $ct_0 = 0.20$. The K^+K^- and $\pi^+\pi^-$ peaks are well separated, and only a small background remains.

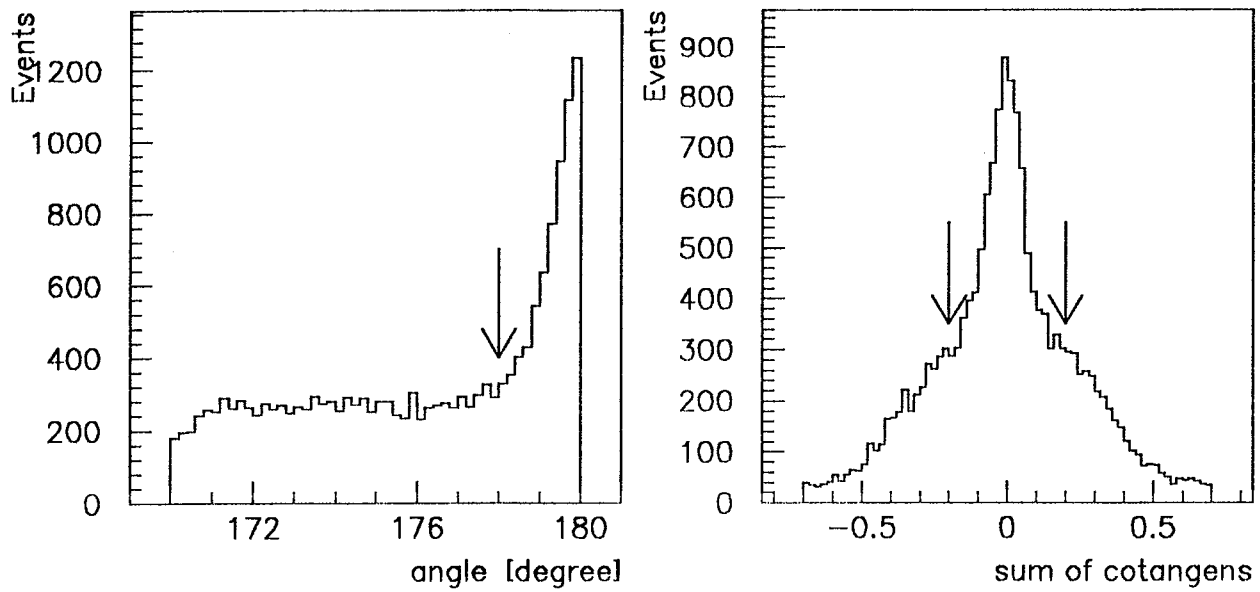


Figure 24: *Back to back cut (marked by the arrows):*
 Left: *Distribution of the angle between the momenta of the individual tracks (extrapolated to the point of closest approach to the z-axis) in the xy-plane: φ_{xy}*
 Right: *Distribution of the sum of the cotangents of the angle between transversal momenta p_T and p_z .*

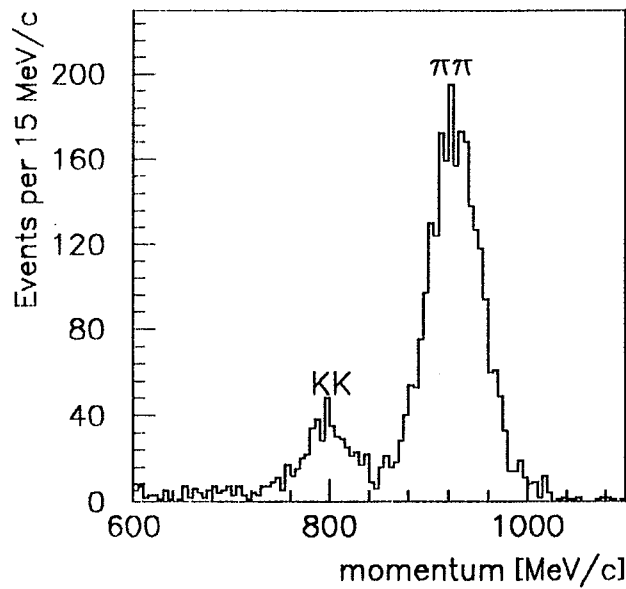


Figure 25: *Momentum distribution of merged tracks for the cut $\varphi_{xy} = 178.0$ and $ct_0 = 0.20$.*

The above mentioned event selection criteria are purely geometrical. Several other techniques were considered for the separation of the kaons and pions. We list them below and mention, why they were not used.

- Cerenkov ADC: Back to back kaons have a momentum of 797 MeV/c. Therefore they are just above the Cerenkov threshold of $\beta = v/c = 0.84$ and are expected to produce light as well. Thus using the Cerenkov ADC value as a cut criteria would introduce a bias between kaons and pions and was therefore not used.
- Time of flight (TOF): For the TOF measurement the start signal is provided by the beam counter (section 2.4), the stop signal by S1. An absolute TOF measurement is not possible due to the fact, that the annihilation does not coincide with the beam counter signal. Only TOF differences between different particles coming from the target can be given. Therefore the TOF does not provide a mean to separate K^+K^- and $\pi^+\pi^-$ events. But it could be used for the separation of the back to back and the background events. The analysis showed that the TOF information did not lead to a better separation than the geometrical criteria, because of the high momenta of the particles.
- Energy loss in S1: CPLEAR also uses the S1 ADC value for the identification of particles. Figure 26 shows the energy loss dE/dx as a function of the momentum. It can be seen, that particle identification is possible only up to 500 MeV/c.

4.2.4 Determination of the Uncorrected Branching Ratio R_{raw}

The distribution of the merged momentum (figure 25) can now be fitted to a function

$$f(p) = P_{BG}(p) + P_K(p) + P_\pi(p) \quad (4.21)$$

where:

- $P_{BG}(p)$ describes the background,
- $P_K(p)$ describes the K^+K^- peak,
- $P_\pi(p)$ describes the $\pi^+\pi^-$ peak.

Different functions were used for $P_{BG}(p)$, $P_K(p)$, $P_\pi(p)$. The best parametrization was found to be a linear function for the background ²⁷ and a gaussian for the K^+K^-

²⁷For the justification of the linear background see the section on Monte Carlo 4.3.2.

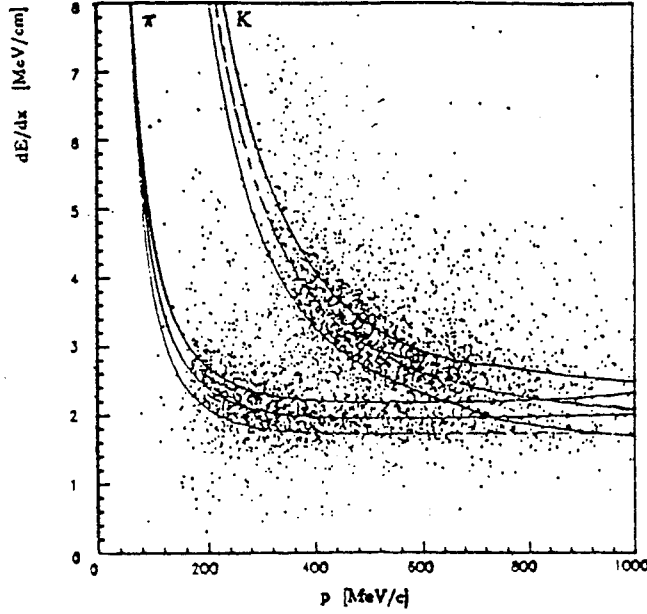


Figure 26: Energy loss in S1 dE/dx as function of particle momentum. The Bethe-Bloch curves for π and K are shown with $\pm 1\sigma$ bands.

and $\pi^+\pi^-$ peak:

$$f(p) = X - Y \cdot p + \frac{A_K}{\sqrt{2\pi}\sigma_K} e^{-\frac{1}{2}\left(\frac{p - \langle p \rangle_K}{\sigma_K}\right)^2} + \frac{A_\pi}{\sqrt{2\pi}\sigma_\pi} e^{-\frac{1}{2}\left(\frac{p - \langle p \rangle_\pi}{\sigma_\pi}\right)^2} \quad (4.22)$$

$X, Y, A_K, \sigma_K, \langle p \rangle_K, A_\pi, \sigma_\pi, \langle p \rangle_\pi$ were obtained by minimizing the χ^2 ²⁸.

At this stage the relative uncorrected branching ratio $R_{raw} = \frac{BR(p\bar{p} \rightarrow K^+ K^-)}{BR(p\bar{p} \rightarrow \pi^+ \pi^-)}$ can be calculated in two complementary ways:

- $R = \frac{A_K}{A_\pi}$ where $A_i = \int_{-\infty}^{+\infty} P_i(p) dp$ ($i = K, \pi$)
- By directly counting the events:

The momentum-axis was divided into 4 intervals (figure 27). The number of events in the section X1-X2 and X2-X3 was counted: N1 and N2. The background contribution was calculated using the background parametrization obtained from the fit, as described above: BGKAON and BGPION.

A fraction of the $K^+ K^-$ ($\pi^+ \pi^-$) events lie outside the interval X1-X2 (X2-X3). In order to take them into account, correction terms C1, C2, C3 and C4 were calculated using the gaussian parametrization of the peaks.

The number $K^+ K^-$ and $\pi^+ \pi^-$ events are obtained from N1 and N2: K_{corr} and P_{corr} .

R is then given by

$$R_{raw} = \frac{K_{corr}}{P_{corr}}. \quad (4.23)$$

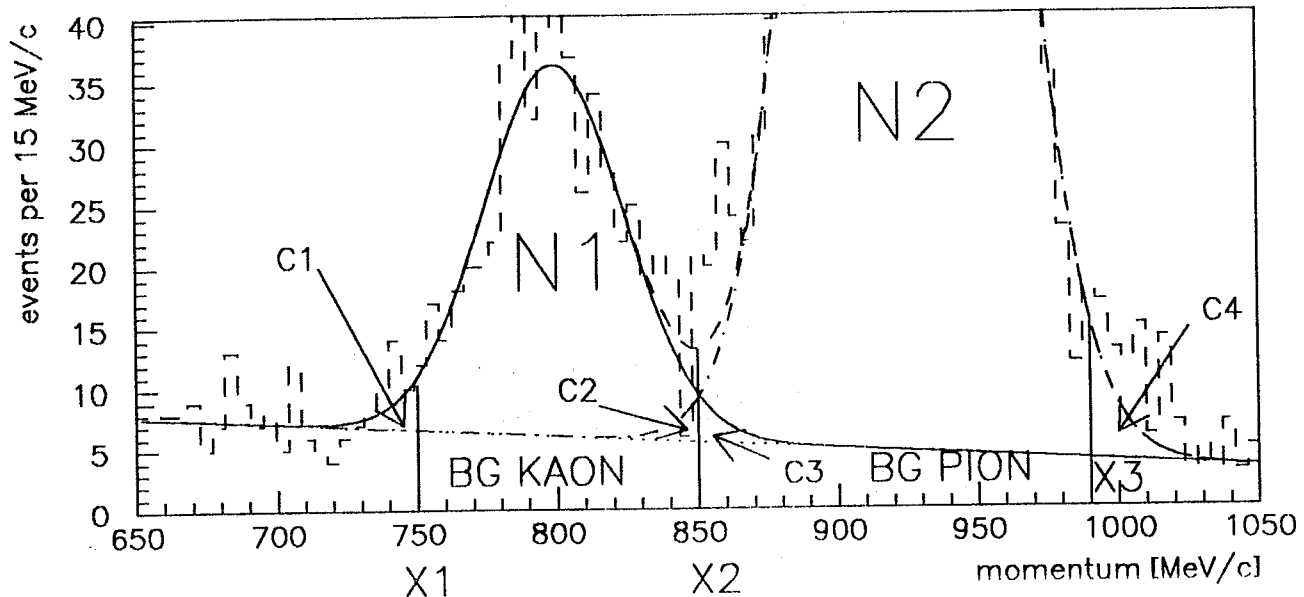


Figure 27: Illustration of the count method for obtaining R_{raw} : Dotted line: data, straight line: fit.

The momentum axis was divided into the two intervals $X1$ - $X2$ and $X2$ - $X3$. $N1$ and $N2$ are the number of events in $X1$ - $X2$ and $X2$ - $X3$. The background contribution to $N1$ and $N2$ (BG_{KAON} and BG_{PION}) and correction terms $C1$, $C2$, $C3$ and $C4$ were obtained from the fit. Note, that the scale of the background was enlarged in this figure in order to clarify the method.

Table 5 shows R_{raw} for different cut values φ_0 and ct_0 for both methods with the statistical error. The following values for φ_0 and ct_0 were taken as the final ones:

$$\varphi_0 = 178.0 \quad ct_0 = 0.20 \quad (4.24)$$

Table 6 lists the central values and the width of the two Gauss functions obtained by the fit for φ_0 and ct_0 . Table 7 summarizes the results of the counting method.

²⁸Minuit [45] was used for the fit.

Table 5: Number of K^+K^- and $\pi^+\pi^-$ events and relative branching ratio for different cuts in φ_{xy} and ct_0 for fit and count method. Only the statistical error is given.

$\varphi_{xy} \ ct_0$	Nb K^+K^- (fit)	Nb $\pi^+\pi^-$ (fit)	BR (fit)	Nb K^+K^- (count)	Nb $\pi^+\pi^-$ (count)	BR (count)
177.0 0.25	424 ± 30	2425 ± 53	17.49 ± 1.26	434 ± 27	2460 ± 52	17.65 ± 1.15
177.5 0.25	422 ± 29	2402 ± 51	17.58 ± 1.23	432 ± 26	2492 ± 52	17.72 ± 1.15
177.5 0.20	423 ± 28	2376 ± 51	17.84 ± 1.22	434 ± 26	2413 ± 52	18.00 ± 1.13
178.0 0.25	406 ± 28	2370 ± 52	17.17 ± 1.21	417 ± 26	2398 ± 51	17.40 ± 1.13
178.0 0.20	405 ± 27	2338 ± 51	17.33 ± 1.16	417 ± 25	2377 ± 51	17.55 ± 1.11
178.0 0.15	401 ± 25	2261 ± 48	17.74 ± 1.14	409 ± 24	2300 ± 50	17.76 ± 1.09
178.0 0.10	348 ± 25	2033 ± 47	17.10 ± 1.26	359 ± 23	2076 ± 48	17.32 ± 1.17
178.5 0.15	379 ± 25	2148 ± 48	17.65 ± 1.20	389 ± 23	2188 ± 49	17.75 ± 1.12
178.5 0.10	327 ± 23	1936 ± 46	16.86 ± 1.24	336 ± 22	1977 ± 46	17.02 ± 1.17

Table 6: Central values and width for the K^+K^- and $\pi^+\pi^-$ peak obtained by the fit for the cut parameters $\varphi_{xy} = 178.0$ and $ct_0 = 0.20$. The indicated errors are only statistical. The obtained central values of the fit are in agreement with the expected momenta of 797 MeV/c for K^+K^- and 927 MeV/c for $\pi^+\pi^-$.

$\langle p \rangle_{K^+K^-}$	$\sigma_{K^+K^-}$	$\langle p \rangle_{\pi^+\pi^-}$	$\sigma_{\pi^+\pi^-}$
799.2 ± 1.6	25.19 ± 1.70	926.4 ± 0.6	27.34 ± 0.53

Table 7: Values obtained with the count method for $\varphi_{xy} = 178.0$ and $ct_0 = 0.20$. The indicated errors are only statistical.

	Events counted	Estimated background	Estimated signal	Corrected signal
Interval X1-X2	456	53 ± 10	403 ± 24	417 ± 25
Interval X2-X3	2434	63 ± 11	2371 ± 51	2377 ± 51

We discuss now possible systematic errors.

- A possible bias from the trigger can be excluded, as the minimum bias trigger was used. The efficiency of S1 to detect at least one of the two charged particles can be assumed to be the same for K^+K^- and $\pi^+\pi^-$ events.
- The cuts in φ_{xy} and ct_0 could change the relative branching ratio, if the corresponding distribution is different for K^+K^- and $\pi^+\pi^-$ events. No possible bias could be found.
- Lineshape differences: The $\pi^+\pi^-$ peak was fitted with different functions, for real data as well as for Monte Carlo data ²⁹. No systematic effects were found. The same study could not be applied to the K^+K^- events because of lack of statistics.
- The interval, where the fit was performed, had an influence on the result. This is mainly due to the fact, that the linear background could only be fitted below or above the two peaks in the momentum distribution. In addition the background is not strictly linear, especially under the K^+K^- peak, where statistics is poor. A possible systematic error of 4 % was included to account for those two effects.

Therefore the relative branching ratio is given as

$$R_{raw} = 0.1755 \pm 0.0111_{stat} \pm 0.0070_{sys}. \quad (4.25)$$

The probability of detecting a K^+K^- event is not the same as the one for detecting a $\pi^+\pi^-$ event. Therefore the raw branching ratio must be corrected to take these different acceptances into account. Monte Carlo studies were done to obtain a correction factor for this effect.

²⁹The Monte Carlo results will be discussed in the next chapter.

4.3 Monte Carlo Studies

Monte Carlo studies were done in order to obtain

- the relative acceptance of K^+K^- and $\pi^+\pi^-$ events
- information about the shape of the background and its influence on the determination of R.

As only tracking devices (PCs and DCs) were used for obtaining R, only their Monte Carlo response was brought into agreement with the data.

The following effects were taken into account in the Monte Carlo simulation (see also appendix C):

- Overall inefficiency of PC1.
- Efficiency of PC1 as function of track length in the cell.
- Resolution of PC1.
- Random hits in PC1.
- Inefficiency of the DCs: The efficiency of PC1 and all the DCs were determined from the tracks in the $\pi^+\pi^-$ peak and put into the Monte Carlo.
- DC wire response: The TDC count of the DCs is parametrized in the Monte Carlo by a gaussian distribution and a flat tail. The sigma of the gaussian, width of the tail and probability for having a tail was changed in order to get a better agreement in the residuals ³⁰ of the chambers. Figure 28 shows the residuals of DC3.
- Strip inefficiency.

Figure 29 shows the number of points used in the transversal fit for Monte Carlo and real data, figure 30 the same for the longitudinal fit.

³⁰The residual is defined as the distance of the real and the fitted point of a given chamber.

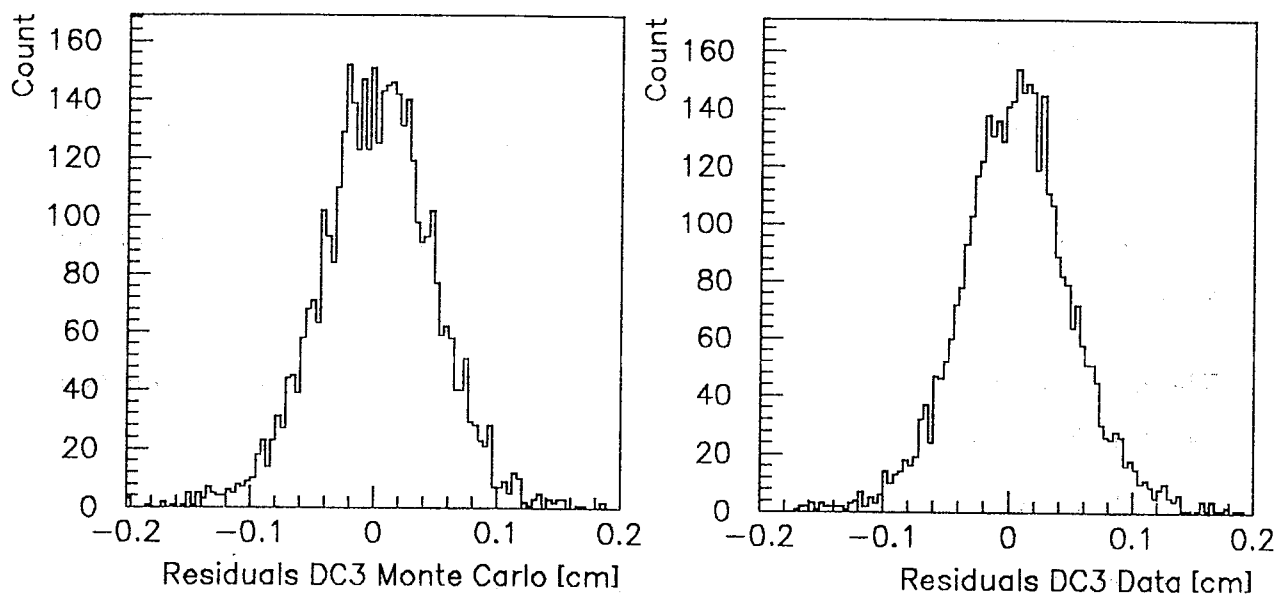


Figure 28: *Residuals (i.e. difference between real hit and fitted value) of DC 3. Left Monte Carlo simulation, right data. The resolution is $380 \mu\text{m}$.*

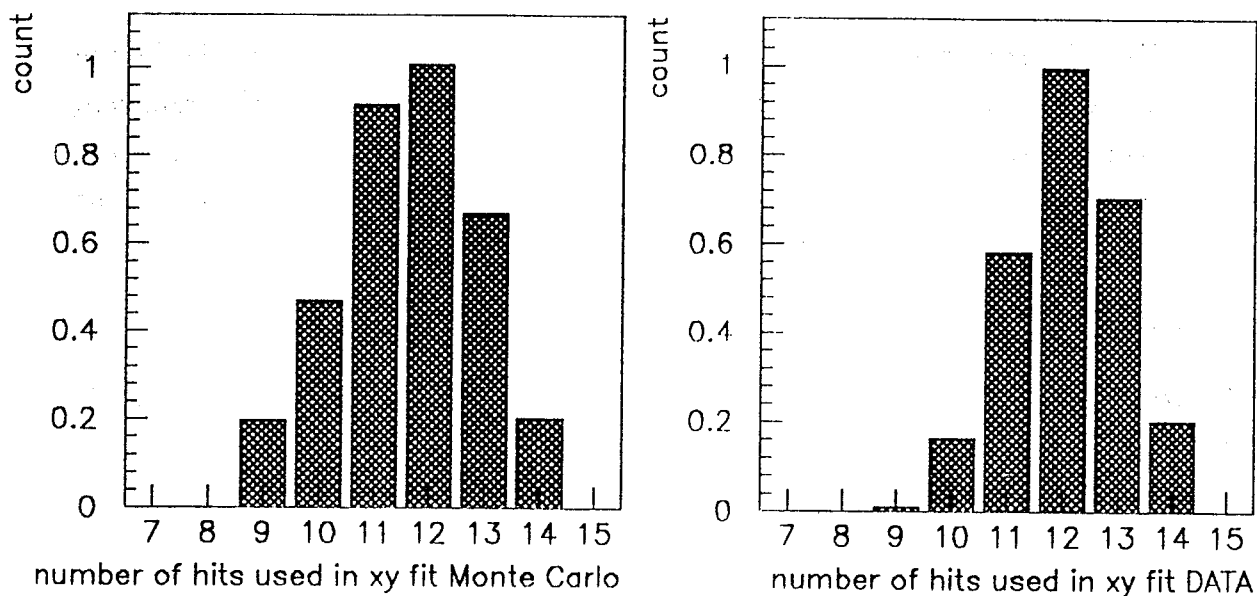


Figure 29: *Number of points used by transversal fit for Monte Carlo (left) and data (right) (Y scale arbitrary).*

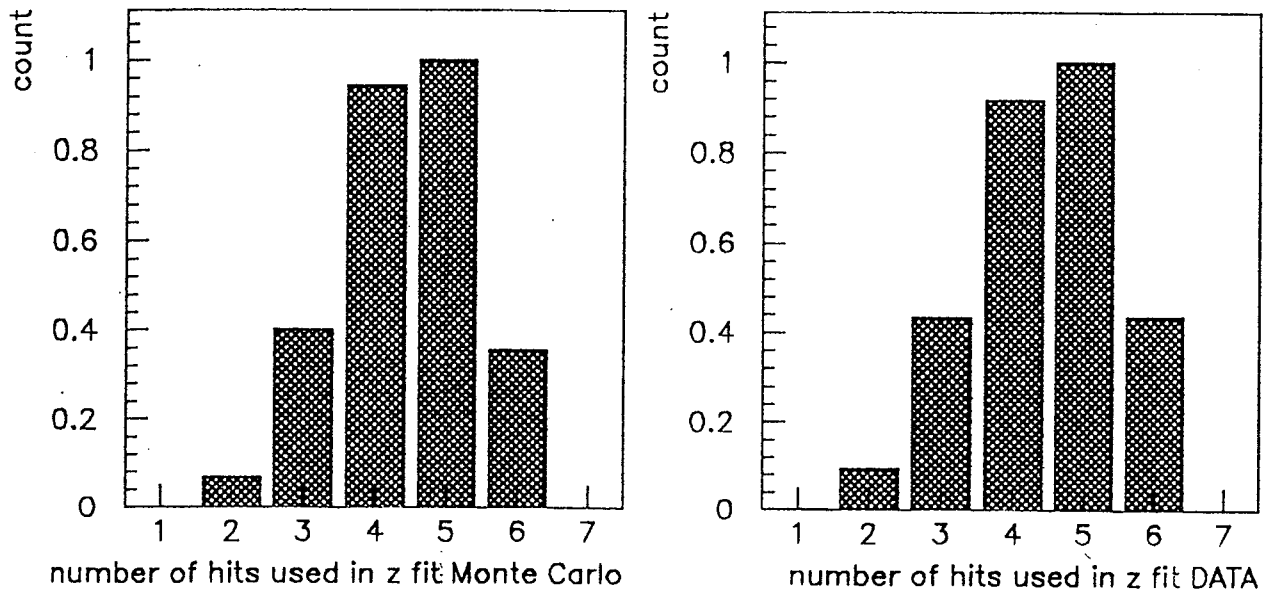


Figure 30: Number of points used by longitudinal fit for Monte Carlo (left) and data (right) (Y scale arbitrary).

4.3.1 The Relative Acceptance between Back to Back Kaons and Pions

The probability of detecting a $p\bar{p} \rightarrow K^+K^-$ event is not the same as the one for $p\bar{p} \rightarrow \pi^+\pi^-$. The main reason is the shorter lifetime of kaons:

$$\tau_K = 1.23 \cdot 10^{-8} \text{sec} \quad \tau_\pi = 2.61 \cdot 10^{-8} \text{sec}.$$

A Monte Carlo study was performed to obtain the relative acceptance between K^+K^- and $\pi^+\pi^-$ events. 20'000 events of each class were produced and tracked through the detector. The relative acceptance κ was determined by comparison of the number of K^+K^- ($\pi^+\pi^-$) events produced with the number of K^+K^- ($\pi^+\pi^-$) events detected as K^+K^- ($\pi^+\pi^-$) events.

The same cuts used for real data, were applied to the Monte Carlo data.

Table 8 gives an overview of:

1. The number of events generated,
2. The number of events, where the pattern found 2 tracks and the fit was successful,
3. The number of events, where the merged fit was successfully done,
4. The number of events, that survived the main back to back cut (see preceding section),

5. The number of events, lying within 3σ after a fit to a gaussian.

Table 8: *Relative acceptance of $p\bar{p} \rightarrow K^+K^-$ and $p\bar{p} \rightarrow \pi^+\pi^-$.*

events generated	pattern/fit 2 tracks	merged done	back to back cut	within 3σ of $K^+K^- / \pi^+\pi^-$ peak
20'000 K^+K^-	15'322	15'146	8'342	8'243
20'000 $\pi^+\pi^-$	15'879	15'781	9'787	9'635

Thus we obtain as relative acceptance

$$\kappa = \frac{acc(K^+K^-)}{acc(\pi^+\pi^-)} = 0.856 \pm 0.015_{stat} \pm 0.011_{sys}. \quad (4.26)$$

The systematic error has two contributions:

- The influence of the different values of the back to back cut paramters φ_{xy} and ct_0 , and how a K (π) is defined as a K (π). K^+K^- ($\pi^+\pi^-$) events, which are too far away from their peak, will be treated as background events by the fit. This contribution to the systematical error was estimated to be 0.005.
- An overall Monte Carlo uncertainty of 1 % was added to take different Monte Carlo versions into account.

The two systematical errors were added quadratically.

4.3.2 The Monte Carlo Background Simulation

The following $p\bar{p}$ annihilation channels were considered in the simulation of the background:

- $p\bar{p} \rightarrow \pi^+\pi^-\pi^0$,
- $p\bar{p} \rightarrow \pi^\pm\rho^\mp \rightarrow \pi^\pm\pi^\mp\pi^0$ (the channel $\pi^0\rho^0$ does not contribute to the background, as the $\pi^+\pi^-$ produced in the ρ^0 decay are not back to back),
- $p\bar{p} \rightarrow \pi^+\pi^-\pi^0\pi^0$.

Other annihilation channels (like $\pi^+\pi^-\pi^0\pi^0\pi^0$, $K^+K^-\pi^0$,...) can be excluded, as the momentum of the two charged tracks is too low, either because of additional neutral pions or because of the heavier mass of the particles involved.

Only events with an opening angle between their momenta in the xy-plane greater than 170 were retained.

Table 9 shows for each of these background channels:

1. The number of events generated,
2. The number of events with $\varphi_{xy} > 170$,
3. The number of events after applying the back to back cut of $\varphi_{xy} > 178.0$ and $|ct_1 + ct_2| < 0.20$ (see page 64),
4. The number of events, lying within $2\sigma_K$ under the kaon peak,
5. The number of events, lying within $2\sigma_\pi$ under the pion peak.

Table 9: Monte Carlo background simulation.

Channel	events generated	$\varphi_{xy} > 170$	back to back cut	background K^+K^-	background $\pi^+\pi^-$
$\pi^+\pi^-\pi^0$	175'177	24'168	1'737	354	282
$\pi^\pm\rho^\mp$	195'116	23'986	1066	198	200
$\pi^+\pi^-\pi^0\pi^0$	313'203	18'423	458	83	54

Figure 31 shows the momentum distribution of the remaining background. It should be noted from table 9, that only a very small fraction of the events survive the back to back cuts.

In order to relate this background simulation to the Monte Carlo back to back sample, they must be scaled according to their relative branching ratio in gaseous H_2 at 15 bar. These values are not known. Table 10 lists the known branching ratios, as measured in liquid H_2 . We will discuss these branching ratios in more detail in the last section.

The obtained background is shown in figure 32 for the three considered background channels, after they have been weighted according to their relative branching ratio in liquid H_2 . The background shape under the K^+K^- and $\pi^+\pi^-$ peaks (i.e. between 700 MeV/c and 1000 MeV/c) is well reproduced by a linear parametrization.

Table 11 lists the background to signal ratio for the K^+K^- and $\pi^+\pi^-$ peak for

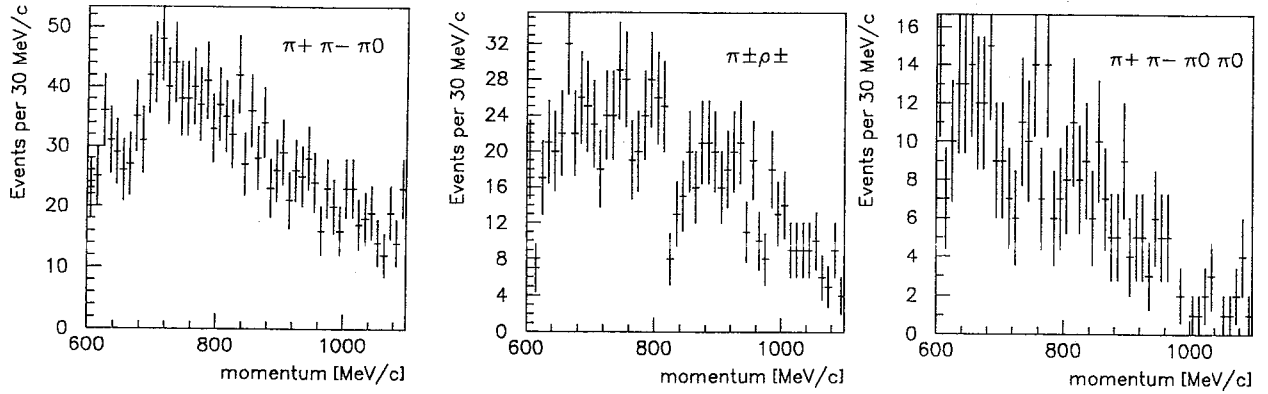


Figure 31: Momentum distribution for the three considered background channels after final back to back cut. The error bars correspond to the statistical error.

Table 10: Branching ratios for back to back background reactions for liquid H_2 .

Channel	BR_{liquid}	ref.
$p\bar{p} \rightarrow \pi^+ \pi^- \pi^0$	$0.84 \pm 0.31 \%$	[46]
$p\bar{p} \rightarrow \pi_0^\pm \rho_0^\mp$	$5.81 \pm 0.32 \%$	[46]
$p\bar{p} \rightarrow \pi^+ \pi^- \pi^0 \pi^0$	$9.3 \pm 0.3 \%$	[47]

real and simulated data, where again the branching ratios of liquid hydrogen have been used (see also table 7).

The comparison shows, that the background contributions are only in rough agreement with the data. There is a better agreement for the $\pi^+ \pi^-$ events than for the $K^+ K^-$ events. The main reason are the unknown background branching ratios.

4.3.3 Fit to a Monte Carlo Sample

Monte Carlo samples, consisting of $K^+ K^-$, $\pi^+ \pi^-$ and background events were generated, in order to test the consistency of the analysis method. Figure 33 shows such a sample in comparison with the real data sample. The background of the sample was chosen such, that the signal to background ratio for $K^+ K^-$ and $\pi^+ \pi^-$ in Monte

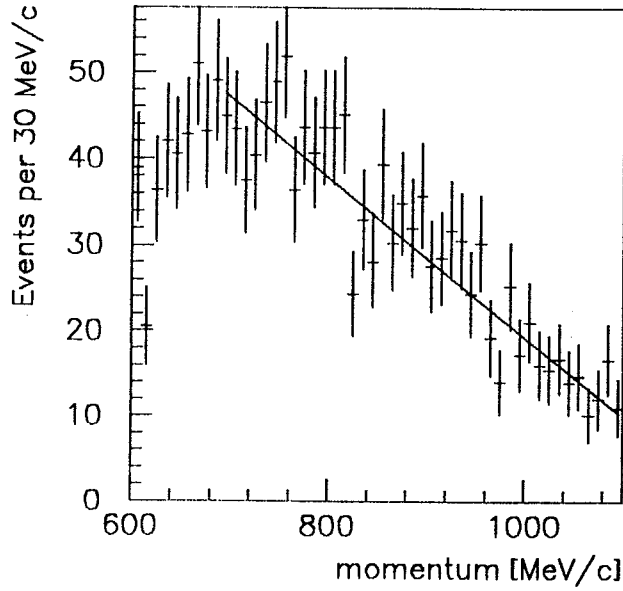


Figure 32: Sum of the three background channels weighted by their relative branching ratio in liquid H_2 .

Table 11: Background to signal ratio λ in percent for Monte Carlo and real data.

Channel	λ [%] data	λ [%] Monte Carlo
K^+K^-	11.6	28.2
$\pi^+\pi^-$	2.5	3.8

Carlo is about the same as in real data. The analysis method for real data was applied to these Monte Carlo samples. The obtained Monte Carlo branching ratio is in agreement with the generated ratio between K^+K^- and $\pi^+\pi^-$ events. Table 12 lists the central value and the sigma of the gaussian parametrization of the K^+K^- and $\pi^+\pi^-$ peak in the fit for data and Monte Carlo, showing the agreement between Monte Carlo and real data.

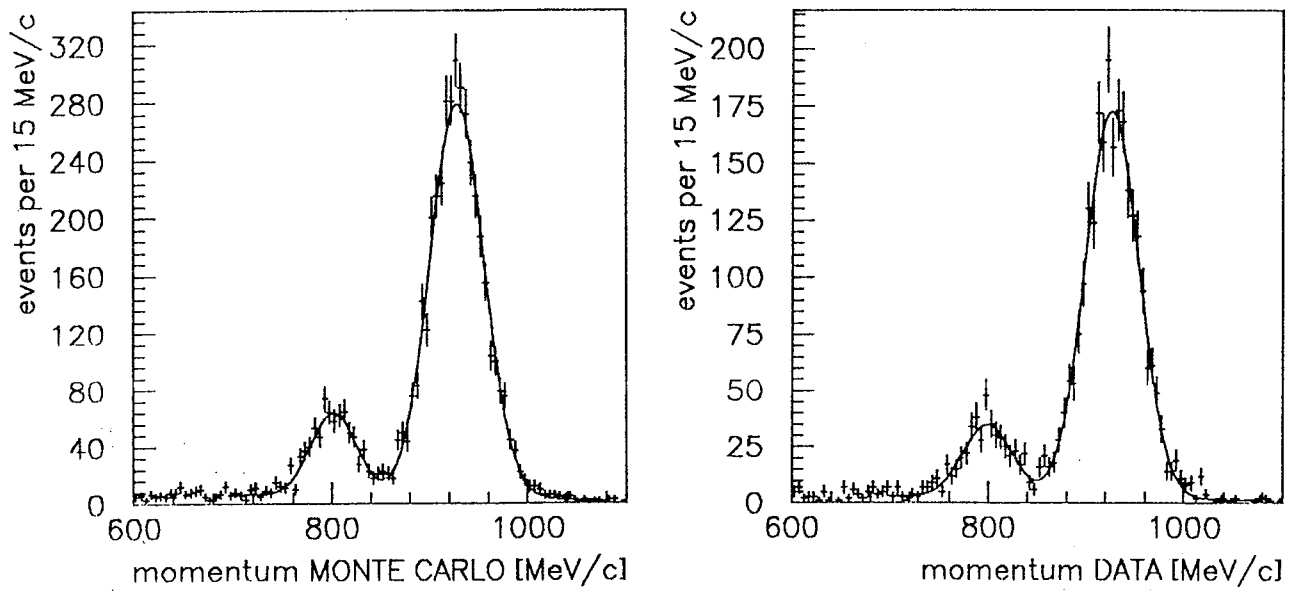


Figure 33: Left: Monte Carlo sample for back to back K^+K^- and $\pi^+\pi^-$ with simulated background and fit, as described in the text. Right: data.

Table 12: Comparison of the central values and sigmas from the fit for K^+K^- and $\pi^+\pi^-$ peak in data and Monte Carlo.

Data type	$\langle p_{K^+K^-} \rangle$	$\sigma_{K^+K^-}$	$\langle p_{\pi^+\pi^-} \rangle$	$\sigma_{\pi^+\pi^-}$
Data	799.2 ± 1.6	25.2 ± 1.7	926.4 ± 0.6	27.3 ± 0.5
MC	801.7 ± 1.2	23.4 ± 1.2	928.3 ± 0.5	27.7 ± 0.4

4.4 Discussion

We can now combine the uncorrected relative branching ratio from the fit R_{raw} with the relative acceptance κ from Monte Carlo to get the relative branching ratio R :

$$\begin{aligned} R_{raw} &= 0.175 \pm 0.011_{stat} \pm 0.007_{sys} \\ \kappa &= 0.856 \pm 0.015_{stat} \pm 0.011_{sys} \\ R &= \kappa \cdot R_{raw} = 0.205 \pm 0.014_{stat} \pm 0.009_{sys}. \end{aligned}$$

Table 13 summarises the values for R , measured so far.

Table 13: *Relative branching ratio $p\bar{p} \rightarrow K^+K^- / p\bar{p} \rightarrow \pi^+\pi^-$*

Target	R	ref.
Liquid H_2	0.28 ± 0.03	[30]
Liquid H_2	0.33 ± 0.02	[48]
Liquid H_2	0.32 ± 0.02	[49]
Liquid H_2	0.337 ± 0.007	[50]
Gaseous H_2 NTP	0.161 ± 0.09	[18]
Gaseous H_2 NTP atomic 2p	0.060 ± 0.012	[18]
Gaseous H_2 15 bar	0.205 ± 0.023	this work

Table 14 shows the absolute branching ratio for $p\bar{p} \rightarrow K^+K^-$ and $p\bar{p} \rightarrow \pi^+\pi^-$ from atomic s and p level, measured by the ASTERIX collaboration [18]. The K^+K^- final state is suppressed by a factor of four in the p wave initial state compared to the s wave initial state. On the other hand the $\pi^+\pi^-$ final state is enhanced in the p wave annihilation compared with the s wave annihilation by about 50 %. The suppression of the K^+K^- from initial p level can be explained by the 3P_0 and 3S_1 model as well as other models [35,51,52].

At this stage we are able to determine the p wave contribution of the annihilation by combining our result of R with the absolute branching ratios (table 14). We assume, that $p\bar{p}$ annihilation can be neglected from atomic d level [27], and annihilations therefore only occur from s and p levels.

The frequency of a final state B_f is then given by

$$B_f = B_0(1 - f_p) + B_1 f_p \quad (4.27)$$

where:

Table 14: *Branching ratios from atomic s and p level into K^+K^- and $\pi^+\pi^-$ [18].*

Atomic level	$BR_{K^+K^-}$ 10^{-3}	$BR_{\pi^+\pi^-}$ 10^{-3}
s-level	1.08 ± 0.005	3.19 ± 0.20
p-level	0.287 ± 0.051	4.81 ± 0.49

B_f is the frequency of the final state f,

B_0 is the branching ratio from an atomic s level into the final state f,

B_1 is the branching ratio from an atomic p level into the final state f,

f_p is the fraction of annihilation from an atomic p level.

It should also be stressed, that f_p contains the annihilations from all the atomic p levels, not only the one from the 2p level.

Thus we obtain for f_p :

$$f_p = \frac{B_0(K^+K^-) - RB_0(\pi^+\pi^-)}{(B_1(\pi^+\pi^-) - B_0(\pi^+\pi^-)) - R(B_1(K^+K^-) - B_0(K^+K^-))} \quad (4.28)$$

$$f_p = 0.380 \pm 0.039_{stat} \pm 0.025_{sys} \pm 0.072_{ext}. \quad (4.29)$$

The statistical and systematical error are due to our measurement of R. The third error, which we call the external error, is due to the errors of B_0 and B_1 . It can be seen, that this way of determining f_p is limited by this external error.

Our result of f_p can be compared with cascade calculations. Figure 34 shows the fraction of p wave annihilation, as obtained by Reifenroether and Klempt [53]. The measured values for liquid and gaseous H_2 at NTP are marked, as well as our measurement at 15 bar. It can be seen, that the overall trend is well reproduced. However, all three experimental values are slightly higher than predicted by the calculation.

Now that we know the fraction of p wave annihilation at 15 bar, we are able to repeat the comparison of background to signal ratio between Monte Carlo and real

data (table 11).

Combining the measured branching ratio of $p\bar{p} \rightarrow \pi^+\pi^-\pi^0$ from atomic s and p level [54,55] with our measurement of $f_p = 38.0\%$, we obtain the branching ratio $p\bar{p} \rightarrow \pi^+\pi^-\pi^0$ at 15 bar.

No such data exists for the background channel $p\bar{p} \rightarrow \pi^+\pi^-\pi^0\pi^0$ ³¹. Therefore we use again the branching ratios in liquid H_2 .

The results are shown in table 15. Comparison with the previously obtained values (table 11) shows no significant improvement in the signal to background ratio for the K^+K^- peak.

However, this is rather a consequence of the unknown branching ratios of the background channels, than a sign of possible inconsistencies in our Monte Carlo simulation.

Table 15: Comparison of K^+K^- and $\pi^+\pi^-$ background to signal ratio in percent for data and Monte Carlo. The branching ratio for liquid H_2 was used for the channel $p\bar{p} \rightarrow \pi^+\pi^-\pi^0\pi^0$. The branching ratio for $p\bar{p} \rightarrow \pi^+\pi^-\pi^0$ (with or without ρ production) was extrapolated to the target pressure of 15 bar.

Channel	λ [%] data	λ [%] Monte Carlo
K^+K^-	11.6	25.8
$\pi^+\pi^-$	2.5	3.6

³¹First results are expected from CRYSTAL BARREL soon.

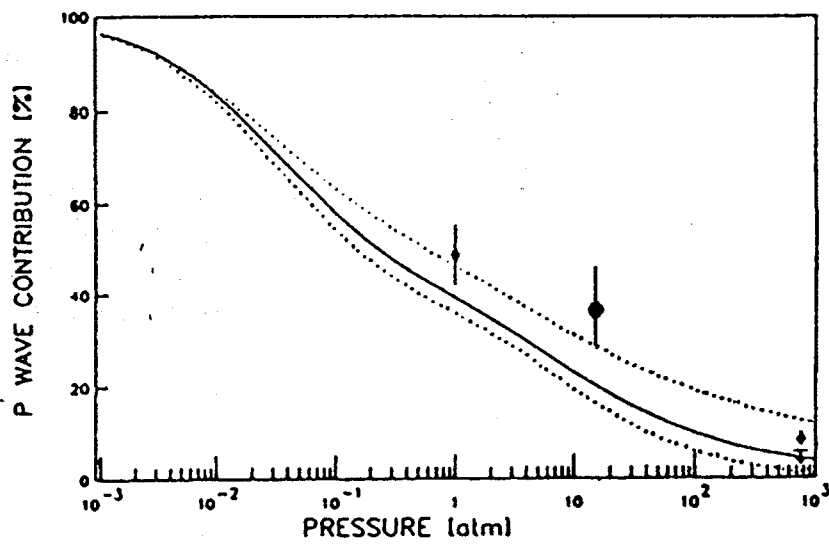


Figure 34: Fraction of p wave annihilation as obtained by Reifenroether and Klempt [53]. The values for liquid and gaseous H_2 are entered, our measurement at 15 atm is also marked.

The dotted lines correspond to a change of different parameters in the calculations (the most important one is a change of the Auger rate by a factor of 2 [upper dotted curve] and 1/2 [lower dotted curve]).

5 Conclusion

The relative branching ratio of K^+K^- and $\pi^+\pi^-$ in $p\bar{p}$ annihilation in gaseous hydrogen at a pressure of 15 bar has been measured by the CPLEAR collaboration with data taken in December 1989 as

$$R = \frac{BR(p\bar{p} \rightarrow K^+K^-)}{BR(p\bar{p} \rightarrow \pi^+\pi^-)} = 0.205 \pm 0.014_{stat} \pm 0.009_{sys}.$$

This value includes a correction factor for the relative acceptance of K^+K^- and $\pi^+\pi^-$ events, obtained by Monte Carlo. The main reason for the different acceptance for these two channels is the shorter lifetime of the kaon.

The background contribution was studied by a Monte Carlo simulation. It was found, that the shape of the background is well reproduced by a linear fit under the K^+K^- and $\pi^+\pi^-$ peak. This was used in the determination of R .

Previous experiments measured R to be 0.161 ± 0.012 at NTP [18] and 0.337 ± 0.007 [50] in liquid hydrogen. Thus our value reflects well the raise of R with increasing pressure. This is due to the fact, that at high target pressure annihilation occurs mainly from atomic s states, where K^+K^- production is enhanced compared to p wave annihilation.

Combining our result of R with the absolute branching ratios for $p\bar{p}$ annihilation into K^+K^- and $\pi^+\pi^-$ from atomic s and p states [18], allows the determination of the fraction of p wave annihilation f_p in gaseous hydrogen at a pressure of 15 bar. The obtained value

$$f_p = 0.380 \pm 0.039_{stat} \pm 0.025_{sys} \pm 0.072_{ext}$$

is consistent with cascade calculations [53]. The statistical and the systematic error are due to the errors of our measurement of the relative branching ratio. The third error, which we call external error, is due to the errors of the absolute branching ratio of $p\bar{p}$ annihilation into K^+K^- and $\pi^+\pi^-$, as obtained by [18]. It is seen, that this external error limits the determination of f_p .

The CPLEAR detector will be able in the future to detect photons from π^0 decays. This opens up the possibility to improve the back to back selection by detecting the additional photons in the various background channels.

A Appendix

Overview of CP Violation

This appendix is organized as follows:

After the introduction the phenomenological description of the decay of the neutral kaon system is given. We explain the relation between $|K^0\rangle$, $|\bar{K}^0\rangle$ and $|K_S^0\rangle$, $|K_L^0\rangle$, leading to the interference phenomena, that can be observed in the neutral kaon system. We then treat the decay into two pions and more briefly other decay modes.

Finally we give a summary of the current experimental status of CP violation.

A.1 Introduction

Kaons are the lightest particles with strangeness. Within the framework of the static quark model of hadrons they belong to the octet of pseudoscalar mesons 0^- . They are grouped in terms of isospin into two doublets:

	$S = +1$	$S = -1$
$I_3 = +\frac{1}{2}$	K^+	\bar{K}^0
$I_3 = -\frac{1}{2}$	K^0	K^-

K^0 and \bar{K}^0 are eigenstates of the strangeness operator. But they should not be considered to be particles, as they are not eigenstates of the Hamiltonian H , which includes weak interactions, that do not conserve strangeness. So they have to be regarded as a particle mixture and the neutral K meson should be treated as a two state system with $|K^0\rangle$ and $|\bar{K}^0\rangle$ as one possible basis:

$$|\Psi\rangle = a|K^0\rangle + b|\bar{K}^0\rangle = \begin{pmatrix} a \\ b \end{pmatrix}. \quad (\text{A.1})$$

The eigenvectors of the Hamiltonian H , which we can associate with the physical particles, are named $|K_S^0\rangle$ and $|K_L^0\rangle$ and can be written in the $|K^0\rangle$ $|\bar{K}^0\rangle$ basis as

$$|K_S^0\rangle = \frac{1}{\sqrt{p^2 + q^2}} \{p|K^0\rangle + q|\bar{K}^0\rangle\}$$

$$|K_L^0\rangle = \frac{1}{\sqrt{r^2 + s^2}} \{r |K^0\rangle + s |\bar{K}^0\rangle\}. \quad (\text{A.2})$$

Two distinct decay modes of the neutral kaon system are observed (we neglect the semileptonic decay for the moment), the decay into $|\pi\pi\rangle$ and $|\pi\pi\pi\rangle$. Both are eigenstates of the CP operator.

$$\begin{aligned} CP |\pi^0\pi^0\rangle &= + |\pi^0\pi^0\rangle \\ CP |\pi^+\pi^-\rangle &= + |\pi^+\pi^-\rangle \\ CP |\pi^0\pi^0\pi^0\rangle &= - |\pi^0\pi^0\pi^0\rangle \\ CP |\pi^+\pi^-\pi^0\rangle &= (-1)^l |\pi^+\pi^-\pi^0\rangle \end{aligned}$$

where l in the $|\pi^+\pi^-\pi^0\rangle$ case is the angular momentum between the two charged pions and states with $l > 0$ are suppressed by the angular momentum barrier.

CP invariance requires, that K_L^0 and K_S^0 , the eigenstates of H , are also eigenstates of the CP operator and decay as follows:

$$\begin{aligned} |K_S^0\rangle &\rightarrow |\pi\pi\rangle \\ |K_L^0\rangle &\rightarrow |\pi\pi\pi\rangle. \end{aligned}$$

Thus the difference in lifetime between K_S^0 and K_L^0 is due to the smaller phase space available for the three pion final state.

In 1964 Christenson, Cronin, Fitch and Turlay [56] discovered, that K_L^0 decays with a very small branching ratio ($2 \cdot 10^{-3}$) into two pions. One of the following conclusions can be drawn from this fact:

1. $|K_L^0\rangle$ is not an eigenstate of the CP operator,
2. CP is violated in the transition of a CP eigenstate into another CP eigenstate with different eigenvalue.

In addition, it is of course also possible, that both conclusions are correct.

Ever since its discovery, CP violation has played a special role in particle physics. Whereas parity violation has been embedded into the theory of weak interactions and CPT invariance is a direct consequence of the basic principles of field theory ³², CP violation is an isolated phenomenon, whose origin is still a mystery. So far it has only been observed in the decay of the neutral kaon system.

³²Any local Lorentzinvariant field theory obeying spin statistic rules for fermions and bosons implies CPT invariance [57,58].

A.2 Phenomenological Description

We define

H_γ	as the Hamiltonian of the electromagnetic interaction
H_{st}	as the Hamiltonian of the strong interaction
H_{wk}	as the Hamiltonian of the weak interaction
H	$= H_{st} + H_\gamma + H_{wk}$
S_{op}	as the strangeness operator
$ K^0\rangle$	as the eigenstate of $H_{st} + H_\gamma$ with strangeness $S = +1$
$ \overline{K^0}\rangle$	$= CPT K^0\rangle$
m_{K^0}	$= \langle K^0 H_{st} + H_\gamma K^0 \rangle$
$m_{\overline{K^0}}$	$= \langle \overline{K^0} H_{st} + H_\gamma \overline{K^0} \rangle$
$\Re R$	as the real part of the complex number R
$\Im R$	as the imaginary part of the complex number R .

Note: The relative phase between $|K^0\rangle$ and $|\overline{K^0}\rangle$ is not observable and can be arbitrarily chosen, because $H_{st} + H_\gamma$ is invariant under the unitary transformation $U = e^{iS_{op}\theta}$.

The Hamiltonian is written in the $|K^0\rangle, |\overline{K^0}\rangle$ basis as

$$H = H_{st} + H_\gamma + H_{wk} = M - i\Gamma \quad (A.3)$$

$$H = \begin{pmatrix} M_{11} & M_{12} \\ M_{21} & M_{22} \end{pmatrix} - i \begin{pmatrix} \Gamma_{11} & \Gamma_{12} \\ \Gamma_{21} & \Gamma_{22} \end{pmatrix} \quad (A.4)$$

where M, Γ are hermitian matrices, and Γ is in addition positive (i.e. $\Gamma_{11} \geq 0$, $\Gamma_{22} \geq 0, \det \Gamma \geq 0$). Note, that H as given by A.3 is not hermitian³³, as the particles decay.

Strangeness conservation of $H_{st} + H_\gamma$ means

$$\langle \overline{K^0} | H_{st} + H_\gamma | K^0 \rangle = 0. \quad (A.5)$$

The weak interaction does not conserve strangeness, leading to the decay of the neutral kaon system.

³³More precisely: H as defined in eq A.3 is the projection of the Hamiltonian into the subspace of the neutral Kaons. This projection is not hermitian.

The Hamiltonian H can be expanded using perturbation theory to

$$M_{11} = m_{K^0} + \langle K^0 | H_{wk} | K^0 \rangle + \sum_n \frac{\langle K^0 | H_{wk} | n \rangle \langle n | H_{wk} | K^0 \rangle}{m_{K^0} - E_n} + \dots \quad (\text{A.6})$$

$$M_{22} = m_{\overline{K^0}} + \langle \overline{K^0} | H_{wk} | \overline{K^0} \rangle + \sum_n \frac{\langle \overline{K^0} | H_{wk} | n \rangle \langle n | H_{wk} | \overline{K^0} \rangle}{m_{\overline{K^0}} - E_n} + \dots \quad (\text{A.7})$$

$$M_{21} = \langle \overline{K^0} | H_{wk} | K^0 \rangle + \sum_n \frac{\langle \overline{K^0} | H_{wk} | n \rangle \langle n | H_{wk} | K^0 \rangle}{m_{K^0} - E_n} + \dots \quad (\text{A.8})$$

where:

\sum_n is a sum over all possible states except K^0 , $\overline{K^0}$ respectively.

It follows from the $|\Delta S| = 1$ rule, that

$$\langle \overline{K^0} | H_{wk} | K^0 \rangle = 0. \quad (\text{A.9})$$

The decrease of the norm of the kaon wavefunction due to the decay has to be equal to the total transition rate into any final state. This leads to the following conditions on the elements of Γ :

$$\frac{d}{dt} \langle \psi | \psi \rangle = -2\pi \sum_f \rho(f) |\langle f | H_{wk} | \psi \rangle|^2 \quad (\text{A.10})$$

$$\frac{d}{dt} \langle \psi | \psi \rangle = \langle \frac{d}{dt} \psi | \psi \rangle + \langle \psi | \frac{d}{dt} \psi \rangle = -2 \langle \psi | \Gamma | \psi \rangle \quad (\text{A.11})$$

$$\Gamma_{11} = \langle K^0 | \Gamma | K^0 \rangle = \pi \sum_n \rho(f) |\langle f | H_{wk} | K^0 \rangle|^2 \quad (\text{A.12})$$

$$\Gamma_{22} = \langle \overline{K^0} | \Gamma | \overline{K^0} \rangle = \pi \sum_n \rho(f) |\langle f | H_{wk} | \overline{K^0} \rangle|^2 \quad (\text{A.13})$$

$$\Gamma_{21} = \langle \overline{K^0} | \Gamma | K^0 \rangle \quad (\text{A.14})$$

$$= \pi \sum_n \rho(f) \langle \overline{K^0} | H_{wk} | f \rangle \langle f | H_{wk} | K^0 \rangle \quad (\text{A.15})$$

$$\Gamma_{12} = \Gamma_{21}^* \quad (\text{A.16})$$

where:

$|\psi\rangle$ is an arbitrary state of the neutral kaon meson,

$\rho(f)$ is the density of the final state f,

\sum_f is the sum over all possible final states.

We now calculate the two eigenvectors of iH , $|K_S^0\rangle$ and $|K_L^0\rangle$, in the $|K^0\rangle$ $|\bar{K}^0\rangle$ basis:

$$(\Gamma + iM) |K_S^0\rangle = \lambda_s |K_S^0\rangle \quad \lambda_s = im_s + \frac{1}{2}\gamma_s \quad (\text{A.17})$$

$$(\Gamma + iM) |K_L^0\rangle = \lambda_l |K_L^0\rangle \quad \lambda_l = im_l + \frac{1}{2}\gamma_l \quad (\text{A.18})$$

$$|K_S^0\rangle = \frac{1}{\sqrt{2(1+|\epsilon_1|^2)}} \left((1+\epsilon_1) |K^0\rangle + (1-\epsilon_1) |\bar{K}^0\rangle \right) \quad (\text{A.19})$$

$$|K_L^0\rangle = \frac{1}{\sqrt{2(1+|\epsilon_2|^2)}} \left((1+\epsilon_2) |K^0\rangle - (1-\epsilon_2) |\bar{K}^0\rangle \right) \quad (\text{A.20})$$

where ϵ_1, ϵ_2 are complex numbers.

Defining $\hat{\epsilon}$ and δ as

$$\hat{\epsilon} = \frac{\epsilon_1 + \epsilon_2}{2} \quad \delta = \frac{\epsilon_1 - \epsilon_2}{2} \quad (\text{A.21})$$

leads to

$$|K_S^0\rangle = \frac{1}{N_s(\hat{\epsilon}, \delta)} \left((1+\hat{\epsilon}+\delta) |K^0\rangle + (1-\hat{\epsilon}-\delta) |\bar{K}^0\rangle \right) \quad (\text{A.22})$$

$$|K_L^0\rangle = \frac{1}{N_l(\hat{\epsilon}, \delta)} \left((1+\hat{\epsilon}-\delta) |K^0\rangle + (1-\hat{\epsilon}+\delta) |\bar{K}^0\rangle \right)$$

where N_s and N_l is the norm of $|K_S^0\rangle$ and $|K_L^0\rangle$.

$|K_S^0\rangle$ and $|K_L^0\rangle$ are no longer orthogonal, if $\epsilon_1 \neq 0$ and/or $\epsilon_2 \neq 0$:

$$\langle K_S^0 | K_L^0 \rangle = \frac{\epsilon_1^* + \epsilon_2}{\sqrt{1+|\epsilon_1|^2} \sqrt{1+|\epsilon_2|^2}}. \quad (\text{A.23})$$

Neglecting higher order terms in ϵ_1 and ϵ_2 , we get

$$\langle K_S^0 | K_L^0 \rangle \simeq 2(\Re \hat{\epsilon} - i\Im \delta). \quad (\text{A.24})$$

CP is violated, if $\Re \hat{\epsilon} \neq 0$. The phase between $|K^0\rangle$ and $|\bar{K}^0\rangle$ can be chosen³⁴, such that $\hat{\epsilon}$ and δ are small. It is then seen from A.22, that K^0 and \bar{K}^0 have almost equal mixture of K_L^0 and K_S^0 . The deviation from equal mixture is the consequence of CP violation (CPT violation respectively).

³⁴We will fix the phase later in the so-called Wu Yang convention (eq.A.51)

It can be shown, that [59]:

If CPT invariance holds

$$M_{11} = M_{22}$$

$$\Gamma_{11} = \Gamma_{22}$$

$$\epsilon_1 = \epsilon_2 = \hat{\epsilon}$$

$$\delta = 0$$

$$\langle K_S^0 | K_L^0 \rangle = 2\Re\hat{\epsilon} \quad \text{real}$$

if T invariance holds

$$\frac{\Gamma_{12}^*}{\Gamma_{12}} = \frac{M_{12}^*}{M_{12}}$$

$$\delta = \epsilon_1 = -\epsilon_2$$

$$\hat{\epsilon} = 0$$

$$\langle K_S^0 | K_L^0 \rangle = 2i\Im\delta \quad \text{imaginary}$$

Finally we express $|K^0\rangle$ and $|\bar{K}^0\rangle$ in terms of $|K_S^0\rangle$ and $|K_L^0\rangle$, neglecting higher order terms of $\hat{\epsilon}$ and δ :

$$\begin{aligned} |K^0\rangle &\simeq \frac{1}{\sqrt{2}}(1 - \hat{\epsilon} + \delta) |K_S^0\rangle + (1 - \hat{\epsilon} - \delta) |K_L^0\rangle \\ |\bar{K}^0\rangle &\simeq \frac{1}{\sqrt{2}}(1 + \hat{\epsilon} - \delta) |K_S^0\rangle - (1 + \hat{\epsilon} + \delta) |K_L^0\rangle. \end{aligned} \quad (\text{A.25})$$

Note:

So far we only used the basic principles of quantum mechanics. In addition we have not (yet) fixed the phase between $|K^0\rangle$ and $|\bar{K}^0\rangle$.

A.2.1 Interference Phenomena

First we calculate the time development of an arbitrary state of the K meson:

At $\tau = 0$:

$$|\psi(\tau = 0)\rangle = a_s |K_S^0\rangle + a_l |K_L^0\rangle = \begin{pmatrix} a_s \\ a_l \end{pmatrix} \quad (\text{A.26})$$

where τ is the time in the rest frame of the neutral kaon system.

At a later time τ we have

$$|\psi(\tau)\rangle = a_s e^{-(im_s + \frac{1}{2}\gamma_s)\tau} |K_S^0\rangle + a_l e^{-(im_l + \frac{1}{2}\gamma_l)\tau} |K_L^0\rangle. \quad (\text{A.27})$$

The rate into the final state $|f\rangle$ is given by

$$R_f(\tau) = 2\pi\rho_f |\langle f | H_{wk} | \psi(\tau) \rangle|^2 \quad (\text{A.28})$$

where ρ_f is the density of the final state.

The partial width ³⁵ into a final state is defined as

$$\begin{aligned}\gamma_s(f) &= 2\pi\rho_f |\langle f | H_{wk} | K_S^0 \rangle|^2 \\ \gamma_l(f) &= 2\pi\rho_f |\langle f | H_{wk} | K_L^0 \rangle|^2 \\ \eta_f &= \sqrt{\gamma_s(f)\gamma_l(f)} e^{i\phi_f} = \frac{\langle f | H_{wk} | K_S^0 \rangle^* \langle f | H_{wk} | K_L^0 \rangle}{\langle f | H_{wk} | K_S^0 \rangle \langle f | H_{wk} | K_S^0 \rangle}.\end{aligned}\quad (\text{A.29})$$

Combining A.28 and A.29 we get

$$\begin{aligned}R_f(\tau) &= \gamma_s(f) \left(|a_s|^2 e^{-\gamma_s\tau} + |a_l|^2 |\eta_f|^2 e^{-\gamma_l\tau} \right. \\ &\quad + (a_s^* a_l |\eta_f| e^{i\phi_f} e^{-i(m_l - m_s)\tau} e^{-\frac{\gamma_s + \gamma_l}{2}\tau} \\ &\quad \left. + (a_l^* a_s |\eta_f| e^{-i\phi_f} e^{-i(m_s - m_l)\tau} e^{-\frac{\gamma_s + \gamma_l}{2}\tau} \right).\end{aligned}\quad (\text{A.30})$$

We now regard the special case of an initially pure $|K^0\rangle$ and $|\bar{K}^0\rangle$ state. Combining A.30 and A.25 we get in first order of $\hat{\epsilon}$ and δ :

$$\begin{aligned}R_f(\tau, K^0[\bar{K}^0]) &= 2\gamma_s(f) \left(\left(\frac{1}{2} \mp \Re\hat{\epsilon} \pm \Re\delta \right) e^{-\gamma_s\tau} + |\eta|^2 \left(\frac{1}{2} \mp \Re\hat{\epsilon} \mp \Re\delta \right) e^{-\gamma_l\tau} \right. \\ &\quad \left. \pm 2|\eta_f| \left(\frac{1}{2} \mp \Re\hat{\epsilon} \mp \Im\delta \right) e^{-\frac{\gamma_s + \gamma_l}{2}\tau} \cos((m_s - m_l)\tau - \phi_f) \right)\end{aligned}\quad (\text{A.31})$$

The upper sign is for K^0 , the lower for \bar{K}^0 .

The asymmetry into the final state $|f\rangle$ is defined as

$$A_f(\tau) = \frac{R_f(\tau, \bar{K}^0) - R_f(\tau, K^0)}{R_f(\tau, K^0) + R_f(\tau, \bar{K}^0)}.\quad (\text{A.32})$$

Using A.31 and assuming CPT invariance ($\delta = 0$) we get

$$A_f(\tau) = \frac{2\Re\hat{\epsilon} - 2\left(\frac{1}{2} \mp \Re\hat{\epsilon}\right) |\eta_f| e^{-\frac{\gamma_l - \gamma_s}{2}\tau} \cos((m_s - m_l)\tau - \phi_f)}{1 + |\eta_f|^2 e^{-(\gamma_l - \gamma_s)\tau}}.\quad (\text{A.33})$$

Figure 1 (page 10) shows the asymmetry for the final state $|f\rangle = |\pi^+\pi^-\rangle$ for $0 < \tau < 30\tau_s$.

From A.33 we can see, why the neutral kaon system is an ideal place to study interference effects.

- $\gamma_s \gg \gamma_l$:

This is due to the fact, that K_L^0 decays into two body final states violate CP. Less phase space is available for the CP conserving 3π final state. So it is easy to experimentally separate the "short" and "long" decay mode by either studying a neutral kaon beam close to the production point or far away.

Furthermore the CP violating decay mode of K_L^0 is easier to detect, because the CP allowed decay rate is so slow.

³⁵By γ_s we denote the total width of the K_S^0 , by $\gamma_s(f)$ the partial width into a final state.

- $m_l - m_s \simeq \frac{1}{2}\gamma_s$:

This leads to an observable interference effects, as the K_S^0 does not disappear too fast with respect to the cosine oscillation.

It should be stressed, that those are features specific to the neutral kaon system. They make it the prime particle to study CP violation.

A.2.2 Decay into $\pi\pi$

Note: From now on we assume CPT invariance, unless explicitly stated.

The relevant amplitudes in terms of the physical particles are:

$$\eta_{+-} = \frac{\langle \pi^+\pi^- | H_{wk} | K_L^0 \rangle}{\langle \pi^+\pi^- | H_{wk} | K_S^0 \rangle} \quad (\text{A.34})$$

$$\eta_{00} = \frac{\langle \pi^0\pi^0 | H_{wk} | K_L^0 \rangle}{\langle \pi^0\pi^0 | H_{wk} | K_S^0 \rangle}. \quad (\text{A.35})$$

The amplitudes in terms of isospin eigenstates are

$$A_0 e^{i\delta_0} = \langle \pi\pi, I=0 | H_{wk} | K^0 \rangle \quad (\text{A.36})$$

$$A_0^* e^{i\delta_0} = \langle \pi\pi, I=0 | H_{wk} | \overline{K^0} \rangle \quad (\text{A.37})$$

$$A_2 e^{i\delta_2} = \langle \pi\pi, I=2 | H_{wk} | K^0 \rangle \quad (\text{A.38})$$

$$A_2^* e^{i\delta_2} = \langle \pi\pi, I=2 | H_{wk} | \overline{K^0} \rangle \quad (\text{A.39})$$

where:

δ_i is the strong interaction $\pi\pi$ phase shift for states with isospin I at the center of mass energy m_{K^0} .

Isospin decomposition of the final $\pi\pi$ states yields:

$$\langle \pi^+\pi^- | = \sqrt{\frac{2}{3}} \langle \pi\pi, I=0 | + \sqrt{\frac{1}{3}} \langle \pi\pi, I=2 | \quad (\text{A.40})$$

$$\langle \pi^0\pi^0 | = \sqrt{\frac{1}{3}} \langle \pi\pi, I=0 | - \sqrt{\frac{2}{3}} \langle \pi\pi, I=2 |. \quad (\text{A.41})$$

We define

$$t_0 = \frac{\Im A_0}{\Re A_0} \quad (\text{A.42})$$

$$t_2 = \frac{\Im A_2}{\Re A_2} \quad (\text{A.43})$$

and combine A.34 - A.41 to get

$$\eta_{+-} = \epsilon + \frac{\epsilon'}{1 + \frac{1}{\sqrt{2}}\omega} \quad (\text{A.44})$$

$$\eta_{00} = \epsilon - \frac{2\epsilon'}{1 - \frac{1}{\sqrt{2}}\omega} \quad (\text{A.45})$$

where

$$\epsilon = \frac{\langle \pi\pi, I=0 | H_{wk} | K_L^0 \rangle}{\langle \pi\pi, I=0 | H_{wk} | K_S^0 \rangle} \quad (\text{A.46})$$

$$= \frac{\hat{\epsilon} + it_0}{1 + i\hat{\epsilon}t_0} \quad (\text{A.47})$$

$$\omega = \frac{\langle \pi\pi, I=2 | H_{wk} | K_S^0 \rangle}{\langle \pi\pi, I=0 | H_{wk} | K_S^0 \rangle} \quad (\text{A.48})$$

$$= \frac{\Re A_2}{\Re A_0} \frac{\hat{\epsilon} + it_2}{1 + i\hat{\epsilon}t_0} e^{i(\delta_2 - \delta_0)} \quad (\text{A.49})$$

$$\begin{aligned} \epsilon' &= \frac{i \Re A_2}{\sqrt{2} \Re A_0} \frac{1 + i\hat{\epsilon}t_2}{1 + i\hat{\epsilon}t_0} \\ &\quad (1 - \hat{\epsilon}^2) e^{i(\delta_2 - \delta_0)} \frac{t_2 - t_0}{(1 + i\hat{\epsilon}t_2)(1 + i\hat{\epsilon}t_0)}. \end{aligned} \quad (\text{A.50})$$

So far we have not specified the phase between $|K^0\rangle$ and $|\bar{K}^0\rangle$.

One common choice is the Wu-Yang phase convention [60]:

$$A_0 \text{ real.} \quad (\text{A.51})$$

From now on we use this convention.

We then get

$$t_0 = 0 \quad (\text{A.52})$$

$$\hat{\epsilon} = \epsilon \quad (\text{A.53})$$

$$\epsilon' = \frac{i \Re A_2}{\sqrt{2} \Re A_0} (1 + i\hat{\epsilon}t_2) (1 - \hat{\epsilon}^2) e^{i(\delta_2 - \delta_0)} \frac{t_2}{(1 + i\hat{\epsilon}t_2)(1 + i\hat{\epsilon}t_0)} \quad (\text{A.54})$$

$$\simeq \frac{i \Re A_2 \Im A_2}{\sqrt{2} \Re A_0 \Re A_2} e^{i(\delta_2 - \delta_0)} = \frac{i \Im A_2}{\sqrt{2} \Re A_0} e^{i(\delta_2 - \delta_0)} \quad (\text{A.55})$$

where in equation A.55 $\hat{\epsilon} \ll 1$ has been assumed.

One advantage of the Wu-Yang phase convention is, that $\hat{\epsilon} = \epsilon$ ³⁶, and $\hat{\epsilon}$ becomes therefore a measureable quantity.

³⁶Note, that η_{00}, η_{+-} are the measureable quantities. $\hat{\epsilon}$, as it has been used so far, is a phase dependent, nonphysical quantity, whose real part is a measure of CP violation.

The equations derived so far hold exactly.

They can be simplified by taking the order of magnitude of various parameters into account.

From experiment we know, that the $|\Delta I| = 3/2$ rule [61] is valid, hence

$$\left| \frac{A_2}{A_0} \right| \simeq \frac{1}{20} \quad (\text{A.56})$$

Neglecting $|A_2|$ and second and higher order terms in ϵ we get the well known relations, giving raise to the Wu-Yang triangle (see fig. 35)

$$\eta_{+-} \simeq \epsilon + \epsilon' \quad (\text{A.57})$$

$$\eta_{00} \simeq \epsilon - 2\epsilon'. \quad (\text{A.58})$$

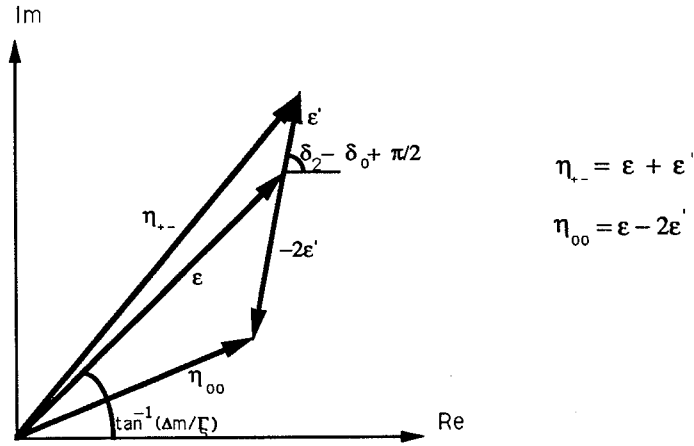


Figure 35: The Wu-Yang triangle for the $|\pi\pi\rangle$ decay of the neutral kaon system.

We turn our attention to the parameter ϵ' , defined in A.50. It is a new CP violating parameter, arising from a phase difference between the $|\pi\pi, I = 0\rangle$ and $|\pi\pi, I = 2\rangle$ states. Whereas ϵ describes CP violation in the mass and decay matrix, ϵ' describes CP violation in the transition matrix ³⁷. It is suppressed by $|\Delta I| = 3/2$

³⁷Thus we see, if ϵ'/ϵ is not zero, then both conclusions drawn in the introduction (page 85) are true.

rule (eq. A.56, A.55).

From A.57 and A.58 we can get an approximation of ϵ'/ϵ :

$$|\eta_{+-}| \simeq |\epsilon| + |\epsilon'| \quad (\text{A.59})$$

$$|\eta_{00}| \simeq |\epsilon| - 2|\epsilon'| \quad (\text{A.60})$$

$$|\epsilon'/\epsilon| \simeq \frac{1}{6}(1 - |\frac{\eta_{00}}{\eta_{+-}}|) \quad (\text{A.61})$$

The neutral kaon system decays predominantly into $|\pi\pi\rangle$. All other decay rates ($|\pi\pi\pi\rangle$, $|\pi l\nu\rangle$ etc..) are at least 3 orders of magnitude smaller. We can use this experimental fact to combine A.15 and A.25 to get

$$(-i(m_l - m_s) + \frac{\gamma_s + \gamma_l}{2}) \langle K_L^0 | K_S^0 \rangle = \sum \eta_f^* \Gamma_f \simeq \eta_{+-}^* \Gamma_{s+-} + \eta_{00}^* \Gamma_{s00}. \quad (\text{A.62})$$

The phases of η_{+-} , η_{00} , ϵ and ϵ' can be estimated using A.62, A.57, A.58. CPT invariance leads to the following conditions [5]:

$$\phi_{+-} \simeq \phi_{00} \simeq \phi_\epsilon \simeq \phi_{SW} \quad (\text{A.63})$$

$$\phi_{\epsilon'} = \delta_2 - \delta_0 \pm \pi \quad (\text{A.64})$$

$$\phi_{SW} = \arctan \frac{2(m_l - m_s)}{\gamma_s} = 43.7 \pm 0.3^\circ \quad (\text{A.65})$$

ϕ_{SW} is called the superweak angle.

A.2.3 CP Violation in Other Decay Modes of the Neutral Kaon System

We first discuss the **semileptonic decay mode of $|K_L^0\rangle$** .

The neutral kaon system can also decay into $|\pi l\nu\rangle$, where l stands for a lepton (μ, e).

The $\Delta S = \Delta Q$ rule states, that

$$|K^0\rangle \rightarrow |\pi^- l^+ \nu\rangle \quad (\text{A.66})$$

$$|\bar{K}^0\rangle \rightarrow |\pi^+ l^- \bar{\nu}\rangle. \quad (\text{A.67})$$

The ratio of the allowed to the forbidden amplitude

$$x = \frac{A(\bar{K}^0 \rightarrow \pi^- l^+ \nu)}{A(K^0 \rightarrow \pi^- l^+ \nu)} \quad (\text{A.68})$$

describes a possible violation of this $\Delta S = \Delta Q$ rule.

The charge asymmetry for an initial state $|\psi(\tau = 0)\rangle$ of the neutral kaon system is defined as

$$\Delta_c(\tau) = \frac{R^+(\tau) - R^-(\tau)}{R^+(\tau) + R^-(\tau)} \quad (\text{A.69})$$

where $R^\pm(\tau)$ is the rate $|\psi(\tau)\rangle \rightarrow |\pi^\mp l^\pm \nu\rangle$. Using A.25 we get for long lifetimes $\tau \gg \tau_s$ (i.e. only K_L^0 left) a constant charge asymmetry

$$\Delta_c(\tau) = \delta_c = \frac{2(1 - |x|^2)}{|1 - x^2|} \Re \hat{\epsilon} \quad (\text{A.70})$$

δ_c is due to the fact, that $|K_L^0\rangle$ has not equal contribution from $|K^0\rangle$ and $|\bar{K}^0\rangle$. It is proportional to $\Re \hat{\epsilon}$, the parameter describing this unequal mixing of $|K^0\rangle$ and $|\bar{K}^0\rangle$ in $|K_L^0\rangle$.

So far CP violation has only been seen in the $|\pi\pi\rangle$ and in the semileptonic decay mode.

Other CP violating decay modes of the neutral kaon are also expected, which we just mention, before discussing the current experimental status.

- $|K_S^0\rangle \rightarrow |\pi\pi\pi\rangle$
- $|K^0\rangle \rightarrow |\gamma\gamma\rangle$ [62]
- $|K_L^0\rangle \rightarrow |\pi^0 e^+ e^-\rangle$.

These decays are experimentally difficult to measure, as they have small branching ratios and involve the detection of neutral particles.

A.3 The Current Experimental Status

CP violation has only be observed in the decay of the K_L^0 so far. Table 16 lists the current status, on which we make now some comments.

The measurement of $|\eta_{00}|$ and ϕ_{00} is difficult, as it includes the reconstruction of neutral final states. Recent experiments have therefore concentrated on measuring simultaneously neutral and charged two pion final states, yielding $|\eta_{00}/\eta_{+-}|$ and the phase difference $|\phi_{+-} - \phi_{00}|$. This method has the advantage of reduced systematic errors with respect to separate measurements of the final states $|\pi^+\pi^-\rangle$ and $|\pi^0\pi^0\rangle$.

Table 16: *List of measured CP violating parameters.*

parameter	value	reference
$ \eta_{+-} $	$(2.268 \pm 0.023) 10^{-3}$	[63]
ϕ_{+-}	46.0 ± 1.2	[63]
$ \eta_{00} $	$(2.253 \pm 0.024) 10^{-3}$	[63]
ϕ_{00}	48.5 ± 3.1	[63]
$\phi_{+-} - \phi_{00}$	$0.2 \pm 2.9 \pm 1.1$	[64]
$\phi_{+-} - \phi_{00}$	-0.3 ± 2.7	[65]
$ \epsilon'/\epsilon $	$(3.3 \pm 1.1) 10^{-3}$	[66]
$ \epsilon'/\epsilon $	$(-0.5 \pm 1.5) 10^{-3}$	[67]
δ_c	$0.327 \pm 0.012 \%$	[63]

Lately two experiments have used this approach to measure $|\epsilon'/\epsilon|$ from $|\eta_{00}/\eta_{+-}|$ using eq. A.61 [66,67]. Their results differ by two standard deviations. It should be noted, that some of the systematic errors of the two experiments are different. Both experiments also presented the measurement of the phase difference $\phi_{+-} - \phi_{00}$ [64,65], which has found to be small, as required by CPT invariance (eqs. A.63 - A.65).

The charge asymmetry δ_c has been measured in the semileptonic decay of K_L^0 at large lifetimes for the final states $|\pi e \nu >$, $|\pi \mu \nu >$ and $|\pi l \nu >$, where l stands for either e or μ . The three results for the different final states are consistent with each other.

B Appendix

B.1 The VALET PLUS

The VALET PLUS ³⁸ was developed at CERN as an easy to use system for testing electronic equipment. Later it was embedded into the data acquisition chain of large experiments, which may comprise several VALETs, as well as workstations or microvaxes for controlling them.

We will describe here only those features of the VALET PLUS, that are used by CPLEAR. A more complete overview with further references can be found in [68].

In terms of hardware the VALET PLUS consists of a VME crate with CPU and a ROM card containing the firmware. CPLEAR uses the FIC 8230 ³⁹ as CPU. Any VME compatible module can be added to this minimal configuration, e.g. CPLEAR uses features such as Ethernet and SCSI interfaces, optical data link, I/O module, Fastbus interface etc.

The SOFTWARE modules of the VALET are based on the CERN standard software packages. MoniCa is used as a monitor for the M680X0 processor family. PILS (Portable Interactive Language System) has been developed at CERN as a simple, interactive language for the VALET. It contains ANSI MINIMAL BASIC, but additional features like data types, modules etc have been added. Execution speed is improved significantly by its compiler.

Several CERN libraries have been rewritten for use with the VALET (CAMAC, CERN histogram package, mathematical libraries etc). It is also possible to directly use the M680X0 exception vectors within PILS.

Although normally programmed in PILS, other languages can be used with the help of CERN crosscompilers. Most of the code for CPLEAR is written in PILS, only time critical code is written in assembler.

There are several possible ways to control the VALET. CPLEAR controls them, during data taking, in so-called DETACHED mode ⁴⁰. This means, that the (PILS) code is loaded from the VAX over ETHERNET into the VALET at bootup time and

³⁸Vme Applied to Laboratory Equipment Test.

³⁹Trademark of Creative Electronic Systems (CES), rue du pont-butin 70, CH-1213 PETIT-LANCY 1.

⁴⁰E.g. another possibility is to connect each VALET to a PC.

started. The VALET then sits in a loop and performs the appropriate action, as the data is passed through the data acquisition chain. There is no direct communication with the user and no terminal is attached to the VALET for output. If the VALET detects specific error conditions, it can send messages over ETHERNET to the VAX. The VAX in turn can also pass well defined commands to the VALET, like start a run, end the current run, ask about status, send histogram etc.

The VAX software to control the VALET of CPLEAR makes heavy use of MODEL [69,70], a CERN written package for online control of large experiments. It includes an event buffer manager (MBM), data logger, human interface, window manager, menu, dialogue and panel packages, process control utilities, error message utility and run control processes.

B.2 FIC8230

CPLEAR uses the FIC 8230 as CPU for all VALETs. The following features of the FIC are relevant for the CPLEAR use of this module ⁴¹:

- M68020 16MHz processor with floating point coprocessor FPU 68881
- DMAC WE 32104 (see below)
- 128 kby SRAM
- global memory of 4 Mby
- VSB interface
- 4 communication FIFOs (First In, First Out).

DMA Controller WE 32104:

As mentioned above the FIC 8230 has a Wester Electronics WE 32104 DMAC, which supports transfers across the 4 Gby addressing range. As CPLEAR makes heavy use of this device, we describe it here in some detail.

The WE 32104 has 4 independent channels, which allow four transfers at the same time. Each channel has a fixed priority, channel 0 being the highest. An 8 bit peripheral bus is supported, which is connected to the FIC front panel general purpose connector.

⁴¹This list is not intended to be complete. We refer to the manufacturer's data sheet for further information [71].

For memory to memory transfers byte, halfword, word, double or quad word transfers are supported.

Memory to memory transfers can be done at rates up to 14.4 Mby/sec ⁴² at 18 Mhz, memory to peripheral transfers up to 7.8 Mby/sec.

A typical DMA transfer occurs in three phases: Initialization, data transfer and termination. At initialization the CPU writes the necessary information for the transfer into the corresponding DMA registers, typically source address, destination address and word count. Then the channel is started. During the data transfer phase, the DMA honours peripheral bus requests and/or requests the system bus/peripheral bus. The internal registers are updated, as the data is transferred.

The termination phase is reached when the transfer counter reaches zero. If the IE (interrupt enable) bit in the mode register is set, an interrupt is generated: If the transfer was successfully terminated, the normal interrupt vector (if the normal termination (NT) bit is set in the status and control register) is put on the bus, otherwise the error interrupt vector.

The WE 32104 can also be used in chained mode. Here one prepares a list of request blocks in memory with the following format: 1. source address, 2. destination address, 3. transfer count, 4. base address. The base address is a pointer to the next request block. The CPU writes the address of the first request block into the base address register at initialization time. Each time a transfer is finished (i.e. the DMA transfer counter has reached 0), the base address register is used to fetch the next request block automatically. The chained transfer is over, when the base address 0 is encountered, and the channel enters termination phase as described above.

B.3 The VME Vertical Bus VMV

CPLEAR uses the CES modules VBE 8213 and VBR 8212 as interfaces to the vertical bus. We explain these two modules, as far as their usage in the CPLEAR experiment is concerned, after a short introduction to the vertical bus (for further information we refer to the manufacturer's data sheet.). Bus access conflicts between the Ethernet interface and the VMV lead to bus errors in the CPLEAR configuration. Their handling is discussed at the end of this appendix.

⁴²These rates can only be obtained for transfers within the FIC card itself.

B.3.1 General Principles of the VMV bus

The VMV bus is the extension of the VME bus to a multicrate environment. Its principle have been adapted from the idea of the CAMAC bus.

In CAMAC each crate's activity is organized by its crate controller. Several crates can be linked by the branch highway to form a multicrate system. A maximum of 7 crates can be linked together per branch. The branch controller organizes the activity on this branch highway. There is only one branch controller per branch.

The VMV bus is more versatile. It allows multi-master operation. So there can be more than one master per VMV bus.

Transfers between master and slave are done in a transparent way without additional software. A VMV cycle looks for the user just like a VME cycle in one crate, but of course the cycle is transmitted over VMV into a VME cycle in another crate.

B.3.2 The CES Modules VBE 8212 and VBR 3213

The **VBR 8212** corresponds to the CAMAC crate controller. It must be present in each VME crate connected to the VMV bus. Its function is to transfer the VMV cycle addressed to its crate into a VME cycle. It is therefore a VMV slave and a VME master. It supports all VME cycle types: A32, D32, D16, D8 in all modes: read, write, read modify write, block mode, ascending mode.

The **VBE 8213** has the function of a CAMAC branch driver. It transforms a VME cycle into a VMV cycle, so it is a VME slave and a VMV master. The presence of the VBE is only required in those crates, from where the VMV bus needs to be accessed.

B.3.3 VMV Addressing Modes:

There are two different types of addressing mode for the VMV bus. For both the crate number and the address in that crate have to be determined.

- **Window mode:**

The VBE has a 1 Mby window space, which can be mapped anywhere into the VME space in the master crate. Performing VME cycles at those addresses then lead to the propagation of the VME cycle over VMV. The crate number, at which the VMV cycle has to be converted into a VME one, is set in the internal register MAPCR in the VBE. If this register is set to 0, then the cycle

is performed in broadcast mode, that means in all crates connected to the VMV bus ⁴³. If the cycle is a read cycle, then the OR of all crates is read.

The higher address lines (A31 - A20) in the VBR crate is taken from the VBE internal register MAPAD and the A19 - A1 are transmitted directly. DS0, DS1, D0 - D31, DTACK and BERR are also directly transmitted. The AM (address modifiers) are either transmitted directly, or taken from the MAPAM register of the VBE, depending on the AMM bit in the CSR of the VBE.

- **Autorouting:**

The crate number is determined by the higher address lines in this mode. CPLEAR does not use it.

B.3.4 VMV Setup in CPLEAR

The VMV is initialised as follow:

- **VBE 8213:**

Address modifiers AM transmitted directly, window mode, internal timeout not activated, timeout generates bus error VMV arbitration: ROR (Release On Request). No interrupts are used.

- **VBR 8212:**

VME arbitration ROR (Release On Request), bus request level 2.

B.3.5 Timeout Handling on the Vertical Bus

One particular problem deserves to be mentioned separatly: The LRT card has no onboard memory. This has the consequence that, whenever an Ethernet packet for a specific VALET arrives, the LRT DMAC must be able to become VME bus master within about 10 μsec . Therefore the LRT card is given the highest bus request level (level 3).

The VBR card is then put on bus request level 2. But the LRT card can in this configuration lock the VBR card out, and a bus error occurs. Those have to be handled in software by the DDS, depending on whether the cycle was performed by CPU or WE 32104 DMAC.

If the CPU tried to perform a VMV cycle, one gets a normal bus error. The CPU saves several register as part of the bus fault exception stack frame [72], and the bus

⁴³More exactly: in all those crates, where the VBR module is set online.

error interrupt service routine is entered. This routine checks, that the bus error occurred on a VMV address and in this case the cycle can be repeated, until it is successfully completed.

The bus errors are handled in a different way, if the WE 32102 DMAC was performing the cycle. This DMAC can be programmed to rerun an unsuccessful cycle up to four times, until it is aborted with a fault. This will solve most of the timeouts on the vertical bus, but not all. If a bus error occurs, the WE 32104 will output the error interrupt vector. The CPU transfers in the corresponding ISR the remaining bytes from the internal register of the DMAC to its destination over VMV. After this is done, the registers of the DMAC have to be updated and the DMAC is started again to complete the transfer.

C Appendix

Detector Performance during Run Period P5 (December 1989)

The data of this thesis has been taken in December 1989 with the CPLEAR detector in an early and in view of the CP experiment still incomplete state of construction and performance. Some components still have to be added and final adjustments have to be made in the future.

Most of the performance values mentioned below have in the meantime (December 1990) been improved.

This section gives only a an overview of the detector performance during the run in December 1989. A more detailed description can be found in [7].

- PROPORTIONAL CHAMBERS:

Only the wires of PC1 were read out. Due to initial technical problems the overall efficiency was about 80%.

- DRIFT CHAMBERS:

All the wires of DC1 - DC6 were read out. Cathode strip information was available from DC1 (U and V strips), DC2 (U and V strips) and DC6 (U strips). The efficiency of the chambers was between 83-95 %. The main reason for this worse than expected efficiency was missing channels of the read out system.

The design value for the resolution of the chambers was not achieved due to noise and crosstalk, and was found to be $380\text{ }\mu\text{m}$.

The efficiency of the strips was approximately 75 %.

The momentum resolution of the fit was 7 % below 200 MeV/c, raising to 20 % at 1 GeV/c.

- STREAMER TUBES:

The ST had an inefficiency of 3 % (dead channels included). The resolution was 2.2 cm. In addition to this resolution there was a trigger dependent, intermittent displacement of the measured z value by 10 cm. This was due to electronic gating problems in the TDCs.

- PID:

The final read out system of the PID was not yet operational in December 1989.

Therefore commercial available electronics based on the CAMAC standard was used. Due to the speed of CAMAC the read out time per event was 4 msec.

- **CALORIMETER:**

The calorimeter was not branched into the normal data acquisition chain.

- **DATA ACQUISITION SYSTEM:**

The data acquisition system was fully operational. However, access problems to the 2SB cards of the event builder over VME and VSB lead to data corruption.

This meant, that a small part of the data was no longer in ZEBRA format and was afterwards unreadable.

References

- [1] CPLEAR Proposal, CERN/PSCC/85-6.
- [2] CPLEAR Letter of Intent, CERN/PSCC/83-28.
- [3] CPLEAR Addendum to the Proposal, CERN/PSCC/85-30.
- [4] L.M.Sehgal and L.Wolfenstein, Phys.Rev. **162** (1965) 162.
- [5] V.V.Barmin et al., Nucl.Phys. **B247** (1984) 293.
- [6] C.Bula, Ph.D. thesis, Eidg. Tech. Hochschule Zurich, to be submitted 1991.
- [7] M.Dodgson, Ph.D. thesis University of Liverpool, 1990, unpublished.
- [8] R.Rickenbach, Ph.D. thesis, University of Basel, 1988, unpublished.
- [9] R.Rickenbach et al., Nucl.Instr. and Methods **A279** (1989) 305.
- [10] P.Bloch et al., submitted to Nucl.Instr.and Methods (1990).
- [11] A.Schopper, Ph.D. thesis, University of Basel, 1988, unpublished.
- [12] D.A.Troester et al., Nucl.Instr. and Methods **A279** (1989) 285.
- [13] U.Johner, Ph.D. thesis, University of Fribourg, to be submitted 1991.
- [14] CPLEAR Online Data Structure, CPLEAR Online Note 048-1 1989.
- [15] VMV User's Manual, CES, available from the manufacturer.
- [16] The KATE Package, CPLEAR Online Note 50.b 1990.
- [17] R.Brun et al., PAW Physics Analysis Workstation, CERN Program Library Q121, Geneva, 1989.
- [18] M.Doser et al., Nucl.Phys. **A486** (1988) 493.
- [19] M.Doser PhD. Thesis, University of Zurich, 1988, unpublished.
- [20] A.G.Wightman, Phys. Rev. **77** (1950) 521.
- [21] E.Borie et al., Phys. Rev. **21** (1980) 1460.
- [22] O.D.Dal'karov et al., Sov. J. Nucl. Phys. **25(4)** (1977) 455.

- [23] L.Bracci and G.Fiorentini, Nuovo Cimento A **43** (1978) 9.
- [24] G.Reifenroether et al., Phys.Lett. B **214** (1988) 325.
- [25] M.Leon et al., Phys. Rev. **127** (1962) 636.
- [26] T.B.Day et al., Phys. Rev. Lett. **3** (1959) 61.
- [27] J.M.Richard and M.E.Sainio, Phys.Lett. **110B** (1982) 349.
- [28] T.B.Day et al., Phys. Rev. **118** (1960) 864.
- [29] M.Ziegler et al., Phys.Lett. **B206** (1988) 151.
- [30] R.Armenteros and B.French, High Energy Physics, edited by E.H.S.Burhop, Academic Press, N.Y., 1969, p.237.
- [31] T.Tanimori et al., Phys.Rev. **D 41** (1990) 744.
- [32] Rossi et al.,Phys. Rep. **63** (1980) 149.
- [33] C.Dover et al., Nucl. Phys. **B244** (1984) 349.
- [34] M.Kohno et al., Phys. Lett. **152B** (1985) 303.
- [35] M.Kohno et al., Nucl. Phys. **A454** (1986) 429.
- [36] M.Maruyama et al., Prog. Theo. Phys. **73** (1985) 1211.
- [37] M.Maruyama et al., Prog. Theo. Phys. **78** (1987) 841.
- [38] J.Ellis et al., Phys. Lett. **217B** (1989) 173.
- [39] J.Ashman et al., Phys.Lett. **206** (1988) 364.
- [40] U.Wiedner et al., Phys.Rev.Lett. **58** (1987) 648.
- [41] U.Wiedner et al., Phys.Rev. **D 40** (1989) 3568.
- [42] CRYSTAL BARREL Proposal, CERN/PSCC/85-56.
- [43] OBELIX Proposal, CERN/PSCC/86-4.
- [44] Geant 3, DD/EE 84-1, Data Handling Division, CERN, Geneva 1987.
- [45] F.James and M.Roos, D506 Minuit, CERN, Geneva, 1989.
- [46] M.Foster et al., Nucl.Phys. **B6** (1968) 107.

- [47] C.Ghesquiere, Symp. on $\overline{N}N$ interactions, Libice, CERN Yellow Report 74-18(1974) 436.
- [48] C.Baltay et al., Phys.Rev.Lett. **15** (1965) 532.
- [49] G.Bardin et al., Proc. III LEAR workshop, 19-26 January 1985, Tignes-Savoie France.
- [50] M.Soulliere, PhD Thesis, Pennsylvania State University, 1987, unpublished.
- [51] G.C.Oades et al., Nucl.Phys. **A464** (1987) 538.
- [52] E.Klempt et al., Proc. IV LEAR Workshop, Villars, Switzerland, 1987 (Harwood Acad. Publ.) p.429.
- [53] G.Reifenroether and E.Klempt, submitted to Nucl.Phys. A 1990.
- [54] B.May et al., Z.Phys.C **46** (1990) 191.
- [55] B.May et al., Z.Phys.C **46** (1990) 203.
- [56] J.H.Christenson, J.W.Cronin, V.L.Fitch and R.Turlay, Phys.Rev.Lett. **13** (1964) 138.
- [57] Lueders G. and Zumino B., Phys.Rev. **106** (1957) 385.
- [58] R.Jost, Helv.Phys.Acta **30** (1957) 409.
- [59] T.D.Lee, Particle Physics and Introduction to Field Theory, Harwood Academic Publishers, 1981.
- [60] T.T.Wu and C.N.Yang, Phys.Rev.Lett. **13** (1964) 380.
- [61] E.D.Commins and P.H.Bucksbaum, Weak Interactions of Leptons and Quarks, Cambridge 1983.
- [62] R.Decker et al., Z.Phys.C **28** (1985) 117.
- [63] Particle Data Group, Phys.Lett. **239** (1990).
- [64] R.Carosi et al., CERN-EP 90-06, submitted to Phys.Lett. **B**.
- [65] M.Karlsson et al., submitted to Phys.Rev.Lett. 1990.
- [66] H.Burkhardt et al., Phys.Lett. **206** (1988) 169.

- [67] B.Winstein, Proc.XIV Int. Symposium on Lepton and Photon Interactions, Stanford,1989.
- [68] Y.Perrin et al., The Valet-Plus Embedded into Large Physics Experiments, VMEbus IN RESEARCH, conf. ETH Zurich, 11-13 October 1988, 59.
- [69] M.D.Sendall et al, Computer Physics Communications **57** (1989) 343.
- [70] C.Boissat et al, Computer Physics Communications **57** (1989) 512.
- [71] FIC 8230 User's Manual, CES, available from the manufacturer.
- [72] MC68020 User's Manual, Prentice-Hall, 1985.

List of Figures

1	Time dependent asymmetry $A_{\pi\pi}(\tau)$	10
2	Transversal view of the CPLEAR detector	14
3	Detail of the transversal view of the detector	14
4	Longitudinal view of the CPLEAR detector	15
5	Beam stopping distribution	16
6	Doublet structure of the drift chambers	17
7	Layout of the trigger	22
8	Timing of the trigger	23
9	The idea of the p_T cut	24
10	Layout of the CPLEAR data acquisition system	33
11	Data flow chart of the CPLEAR experiment	34
12	Data transfer from FE to EB	36
13	Principle of VMV operation	39
14	Data transfer in the EPS VALET	44
15	Principle of the VALET - VAX communication	45
16	Radiative transitions	51
17	Quark graphs for $p\bar{p}$ annihilation into 2 final state mesons	55
18	Quark antiquark vertices	55
19	Quark line diagram for K^+K^- backward peak	57
20	Data reduction	60
21	Offline display of two events	61
22	Momentum distribution of back to back candidates	62
23	Momentum distribution of the merged fit	63
24	Distribution of cut parameters	65
25	Momentum distribution of merged tracks for final cut	65
26	dE/dx as function of particle momentum	67
27	Illustration of the count method for obtaining R_{raw}	68
28	Residuals of DC3 for Monte Carlo and real data	72
29	Number of points used by transversal fit for Monte Carlo and data	72
30	Number of points used by longitudinal fit for Monte Carlo and data	73
31	Background simulation after final back to back cut	76
32	Sum of the simulated background channels after final back to back cut	77
33	Monte Carlo sample for back to back event with background simulation	78
34	Fraction of p wave annihilation as function of pressure in H_2	82
35	Wu-Yang triangle	93

List of Tables

1	Characteristics of the CPLEAR magnet	19
2	CPLEAR detector characteristics 1	19
3	CPLEAR detector characteristics 2	20
4	Possible initial states for $p\bar{p}$ -annihilation into $\pi^+\pi^-$ and K^+K^-	53
5	Relative branching ratio for fit and count method	69
6	Central value and width for K^+K^- and $\pi^+\pi^-$ peak	69
7	Results of the count method for final cuts	69
8	Relative acceptance of K^+K^- and $\pi^+\pi^-$ events	74
9	Monte Carlo background simulation	75
10	Branching ratios for back to back background channels	76
11	Background to signal ratio for Monte Carlo and real data.	77
12	Fit parameters for K^+K^- and $\pi^+\pi^-$ peak in Monte Carlo and real data	78
13	Relative branching ratio $p\bar{p} \rightarrow K^+K^- / p\bar{p} \rightarrow \pi^+\pi^-$	79
14	Branching ratio from atomic s and p level for $\pi^+\pi^-$ and K^+K^-	80
15	Background to signal ratio for Monte Carlo and real data.	81
16	List of measured CP violating parameters	96

Curriculum Vitae

Date of birth: 31.12.1959

- 1967 - 1971: Primarschule Pestalozzi in Bern, Switzerland
- 1971 - 1975: Sekundarschule Munzinger in Bern
- 1975 - 1979: Gymnasium Kirchenfeld in Bern
- 1980 - 1986: Gained diploma in physics at the Eidgenössische
Technische Hochschule in Zurich, Switzerland.
- 1986 - 1990: Ph. D. - Experimental Particle Physics, employed by
ETH, but based at CERN.

Acknowledgments

I am very grateful to Professor Dr. H.-J. Gerber for giving me the opportunity to do this thesis and for advising and supporting me in the last four years.

My special thanks go to Dr. Chris "let's go skiing" Bee and to Dr. Peter "der juckt mich nimmer" Gumplinger. Chris helped me enormously over the last three years and he organizes the online work so smoothly, that one is tempted to forget, how important organisation is. Peter, on the other hand, provided the perfect and indispensable guidance through all the whiteouts between the offline lowlands and the lofty summits of the beautiful Swiss Alps.

I am also indebted to many people at CERN for fruitful discussions, in particular Dr. P. Bloch, Dr. M. Dodgeson, Dr. B. Eckart, Dr. M. Fidecaro, Dr. D. Francis, Dr. D. Garretta, Dr. C. Guyot, Dr. G. Hayes (with whom I share unforgettable Struck experiences), U. Johner, P. Kokkas, Dr. R. Le Gac, Dr. T. Ruf, Dr. L. Sacks, Dr. C. Santoni, Dr. F. Touchard, Dr. D. Tröster, Dr. E. Watson, Dr. P. Weber and H. Wendler.

I also owe many thanks to all the people at SIN/ETH for their support and advice, namely M. Dröge, Dr. W. Fetscher and Dr. T. Nakada, as well as to Professor Dr. L. Tauscher from the University of Basel.

Furthermore I am indebted to Oli Bernet for graphics support as well as to Cosa Rosa Bächli and Liz Furrer for their help while writing the thesis and for keeping bureaucracy away from me.

Finally I would like to thank my parents and all my friends in Bern and Zurich for their constant encouragement and companionship, in particular Alfred and Minouche, to whom I dedicate this thesis.